

Numerical investigation on the advance of leader channels in lightning and long sparks



Universidad de Granada

Alejandro Francisco Malagón Romero

Department of Solar System

Instituto de Astrofísica de Andalucía

Programa de Doctorado en Física y Ciencias del Espacio

A thesis submitted for the degree of

Philosophiæ Doctor (PhD)

March 2021

Examination date: March 23, 2021

Thesis supervisor:

Dr. D. Alejandro Luque Estepa

© Alejandro Francisco Malagón Romero

Cover design: Alejandro Francisco Malagón Romero

Cover picture: Lightning Storm. Ningyu Liu

A mis padres

Declaration

El doctorando / The doctoral candidate Alejandro Francisco Malagón Romero y el director de la tesis / and the thesis supervisor: Alejandro Luque Estepa.

Garantizamos, al firmar esta tesis doctoral, que el trabajo ha sido realizado por el doctorando bajo la dirección de los directores de la tesis y hasta donde nuestro conocimiento alcanza, en la realización del trabajo, se han respetado los derechos de otros autores a ser citados, cuando se han utilizado sus resultados o publicaciones.

Guarantee, by signing this doctoral thesis, that the work has been done by the doctoral candidate under the direction of the thesis supervisor/s and, as far as our knowledge reaches, in the performance of the work, the rights of other authors to be cited (when their results or publications have been used) have been respected.

Lugar y fecha / Place and date: Granada, 23 de Marzo de 2021

Director de la Tesis/
Thesis supervisor

Doctorando/
Doctoral candidate

Firma/Signed

Firma/Signed

Abstract

Lightning is one of the most spectacular phenomena on Earth. Despite its prevalence in our lives, it still holds many unknowns. In this thesis, we will be dealing with a fundamental problem in Lightning Physics, the stepped propagation of lightning channels as they head to the ground. The stepping mechanism is crucial to understand other processes such as the emission of X-rays or gamma radiation reported by numerous observations of lightning discharges in the last decades.

The stepping mechanism involves widely separated space and time scales: from nanoseconds to tens of microseconds and from a few micrometers up to tens of meters. Currently, observations are not able to resolve the tiniest scales associated with lightning. However, numerical models settle a framework to simulate basic phenomena in Lightning Physics and study its most elusive scales.

This thesis aims to study the stepped propagation of lightning channels with a prominently numerical approach. We have built a self-consistent state-of-the-art 2D cylindrically symmetric model that accounts for charge transport, electrostatic interactions, gas heating, and expansion. In our efforts for improving our model, we have implemented a numerical method to solve the Poisson equation that allows us to reduce the size of the computational domain, speeding up our simulations. This method is also valid to optimize the calculation of the photoionization term in streamer discharge codes.

We have used our model to investigate the emergence of space stems. These are luminous spots that appear ahead of an advancing leader mediating the leader's stepped propagation. We show that space stems start as regions of

locally depleted conductivity that form in the streamers of the corona around the leader. An attachment instability enhances the electric field leading to strongly inhomogeneous, bright, and locally warmer regions ahead of the leader that explain the existing observations.

Space stems are known to readily launch counter-propagating streamers. These are believed to heat the space stem close to leader temperatures. Similarly, high-altitude electric discharges such as sprites develop a non-thermal version of a space stem known as glow. As space stems, glows also shoot counter-propagating streamers. We have studied the mechanism underlying the onset of these counter-propagating streamers with the AFIVO 3D streamer model. Our results show that an attachment instability leads to a charge accumulation at the boundaries of the glow, which enables it to shoot these counter-propagating streamers. This explains the characteristic shape of carrot sprites. Finally, we have studied the effect of a forced electric current through a space-stem-like structure. The source of this electric current could be the counter-propagating streamers mentioned above. In the same way, we have studied the influence of water in the development of a space stem under such conditions. Our results show that water enhances the initially small plasma inhomogeneities. This explains some of the features observed in the leader stepping and highlights the relevance of water chemistry models to address leader propagation.

Resumen

Los rayos son uno de los fenómenos más espectaculares en la Tierra. A pesar de su prevalencia en nuestra vida, todavía guardan muchos secretos. En esta tesis, vamos a tratar un problema fundamental en Física de Rayos, la propagación a saltos del canal de un rayo a medida que se propaga hacia el suelo. El "mecanismo a saltos" es crucial para entender otros procesos como las emisiones de rayos X y radiación gamma observadas por numerosos experimentos en las últimas décadas.

El "mecanismo a saltos" involucra escalas espacio-temporales muy diversas: desde los nanosegundos hasta las decenas de microsegundos y desde los pocos micrómetros hasta las decenas de metros. Actualmente, las observaciones no son capaces de desentrañar las escalas más pequeñas asociadas a los rayos. Sin embargo, los modelos numéricos proporcionan un entorno para simular fenómenos básicos en la Física de Rayos y así estudiar las escalas de tiempo más elusivas.

Esta tesis tiene por objeto estudiar la propagación a saltos del canal de un rayo con un enfoque eminentemente numérico. Hemos desarrollado nuevo modelo numérico 2D con simetría cilíndrica capaz de describir el transporte de carga, las interacciones electrostáticas, el calentamiento y la expansión del gas que se dan en una descarga eléctrica. Al desarrollar un modelo numérico, es siempre importante su optimización para así agilizar las simulaciones. Para ello hemos implementado un método numérico que nos permite resolver la ecuación de Poisson en un dominio computacional ajustado a las dimensiones físicas de la descarga que simulamos. Este método también se puede utilizar para optimizar el cálculo del término de fotoionización que aparece en los códigos numéricos de descargas tipo dardo.

Hemos usado nuestro modelo para investigar el origen de los tallos espaciales. Estos son manchas luminosas que aparecen delante de un líder a medida que se propaga. Nuestros resultados muestran que los tallos espaciales se originan en zonas de conductividad reducida en los dardos que forman las coronas en torno al líder. Una inestabilidad de adhesión incrementa el campo eléctrico en estas zonas de conductividad reducida. Esto conduce a zonas inhomogéneas, brillantes y más calientes delante del líder que explican las observaciones existentes.

Los tallos espaciales son capaces de lanzar descargas tipo dardo. Estas descargas podrían ser responsables de calentar el tallo espacial hasta temperaturas cercanas a las del líder. De igual manera, descargas eléctricas a gran altitud como los "sprites" desarrollan una versión a temperatura ambiente del tallo espacial que se conoce como "brillo". Como los tallos espaciales, los brillos son capaces de lanzar dardos. Hemos estudiado el mecanismo que subyace al lanzamiento de estos dardos con AFIVO 3D, un modelo para descargas eléctricas de tipo dardo. Nuestros resultados apuntan a que, de nuevo, una inestabilidad de adhesión produce una acumulación de carga en los bordes del "brillo", lo que lleva al lanzamiento de descargas tipo dardo. Esto explica la característica forma de los "sprites" de tipo zanahoria.

Finalmente, hemos estudiado el efecto que tiene una corriente fluyendo a través de un plasma similar al tallo espacial. El origen de esta corriente podría ser las descargas tipo dardo que emanan del mismo. También hemos estudiado la influencia del agua en el desarrollo del tallo espacial bajo una corriente eléctrica forzada. Nuestros resultados muestran que el agua favorece el desarrollo de inhomogeneidades en el plasma que inicialmente eran pequeñas. Esto explica algunas de las características observadas en los saltos de los líderes y subraya la importancia de que los modelos químicos incluyan agua para abordar la propagación del líder.

Contents

List of Figures	xiii
List of Tables	xv
1 Introduction	1
1.1 Motivation: Lightning and long spark discharges	1
1.2 Fundamental processes in electric discharges	3
1.2.1 Transport processes	3
1.2.2 Kinetic processes	4
1.2.2.1 Ionization	5
1.2.2.2 Attachment	6
1.2.2.3 Excitations	7
1.2.2.4 Detachment	7
1.2.2.5 Recombination	8
1.2.3 Maxwell relaxation time and electric field enhancement	8
1.2.4 Avalanche to streamer transition	9
1.3 Streamer discharges	10
1.4 Leader discharges	13
1.5 Space stem onset: The attachment instability	15
1.6 Thesis Goals and contributions	18
1.7 Content	18

2	Electro-hydrodynamic model	21
2.1	Introduction	21
2.2	Electro-hydrodynamic model	22
2.3	Hyperbolic equations	24
2.3.1	Conservation laws	24
2.3.2	Weak solutions	25
2.3.3	The Rankine-Hugoniot Jump Conditions	25
2.3.4	Linear hyperbolic systems	27
2.3.5	Riemann problem	29
2.3.6	Non-linear hyperbolic system	32
2.3.7	Entropy condition and uniqueness	35
2.3.8	Riemann problem for a non-linear hyperbolic system	35
2.3.9	P-characteristic field: Linear degeneration and genuinely non-linear	36
2.4	Finite Volume Methods	36
2.4.1	The Courant-Friedrichs-Lewy (CFL) condition	38
2.4.2	First order Godunov's method for hyperbolic linear systems	39
2.4.3	Approximate Riemann solvers	40
2.4.4	Roe's solver	41
2.4.5	Wave propagation algorithms	42
2.4.6	High resolution methods	43
2.4.7	Multidimensional systems	44
2.4.8	Source terms	45
2.5	Poisson's equation	46
2.5.1	Discretization	46
2.5.2	Boundary conditions	47
2.5.3	Poisson's solvers	47
2.6	Numerical code	48

3	A domain-decomposition method to implement electrostatic free boundary conditions for electric discharges	49
3.1	Introduction	49
3.2	Electrostatic free boundary conditions in the radial direction	52
3.2.1	Domain decomposition	52
3.2.2	Linearity	55
3.2.3	Expansion in orthonormal solutions of the Laplace equation	55
3.2.4	Continuity of the normal derivative	56
3.2.5	Algorithm	57
3.2.6	Tests and sample implementation	58
3.2.6.1	Tests	58
3.2.6.2	Order of accuracy	59
3.2.7	Streamer simulations	61
3.3	Full free boundary conditions	63
3.3.1	Domain decomposition	63
3.3.2	Linearity	63
3.3.3	Expansion in solutions of the Laplace equation	65
3.3.4	Continuity of the normal derivative	65
3.3.5	Algorithm	67
3.3.6	Tests and sample implementation	67
3.3.6.1	Tests	67
3.3.6.2	Order of accuracy	69
3.3.7	Streamer simulations	69
3.4	Discussion and conclusions	72
4	Spontaneous emergence of space stems ahead of negative leaders in lightning and long sparks	75
4.1	Introduction	75
4.2	Space stem	77
4.2.1	Model and Initial Conditions	77
4.2.2	Results	80
4.2.2.1	Formation of the Space Stem	83

4.3	Two-Sphere Model for a Leader Corona	86
4.3.1	Model Description	87
4.3.2	Single Corona Discharge	90
4.3.3	Multiple Discharges	92
4.4	Discussion and Conclusions	92
5	On the emergence mechanism of carrot sprites	97
5.1	Introduction	97
5.2	Sprite streamer model	99
5.3	Observations	102
5.4	Results and Discussion	103
5.5	Conclusions	109
6	Stepping mechanism in humid air	111
6.1	Introduction	111
6.2	Model	112
6.3	Results and discussion	117
6.4	Conclusions	118
7	Summary and conclusions	121
7.1	Summary	121
7.2	Conclusions	123
8	Future Work	125
8.1	Future Work	125
	Appendix A Chemical models	127
A.1	Light Emissions	127
A.2	Chemical model	128
	References	139

List of Figures

1.1	Frame of a high-speed recording of a negative leader propagating towards the ground	2
1.2	Simulation of the propagation of a positive streamer at 13 km	11
1.3	Comparison of the electric field and the propagation velocity of streamers of opposite polarity	12
1.4	Comparison of the electron density in the wake of a positive and a negative streamer at STP	13
1.5	Sketch of the structure of a leader discharge	14
1.6	Frame of a high-speed recording of a negative stepped leader	15
1.7	Attachment instability	17
2.1	Discontinuity propagating with speed s , separating the pair of constant states (q_l, q_r)	27
2.2	Riemann problem	30
2.3	An example with characteristics	32
2.4	Colliding and diverging characteristic lines from the inviscid Burgers equation	33
2.5	Emerging discontinuities in non-linear hyperbolic equations	35
2.6	Discontinuity propagating with speed s , separating the pair of constant states (q_l, q_r)	38
2.7	Overshoots in the solution	44
3.1	Electric discharge geometry	53

LIST OF FIGURES

3.2	Comparison between Neumann boundary conditions and free boundary conditions	59
3.3	Streamer propagation with free radial boundary conditions	61
3.4	Domain decomposition of problem of a charge distribution in free space .	64
3.5	Comparison of the potential of a uniformly charged sphere in free space and between two electrodes	68
3.6	Electric field of a streamer as it approaches the electrode	70
3.7	Comparison of the streamer velocity for Dirichlet conditions and free boundary conditions	71
4.1	Space stem emergence, attachment instability light emission	81
4.2	Emergence of the space stem in a narrow section of the streamer channel .	84
4.3	Conductance per unit length and electric current in the streamer channel .	85
4.4	Isolated space stems cannot exist in positive leaders.	86
4.5	Sketch of the two-sphere model for a leader corona	88
4.6	Results of a single discharge in the two-sphere model	91
4.7	Results of multiple ionization waves in the two-sphere model	93
5.1	Sprite channel initial conditions	101
5.2	Time series from high-speed video observations of a sprite	102
5.3	3D simulation of a pre-ionized streamer channel	104
5.4	Non-linear behaviour of the rate coefficient for the production of $N_2(B^3\Pi_g)$. 105	
5.5	Electric current and luminosity of a pre-ionized streamer channel	108
6.1	Energy deposition into the different degrees of freedom of the background gas	114
6.2	Evolution of the electron density and electric field in the space stem in dry and humid air	117
6.3	Evolution of the temperature in the space stem in dry and humid air . . .	119

List of Tables

3.1	Error obtained with change in outer radius	60
3.2	Errors obtained with changes in the longitude of the domain	69
4.1	Parameter values employed in our simulations.	90
6.1	De-excitation rate coefficients of $N_2(v = 1)$ with the j th species.	116

Chapter 1

Introduction

1.1 Motivation: Lightning and long spark discharges

Lightning is one of the most spectacular phenomena on earth. Every second, around ten lightning flashes strike some point on Earth (*Christian et al.*, 2003), initiating wildfires, causing injuries (*Rakov and Uman*, 2003a) or damaging structures such as wind turbines (*Montanyà et al.*, 2016) causing millions of dollar losses every year. Nevertheless, we also benefit from smaller-scale discharges to treat surfaces (*Bárdos and Baránková*, 2010), clean the air (*Veldhuizen, van*, 2000) or treat wounds (*Nasir et al.*, 2016).

Despite its prevalence in our daily life, lightning still holds many unknowns: as they head towards the ground, most lightning channels propagate in a discontinuous manner or a series of "steps" (*Biagi et al.*, 2010). We do not know why. Related to this, during this stepped-wise propagation, the lightning channel emits X-ray bursts (*Moore et al.*, 2001; *Dwyer*, 2004). The precise mechanism whereby this happens is just partially understood. Satellites also report the emission of upward-directed gamma-ray radiation from thunderstorms, known as Terrestrial Gamma Flashes (TGFs) (*Fishman et al.*, 1994). There are two main mechanisms (*Dwyer et al.*, 2009; *Celestin et al.*, 2012) trying to address this problem, currently, we do not know which one is the right one.

It is well known that lightning is a very long spark discharge, similar to those long spark discharges in the laboratory with electrode gaps longer than around 2 m. Same physics at different space and time scales (*Aleksandrov and Bazelyan*, 1999). Therefore,

1. INTRODUCTION

significant knowledge of lightning discharges comes from the study of long spark discharges in the laboratory and vice versa. We will interchangeably speak about them to describe their features.

Depending on the starting and final point, lightning flashes are generally classified as cloud-to-cloud (CC) or cloud-to-ground (CG). CC lightning flashes constitute 75% of the total, including intracloud, intercloud, and cloud-to-air flashes. Only 25% of the lightning flashes hit the ground and out of that number, 90% are negative lightning flashes. A negative CG lightning flash (CG-) "effectively" transports negative charge from the cloud to the ground while a positive CG lightning flash (CG+) does the same for positive charge (*Rakov and Uman, 2003b*).

A CG- flash is composed of a luminous downward-traveling discharge, the leader, followed by a brighter upward-traveling discharge, the return stroke (*Schonland and Collens, 1934*). Figure 1.1 shows the leader (1) surrounded by a streamer corona (2) (*Raizer, 1991; Cooray, 2003*), a fan of faint, cold, and filamentary discharge channels that propagate due to a high electric field at their tips and pave the path for the advance of the leader. The leader advances as a section of the streamer corona heats and joins the leader.

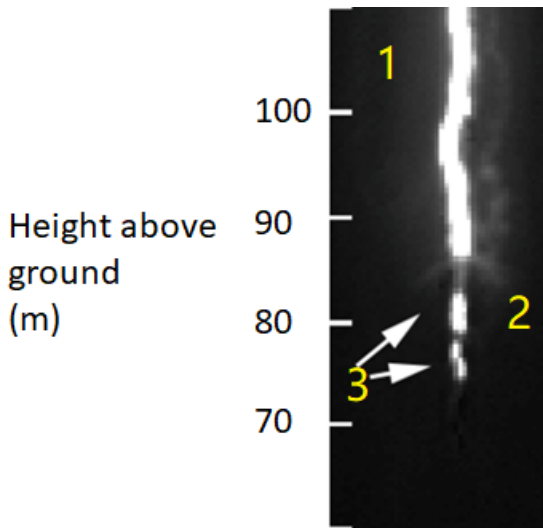


Figure 1.1: Frame of a high-speed recording of a negative leader propagating towards the ground. The main leader (1) advances as sections of the streamer corona (2) heat. Negative leaders advance in a series of steps punctuated by the so called space stem (3) that later becomes the new leader tip after a step is completed. (*Biagi et al., 2010*).

While positive leaders advance in a continuous manner (*Les Renardières group*, 1978b), negative leaders advance in a stepped fashion with step lengths ranging from a few meters to tens meters and with waiting times in the microsecond scale (*Schonland et al.*, 1935; *Gorin et al.*, 1976; *Les Renardières group*, 1978a). Experiments in laboratories (*Schonland et al.*, 1935; *Gorin et al.*, 1976; *Les Renardières group*, 1978a), as well as observations of artificial and natural lightning (*Biagi et al.*, 2014; *Hill et al.*, 2011; *Gamerota et al.*, 2014), show that the streamer-to-leader transition is mediated by the so-called space stem (3) (figure 1.1), a bright region that emerges in the streamer corona, separated from the leader tip a length comparable to the length of the leader steps. Then, the space stem evolves into a hot plasma, named space leader, that becomes the new leader tip once a step is completed.

The mechanism that leads to the formation of the space stems is so far unknown. However, its understanding is fundamental to fully address the polarity asymmetry as well as the leader propagation. This is the problem that we address in this thesis.

Next, we will shortly introduce some concepts and processes in electric discharges that are fundamental to understand leader discharge propagation.

1.2 Fundamental processes in electric discharges

1.2.1 Transport processes

An electric discharge occurs whenever a sufficiently high electric field is applied to an insulating medium such as air. Under that electric field \mathbf{E} , electrons will accelerate and gain energy that will be partly lost in collisions with neutrals. This gain-loss energy process gives rise to an average electron velocity, the drift velocity

$$\mathbf{v}_e = -\mu_e \mathbf{E}, \quad (1.1)$$

where μ_e is the electron mobility. The electron mobility is inversely proportional to the electron mass and the collision frequency, which in general depends on the electric field. Ions also drift under the electric field but, being heavier, its response is slower, and hence the associated mobility smaller.

1. INTRODUCTION

The transport of charges in the drift motion leads to an electric current \mathbf{j} that to a good approximation follows Ohm's law,

$$\mathbf{j} = \sigma \mathbf{E}. \quad (1.2)$$

Here, σ is the electric conductivity,

$$\sigma = \sum_s n_s q_s \mu_s, \quad (1.3)$$

where the sum extends over the species s , and n_s and q_s are the number density and electric charge of the species s respectively. It usually happens that the electron density, as well as the electron mobility, are several orders of magnitude larger than those of the ions, and thus, it is common to neglect the ionic current.

Although a minor process in streamer discharges, diffusion is often considered in numerical models: whenever there are density gradients, electron and ions diffuse towards lower density regions. The diffusion flux is defined as

$$\mathbf{\Gamma}_s = D_s \nabla n_s, \quad (1.4)$$

where s labels the species and D_s is the diffusion coefficient. As for mobility, diffusion coefficients for ions are usually orders of magnitude smaller than the electron diffusion coefficient. In many applications, it is common to neglect the diffusion of ions.

Electrons and ions collide with neutrals of the background gas, losing a fraction of the energy gained from the electric field. The energy density loss per unit time is the Joule heating:

$$Q = \mathbf{j} \cdot \mathbf{E} = \sigma E^2. \quad (1.5)$$

1.2.2 Kinetic processes

Next, we will describe the relevant processes that electrons immersed in an electronegative gas such as air undergo in the drift motion.

1.2.2.1 Ionization

Ionization is a mechanism of electron-ion pair production. In particular, ionization by electron impact is one of the main mechanisms of charge production in electric discharges at room temperature such as streamers. As one electron accelerates in an electric field, it gains energy. In a collision with an/a atom/molecule, the electron can release a further electron. For discharges in air at room temperature, the main species to ionize are N_2 and O_2 molecules with ionization potentials of 15.6 eV and 12.2 eV, respectively (*Bazelyan and Raizer, 1997*). The ionization rate is given by

$$\frac{dn_e}{dt} = (n_{O_2}k_{i,O_2} + n_{N_2}k_{i,N_2})n_e = \nu_i n_e, \quad (1.6)$$

where n_e , n_{O_2} and n_{N_2} are the electron, oxygen and nitrogen densities, k_{i,O_2} and k_{i,N_2} are the electron impact rate coefficient for O_2 and N_2 and ν_i is the "effective" ionization frequency. For a constant ionization frequency, the electron density experiences an avalanche growth from its initial value n_{e0}

$$n_e = n_{e0}e^{\nu_i t}. \quad (1.7)$$

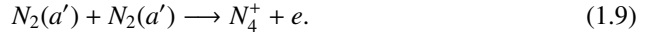
In the range of energies of this thesis, the higher the electron energy, the higher the probability to ionize further atoms and molecules. In a collision, an electron can excite electronically an atom so that the electrons in the outer layer are not so tightly coupled to the nuclei. Then, a subsequent electron-impact collision can release one of these electrons. This process requires less energy, in fact below the ionization potential. As we will see, electronic excitation has a lower potential threshold and therefore there are more excitation than ionization events. This is fundamental for the production of ionizing photons.

Photoionization is another relevant charge production mechanism (*Zhelezniak et al., 1982*). In this process, an excited nitrogen molecule releases a photon with enough energy to ionize an oxygen molecule. As we will see in the next sections, photoionization is fundamental for the growth of positive streamers (*Nijdam et al., 2010; Pancheshnyi, 2005*).

As neutrals and excited states populate the background gas and the temperature increases (roughly above 1000 K) new ionization processes such as associative ionization

1. INTRODUCTION

become relevant to sustain the charge production. Two of the most important reactions of this kind involve excited or neutral:



Both reactions require relatively high abundance of neutrals and excited molecules to be relevant.

1.2.2.2 Attachment

Some neutrals have affinity to form a negative ion. The energy associated with the ground state of these ions is slightly lower than the energy of the ground state of the corresponding neutral. Thus, there is a tendency of these neutrals to "capture" free electrons. As we mentioned, the final ion state has a lower energy. Depending on the way this extra energy is released, we have 3-body attachment or dissociative attachment. Examples of these two in air (M) are



Reaction 1.10, called three-body attachment, is the most relevant attachment reaction for low electric fields in air at room temperature. On the other hand, reaction 1.11, called dissociative attachment, is prominent for moderate electric fields. This agrees with intuition since breaking an O_2 molecule requires more energy than simply attaching to the molecule. The electron loss by attachment is given by

$$\frac{dn_e}{dt} = -(k_{3B} + k_{DA}) n_{O_2} n_e = -\nu_a n_e, \quad (1.12)$$

where k_{3B} and k_{AD} are the three-body and dissociative attachment rate coefficients respectively and ν_a is the attachment frequency.

1.2.2.3 Excitations

In air, electrons can readily excite a neutral electronically, vibrationally, or rotationally (*Capitelli et al.*, 2000). That is, part of the kinetic energy of the electron is transferred to one of these internal degrees of freedom. The energy threshold for N_2 electronically excited states varies from 6 eV to 11 eV (*Bazelyan and Raizer*, 1997). For N_2 vibrationally excited states, threshold energies ranges from 1.8 eV to 3.3 eV (*Bazelyan and Raizer*, 1997). With lower energy thresholds, excited states are more abundant than ionized states. This is fundamental since excited states are prone to populate the gas with ionizing photons able to trigger electron avalanches.

1.2.2.4 Detachment

Negative ions can also experience collisions with neutrals that lead to the release of an electron. In air at room temperature these are the main mechanisms of electron detachment:



As it can be inferred, the second detachment reaction requires more energy since it breaks the O_2 molecule. Under moderated electric fields (60 Td to 90 Td), air is efficiently populated with O and O^- through reactions 1.14 and 1.11. When O^- and O are sufficiently abundant,



becomes the dominant detachment reaction (*da Silva and Pasko*, 2013).

1.2.2.5 Recombination

Electron-ion recombination processes are usually slower than other electron-loss processes. Even for a neutral plasma where $n_+ \approx n_e$, the recombination rate

$$\beta_{recombination} n_e^2 \ll k_a n_{air} n_e. \quad (1.16)$$

Electrons are quickly transformed into negative ions through attachment. Therefore, ion-ion recombination can be another possible sink of charge carriers. However, this is usually a minor process since a significant abundance of ions requires long time scales (*Bazelyan and Raizer, 1997*).

1.2.3 Maxwell relaxation time and electric field enhancement

When an electric field is applied to a neutral plasma seed, charges of opposite sign drift in opposite directions. In the interior of the seed, this charge separation leads to an electric field that screens the background field. The evolution of the charge density is given by the equation for the conservation of charge

$$\frac{\partial \rho_c}{\partial t} + \nabla \cdot \mathbf{j} = 0. \quad (1.17)$$

The charge separation sources the resulting electric field in the plasma seed. This is reflected in Poisson equation

$$\nabla \cdot \mathbf{E} = \frac{\rho_c}{\epsilon_0}, \quad (1.18)$$

where ϵ_0 is the vacuum permittivity. From Ohm's Law equation 1.2, charge conservation equation 1.17 and Poisson equation 1.18 we can get the local rate of change for the electric field

$$\frac{\partial_t |\mathbf{E}|}{|\mathbf{E}|} = \frac{-\sigma}{\epsilon_0}, \quad (1.19)$$

where $\partial_t \equiv \frac{\partial}{\partial t}$. Equation 1.19 suggests a physical time scale, usually named as Maxwell (or dielectric) relaxation time

$$\tau_{Maxwell} = \frac{\epsilon_0}{\sigma}. \quad (1.20)$$

This physical time scale is a constraint on the time step length in numerical simulations. It gives an idea of how often we should solve Poisson equation to update the value of the electric field.

The conservation of charge signified in equation 1.17 has an important consequence for the growth of spatial electric charges. The charge separation will lead to an electric field enhancement at the boundaries of the neutral plasma seed in time scales on the order of the Maxwell relaxation time, reaching electric field values capable of ionizing the background gas. This is a fundamental process for the building block of electric discharges, the streamer discharge.

1.2.4 Avalanche to streamer transition

The development of an electric discharge is a competition between gain-loss electron processes. We have already seen that when there is exclusively ionization, the electron density experiences an avalanche-like growth in time. This also happens in space under the same assumptions

$$\frac{dn_e}{dx} = n_e \alpha, \quad (1.21)$$

where α is the ionization coefficient that represents the number of ionization events per unit length. Taking into account the attachment processes, we can also define an attachment coefficient β in pretty much the same way so the avalanche growth in one dimension is given by

$$\frac{dn_e}{dx} = \tilde{\alpha} n_e, \quad (1.22)$$

where $\tilde{\alpha} = (\alpha - \beta)$ is the effective ionization coefficient. The avalanche will grow as long as $\tilde{\alpha} > 0$ and the value of the electric field for which $\tilde{\alpha} = 0$ is the breakdown electric field whose value in air is approximately 30 kV/cm.

As the avalanche-growth continues, there is a moment when the space charge effects become important and the electric field generated by the avalanche is comparable to the background electric field. That is the avalanche-to-streamer transition. The Raether-Meek

criterion suggests that the space charge effects become important when $\tilde{\alpha}L \approx 20$, where L is the distance traveled by the avalanche (*Bazelyan and Raizer, 1997*).

1.3 Streamer discharges

A streamer is a cold and filamentary electric discharge that propagates due to a high electric field at its tip (*Cooray, 2003; Nijdam et al., 2020*). This enhanced field is caused by a surplus of charge concentrated in a thin layer of a few micrometers in thickness. As the streamer tip propagates, it leaves behind a quasi-neutral plasma, known as streamer body or streamer channel (fig. 1.2). Note that the reduced electric field E_{red} (Fig. 1.2) is defined as the ratio E/n_{air} , where E is the electric field and n_{air} is the air number density. E_{red} is measured in Townsend, which is defined by the relation $1 \text{ Td} = 10^{21} \text{ Vm}^{-2}$.

The application of a background electric field in air, sets a privileged direction for the propagation of a streamer discharge. Streamers that propagate in the direction of the electric field are called positive streamers while those that propagate in the opposite direction are called negative streamers. This asymmetry leads to substantial differences among positive and negative streamers that we detail below.

The growth of a streamer channel depends on the effective ionization of air. Since positive streamers propagate against the electron drift motion, the ionization in front of it mainly depends on electron avalanches that move towards the streamer head. Hence, for its propagation in virgin air, a positive streamer requires an upstream electron source such as photoionization (*Nijdam et al., 2010; Pancheshnyi, 2005*). On the other hand, a negative streamer propagates in the direction of the electron drift motion. Close to the streamer tip, electrons move outwards, ionizing the air in front of them. Consequently, photoionization is not such a relevant process for negative streamers.

In negative streamers, the charge layer at the tip contains an excess of negative charge. Around this region, electrons drift outwards, broadening the volume of the charge layer, decreasing the focus and enhancement of the electric field. On the contrary, in a positive streamer, the charge layer is characterized by a positive charge surplus. Ions are slower than electrons and although they drift outwards following the electric field lines, the broadening of the charge layer is negligible.

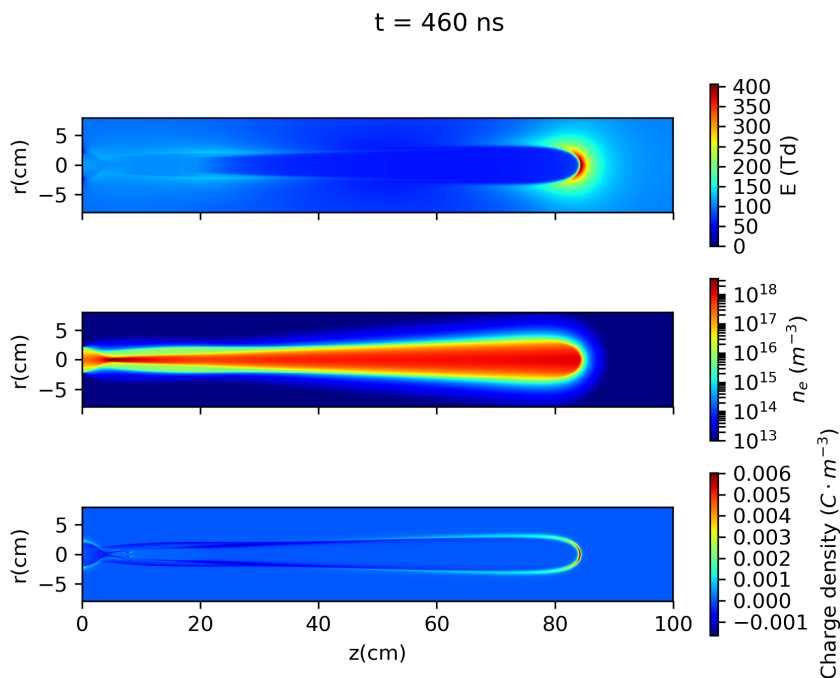


Figure 1.2: Snapshot of the evolution of the reduced electric field (upper panel), electron density (middle panel) and charge density of a positive streamer at 13 km. The enhanced electric field at the tip (upper plot) is caused by a surplus of positive charge in a thin layer (lower panel). As it propagates, the streamer tip leaves behind an ionized (middle panel) quasi-neutral wake.

Experiments (*Briels et al.*, 2008) and simulations (see fig. 1.3) show that positive streamers are better at focusing and enhancing the electric field at their tip, hence, the voltage required to initiate them is lower than for negative streamers (*Briels et al.*, 2008). Although positive streamers are more readily produced in a laboratory than negative streamers, from a computational point of view, positive streamers usually require a higher spatial resolution to properly resolve the space charge layer at the tip.

In general, due to a higher electric field at the tip, positive streamers propagate faster than negative streamers (see fig. 1.3). As we argued before, the electron drift motion broadens the head in negative streamers, decreasing the enhanced electric field. A lower electric field in the streamer head results in lower ionization rates and therefore a slower-

1. INTRODUCTION

growing discharge. (Luque *et al.*, 2008).

For the same reason, the electron density in a positive streamer wake is (fig. 1.4). As a consequence, the electric field is better screened along the channel, favoring a greater enhancement of the field at the tip. This is a consequence of the strong coupling streamer channel-head.

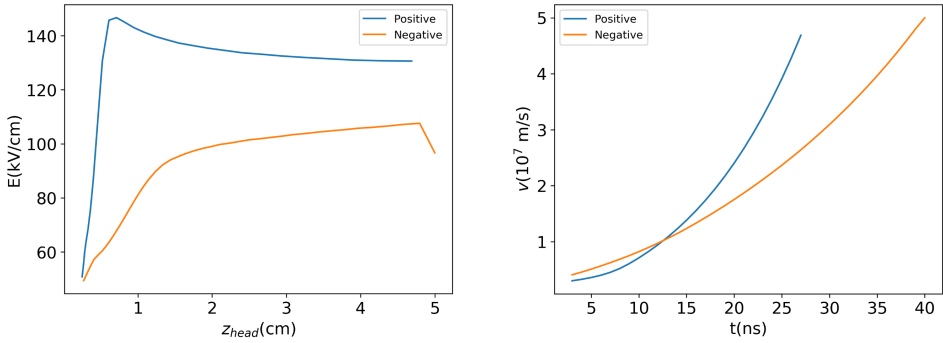


Figure 1.3: Comparative plots of the electric field at the tip and the streamer velocity for different polarities. Positive streamers carry a higher electric field at the tip (left panel) and propagate faster than negative streamers (right panel).

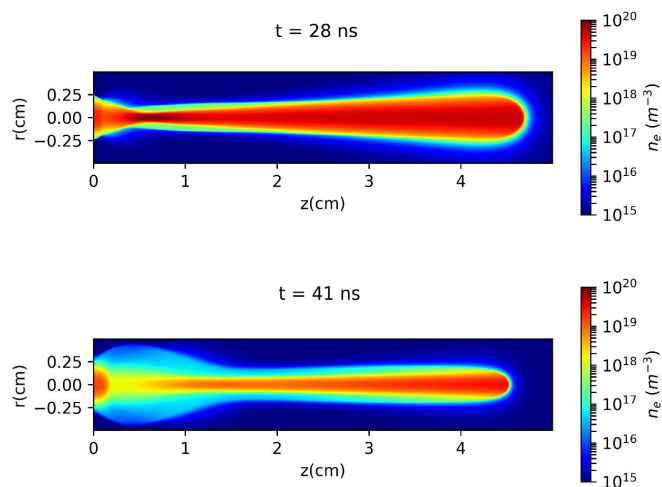


Figure 1.4: Snapshot of the evolution of the electron density for a positive streamer (upper panel) and a negative streamer (lower panel). A positive streamer carries a higher electric field at its tip. Therefore, the ionization in a positive streamer wake is higher than in a negative streamer

1.4 Leader discharges

A leader discharge is a fundamental process in the development of long spark discharges (> 1 m) (Gallimberti *et al.*, 2002). Figure 1.5 shows four major regions that characterize the complex structure of a leader (Bazelyan and Raizer, 1997): The leader channel (1), the leader tip (2), the streamer corona (3) and the leader sheath (4).

The leader channel is the long-lived region. It is a bright, highly conductive and hot core characterized by temperatures of around 5000 K and even 30 000 K in laboratory leader discharges and around 30 000 K in lightning (Cooray, 2003; Orville, 1968; Kieu *et al.*, 2020). The leader tip is colder, about 1000 K (Aleksandrov and Bazelyan, 1999). At the leader channel, the field is highly screened and so the conductivity is maintained by thermal processes such as associative ionization (reaction 1.8). This effective screening, transfers a significant portion of the electrode (cloud) potential to the leader tip that enables the onset of streamer discharges that form the corona.

The growth of a leader is accompanied by a succession of streamer corona bursts that

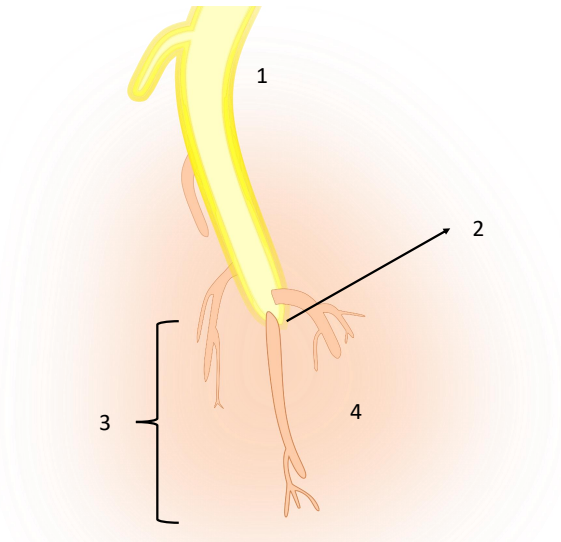


Figure 1.5: Sketch of the structure of a leader discharge: The long-lived region or leader channel (1), the leader tip (2), the streamer corona (3) and the leader sheath (4).

ionize sections of the air in front. As the leader advances, the leader channel sees itself surrounded by an ionized "envelope" ((4) in figure 1.5) that reduces its lateral expansion and stabilizes its propagation (*Raizer, 1991*).

Observations report a polarity asymmetry in the leader propagation: while positive leaders propagate in a continuous manner, negative leaders propagate in a series of steps or jumps and therefore, they are usually called stepped leaders.

In positive leaders, the streamer-to-leader conversion zone is adjacent to the leader tip, where all streamers emerge. This zone is heated by the current that the streamer corona carries. On the other hand, in negative leaders the conversion zone is optically separated from the leader tip (*Biagi et al., 2014*). Observations (see fig. 1.6) show that the streamer-to-leader transition is mediated by the so-called space stem, a bright and isolated region in the streamer corona. The leader completes a step when the space stem joins the main leader, becoming the new leader tip.

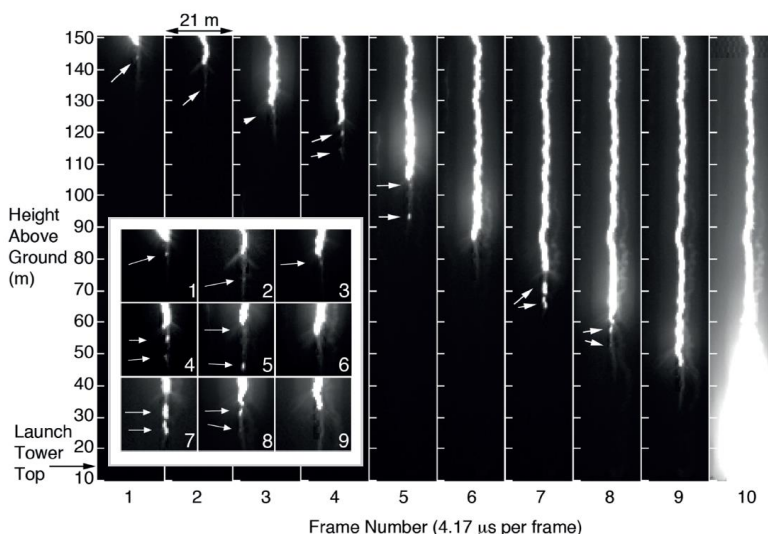


Figure 1.6: Frames of a high-speed recording of negative stepped leader adapted from ((Biagi *et al.*, 2010)). The sequence shows the stepped propagation of a descending negative lightning leader and the formation of spaces stems (arrows) ahead. A faint streamer corona is also visible in some frames.

1.5 Space stem onset: The attachment instability

One of the most pressing questions in the propagation of a negative leader is the onset of the space stem and the mechanism that heats it to become a space leader. In this thesis, we propose that the formation of the space stem is mediated by the action of an attachment instability (Douglas-Hamilton and Mani, 1974; Sigmond, 1984) in a streamer channel.

The key is the non-monotonic dependence of the net attachment rate on the electric field. The dissociative attachment reaction 1.11 has an energy threshold corresponding to the dissociation energy of the intermediate unstable negative ion O_2^* . Hence, the dissociative attachment rate increases with increasing electric field.

The net ionization rate is depicted in the left panel of figure 1.7. For this calculation we have considered 3-body attachment, dissociative attachment and electron impact ionization. Above the breakdown electric field E_k , the electron production dominates over electron loss. Nevertheless, below E_s , a higher electric field implies faster electron depletion.

1. INTRODUCTION

In the streamer channel, the evolution of the electric field is driven by the balance between chemical and transport processes. We can derive a toy model (Luque *et al.*, 2016a) to study the effect of the attachment instability by considering these two contributions.

Following Luque *et al.* (2016a), we assume that the homogenization of the electric current in the channel occurs in short time scales and so for our analysis we can consider that $\nabla \cdot \mathbf{j}_e = 0$. Then, if we take an infinitesimally thin slice in a streamer channel, the electron density evolves according to the equation:

$$\frac{dn_e}{dt} = k_{eff} n_{air} n_e, \quad (1.23)$$

with k_{eff} being the effective ionization rate.

If we assume that variations in the radial direction are negligible, the current through that streamer channel slice can be written as

$$I = \eta E, \quad (1.24)$$

where $\eta = 2\pi e\mu \int_0^R dr n_e$ is the conductance. Combining equations 1.23 and 1.24 we can derive an equation for the evolution of the electric field:

$$\frac{dE}{dt} = E \left(\frac{1}{I} \frac{dI}{dt} - \frac{1}{\eta} \frac{d\eta}{dt} \right), \quad (1.25)$$

or in terms of the net ionization rate (Luque *et al.*, 2016a),

$$\frac{dE}{dt} = E \left(\frac{1}{I} \frac{dI}{dt} - k_{eff} n_{air} \right). \quad (1.26)$$

Now, we assume a decaying current $\frac{1}{I} \frac{dI}{dt} = -\tau$, with decay constant τ determined by the global dynamics of the streamer. The green point in fig. 1.7 is unstable. Thus, the system will move away from that point, either climbing or descending the curve of the net ionization rate. This will result in regions with significantly different conductivities.

In a streamer channel, the electron density left behind by the streamer head is not necessarily homogeneous, therefore creating regions with different conductivity. Consider three distinct regions A,B characterized by an electric field E and S with associated electric field E_s , as depicted in fig. 1.7. Assume that S is a region with lower conductivity. The charge separation leads to both, an enhanced electric field $E_s > E$ and a greater dissociative

attachment rate in S. As a result, electrons are depleted faster, decreasing the conductivity, increasing the charge separation and subsequently the electric field. This feedback process will continue until the electric field saturates in S (E_s).

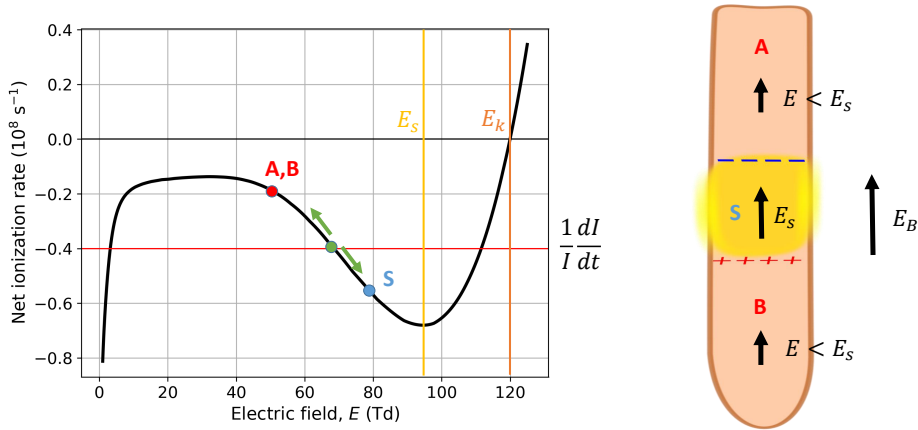


Figure 1.7: The attachment instability in region S, leads to a sharply defined region with lower conductivity and an enhanced electric field E_s .

Presumably, region S is the space stem. The action of the attachment instability leads to inhomogeneities inside the streamer channel and an accumulation of charges at the boundaries of the space stem. This accumulation of charges is prone to launch counter-propagating streamers that heat the space stem. These streamers are actually observed in experiments by (Kochkin *et al.*, 2012) and probably force a strong current through the space stem that heats it to a few thousand degrees. We will revisit and dig into all these topics in chapters 4, 5 and 6.

As the space stem reaches temperatures of around 1000 K, the electron loss due to attachment processes (mainly dissociative attachment) is balanced by the detachment from O^- ions (reaction 1.15). Once that thermal ionization processes becomes the main source of electrons, the conductivity at the space stem (S) surpasses that of the outer regions (A and B). Consequently, the inner electric field is expelled i.e. $E > E_s$ and the charge distribution at the space stem boundaries is inverted. The higher electric field in A heats

the segment connecting the leader and the space stem, completing a leader step.

1.6 Thesis Goals and contributions

As we have discussed throughout this chapter, the precise mechanism whereby lightning and long spark discharges propagate is only partially understood. The formation of space stems is enigmatic and the mechanisms that promote it to a space leader are not yet well established. Undoubtedly, experiments provide valuable information about the physics involved, however current technology is not able to resolve the smallest scales involved in the stepping mechanism. On the other hand, numerical simulations can provide insight about these scales. In this thesis we aim to test the hypothesis that the space stem arises due to an attachment instability. We will also investigate the mechanism that enables space stems to shoot counter-propagating streamers. These counter-propagating streamers are believed to sustain the current through the space stem, heating it up to become a space leader that finally joins the leader. We will address these problems using a numerical approach. For that, as a first step, we need to build an electro-hydrodynamic model that couples charge transport, electrostatic interactions, gas heating and expansion together with a suite of the appropriate chemical reactions for the time-scales under consideration.

1.7 Content

We have divided the content of this thesis in the following way: In chapter 2 we present an electro-hydrodynamic model for the streamer-to-leader transition and the numerical methods employed to solve it. Chapter 3 is devoted to a numerical method to optimize the resolution of Poisson's equation in unbounded domains, work published in *Malagón-Romero and Luque (2018)*. In chapter 4 we use our electro-hydrodynamical code to study the emergence of space stem precursors. The results are published in *Malagón-Romero and Luque (2019)*. In chapter 5 we study the evolution space-stem-like structures at high altitude and how the charge distribution enables them to shoot counter-propagating streamers (*Malagón-Romero et al., 2020*). In chapter 6 we study the heating effects of a sustained electric current flowing through the space stem in dry and humid air conditions. Finally,

chapters 7 and 8 are devoted to the summary, conclusions and future work plans respectively.

It is worth mentioning the work done with streamer simulations to study the contribution of sprite streamers to the chemical composition of the mesosphere-lower thermosphere and improve spectroscopic diagnostic methods of atmospheric electricity phenomena. These works were published in *Malagón-Romero et al. (2019)* and *Pérez-Invernón et al. (2020)* respectively. We have not included them in this thesis for the sake of consistency with the main topic.

1. INTRODUCTION

Chapter 2

Electro-hydrodynamic model

2.1 Introduction

A sufficiently long electric discharge propagates in essentially two phases before it bridges the electrode gap: the streamer phase consists of thin filaments of ionized air that propagate due to a high electric field at their tip. The dominant process here is impact ionization. In the leader phase, the electric current in the streamers has increased the air temperature to a few thousand K and the thermal energy of the molecules is comparable to the ionization potential of N_2 and O_2 .

The study of the streamer-to-leader transition calls for a model of electric discharges that includes heating and gas expansion fully self-consistently. In our approach, we will not study temperatures higher than 2000 K and so we will not consider thermal conduction or viscous dissipation processes since the time scales associated with the streamer-to-leader transition are too short for them to be relevant. In chapter 4, we will study the evolution of a streamer emerging from the leader tip up to 100 ns. In this case, we model the dynamics of air with the compressible Euler equations, by considering the vibrational energy evolution decoupled from the translational energy evolution since the vibrational-translational relaxation is way beyond the time-scale we pursue. In chapter 6, we will face longer time-scales, and so we will extend our set of equations to include the evolution of vibrational energy and vibrational-translational relaxation.

In order to study the influence of the electric current flowing in the electric discharge,

we have to couple the gas dynamics equations with the transport equations for the charged species as well as the equation describing the electrostatic interactions among them, that is, Poisson's equation.

Euler equations and charge transport equations fit into the so-called hyperbolic equations while the Poisson equation is an elliptic equation. In general, we cannot solve these equations analytically and so we need to use numerical methods. This chapter is organized as follows: In section 2.2 we describe the electro-hydrodynamic model to study the streamer-to-leader transition. Section 2.3 is an introduction to the mathematical background of hyperbolic equations and section 2.4 is devoted to finite volume methods, a set of numerical techniques to solve this kind of equations. Then, we describe the procedure followed to solve the Poisson equation in section 2.5 and finally, in section 2.6 we give a short description of our numerical code.

2.2 Electro-hydrodynamic model

As we have seen in chapter 1, the environment around a leader channel is quite complex, with the sheath and the streamer corona populated by hundreds of interacting streamers. Despite recent progress in three-dimensional streamer simulations (*Luque and Ebert, 2014; Teunissen and Ebert, 2017; Shi et al., 2017*), a full corona around a leader is presently out of reach for numerical models.

In this thesis we opt for simulating discharge channels where there exist, in good approximation, a cylindrical symmetry. Therefore, we build a 2D cylindrically symmetric model (z, r) for electric discharges that includes heating and expansion of the background gas fully self-consistently. The background gas, that is, the air where the discharge will develop, follows the equation of state for an ideal gas and its dynamics is described by the compressible Euler equations (*Popov, 2003; da Silva and Pasko, 2013; and Lifshitz, 1987*). These are conservation equations for mass, momentum and energy:

$$\frac{\partial \rho}{\partial t} + \mathbf{u} \cdot \nabla \rho + \rho \nabla \cdot \mathbf{u} = 0, \quad (2.1a)$$

$$\frac{\partial \mathbf{u}}{\partial t} + (\mathbf{u} \cdot \nabla) \mathbf{u} + \frac{\nabla p}{\rho} = 0, \quad (2.1b)$$

$$\frac{\partial \varepsilon}{\partial t} + \mathbf{u} \cdot \nabla \varepsilon + \frac{p}{\rho} \nabla \cdot \mathbf{u} = \frac{Q_T^{eff}}{\rho}. \quad (2.1c)$$

Here ρ is the mass density of air, \mathbf{u} is the local velocity at a given point and time, p is the pressure and ε is the specific energy associated with the rotational and translational degrees of freedom, which we assume in thermal equilibrium. Q_T^{eff} is the local power density dissipated by the electric discharge that goes into gas heating. By using equations 2.1 and the equation of state for an ideal gas, we neglect thermal conduction and viscous dissipation. We will use this approach in chapter 4, to study time scales not longer than 100 ns. In chapter 6, we will consider longer time scales where vibrational-translational non-equilibrium starts to become relevant. To do that we will extend the system of equations 2.1 to account for the evolution of the vibrational energy density.

All species are advected along with the fluid with a velocity \mathbf{u} . Furthermore, charged species drift on top of the background gas motion according to the local value of the electric field \mathbf{E} , so the resulting velocity is $\mathbf{v}_s = \mathbf{u} + \mu_s \mathbf{E}$, where s labels the species and μ_s is the corresponding mobility. In our model, the dynamics of all charged species is described by diffusion-drift-reaction equations for electrons and ions,

$$\frac{\partial n_s}{\partial t} + \nabla \cdot (n_s \mathbf{v}_s) = C_s + \nabla \cdot (D_s \nabla n_s) + S_{ph} \delta_{O_2^+,i} + S_{ph} \delta_{e,i}, \quad (2.2)$$

where n_s is the number density, D_s is the diffusion coefficient, C_s is the net production of species s and S_{ph} is the photoionization term. The Kronecker deltas $\delta_{e,i}$ and $\delta_{O_2^+,i}$ express the fact that the photoionization term only applies to the equations for electrons and O_2^+ .

The kinetic scheme employed in our simulations depends on the time scales that we plan to study. In chapter 4, the chemical scheme includes impact ionization, attachment/detachment, and water cluster formation/breaking (Luque *et al.*, 2017). In chapter 6, we will extend the chemical model mentioned above with a set of chemical reactions accounting for processes relevant at temperatures of several thousand degrees (da Silva and Pasko, 2013; Liu and Becerra, 2017).

2. ELECTRO-HYDRODYNAMIC MODEL

Moving to the electrostatic part of our model, the electric field $\mathbf{E} = -\nabla\phi$ is determined by the balance of charged species and satisfies the Poisson equation

$$\nabla^2\phi = -\sum_s \frac{q_s n_s}{\epsilon_0}, \quad (2.3)$$

where q_s is the charge of species s and ϵ_0 is the vacuum permittivity, which we assume is also valid for air.

2.3 Hyperbolic equations

2.3.1 Conservation laws

Consider a spatial domain $\Omega \subseteq \mathbb{R}^n$. Euler equations 2.1 and transport equations for electrons and ions 2.2 can be written in a general form as:

$$\frac{\partial q(\mathbf{x}, t)}{\partial t} + \sum_{j=1}^n \frac{\partial f_j(q(\mathbf{x}, t))}{\partial x_j} = \Psi(q(\mathbf{x}, t)), \quad \mathbf{x} \in \mathbb{R}^n \quad (2.4)$$

where $q \in \mathbb{R}^m$ is the vector of conserved quantities, $f_j \in \mathbb{R}^m$ is the j -component of the vector of fluxes through the boundary $\partial\Omega$ and $\Psi \in \mathbb{R}^m$ is the vector of source terms. Equation 2.4 is known as balance equation law and it states that the rate of change in q is a balance between flux and source terms. In many cases, the rate of change in q is only due to the flux, that is $\Psi \equiv 0$, and then each equation in 2.4 is termed as conservation equation law. The partial differential equations 2.4 are derived from a more fundamental integral form

$$\frac{d}{dt} \int_{\Omega} q(\mathbf{x}, t) dV + \sum_{j=1}^n \int_{\Omega} f_j n_j dS = \int_{\Omega} \Psi(q(\mathbf{x}, t)) dV. \quad (2.5)$$

The differential form is not valid at discontinuities such as shocks or contact surfaces that turn out to be physical solutions. We will often write the differential form for convenience, to build a matrix representation of the partial differential equation (PDE), but always bearing in mind the most fundamental integral form. In most of the derivations throughout this chapter, we will only consider conservation laws. Later on, we will discuss how to handle source terms in balanced equation laws.

2.3.2 Weak solutions

The integral form 2.5 is valid anywhere. There are no requirements on the smoothness of q . Equations 2.4 and 2.5 are equivalent provided that the solution is continuously differentiable. The integral form admits discontinuous solutions for which the PDE is not even defined in a classical sense. The differential form is valid where q is smooth but it is not valid at the discontinuities. We wish to extend the space of solutions of 2.4 to include discontinuous solutions. We are going to work out this for a 1-dimensional space but this is easily extended to an n-dimensional space. Let $\phi(x, t)$ be a test function, continuously differentiable with compact support, i.e. $\phi \in C_0^1(\mathbb{R} \times \mathbb{R})$. If we multiply equation 2.4 by the test function and integrate over space and time, we have

$$\int_0^\infty \int_\Omega (\phi q_t + \phi f(q)_x) dV dt = 0. \quad (2.6)$$

Since our flux may diverge, we should exchange derivatives as follows:

$$\int_0^\infty \int_{-\infty}^\infty (\phi q)_t + (\phi f(q))_x dx dt - \int_0^\infty \int_{-\infty}^\infty \phi_t q + \phi_x f(q) dx dt = 0. \quad (2.7)$$

Then, we obtain

$$\int_0^\infty \int_{-\infty}^\infty \phi_t q + \phi_x f(q) dx dt = - \int_{-\infty}^\infty \phi(x, 0) q(x, 0) dx. \quad (2.8)$$

All the boundary terms that usually appear after integration vanish at infinity due to the compact support test function ϕ . Note that the right-hand term brings in the initial conditions. We say that q is a weak solution of the PDE 2.4 if it satisfies 2.8 for every $\phi \in C_0^1(\mathbb{R} \times \mathbb{R})$.

2.3.3 The Rankine-Hugoniot Jump Conditions

We can characterize weak solutions by regions of smooth behavior separated by discontinuities. Therefore, these weak solutions satisfy the differential form where they are smooth and an additional condition at the discontinuities named Rankine-Hugoniot condition. Next, we are going to derive this condition from the integral form in one dimension but this is extensible to higher dimensions. Consider a region in the plane x-t

2. ELECTRO-HYDRODYNAMIC MODEL

$[x_1, x_1 + \Delta x] \times [t_1, t_1 + \Delta t]$, where Δx and Δt are small enough to consider that the shock wave speed s is constant and that q_l and q_r are constant in the wedges defined by $x = st$ (figure 2.1). If we apply 2.5 to our region of interest we get

$$\frac{d}{dt} \int_{x_1}^{x_1 + \Delta x} q(x, t) dx = f(q(x_1, t)) - f(q(x_1 + \Delta x, t)). \quad (2.9)$$

If we integrate in time we obtain

$$\begin{aligned} & \int_{x_1}^{x_1 + \Delta x} q(x, t_1 + \Delta t) dx - \int_{x_1}^{x_1 + \Delta x} q(x, t_1) dx \\ &= \int_{t_1}^{t_1 + \Delta t} f(q(x_1, t)) dt - \int_{t_1}^{t_1 + \Delta t} f(q(x_1 + \Delta x, t)) dt. \end{aligned} \quad (2.10)$$

The first and second terms on the left side are just the constant states q_l and q_r respectively. Hence, we can write the previous equation as

$$(q_r - q_l) s = f(q_l) - f(q_r), \quad (2.11)$$

where $s = \frac{\Delta x}{\Delta t}$ is the propagation speed of the discontinuity. Equation 2.11 is the Rankine-Hugoniot condition and restricts the jump in q to be a linear combination of the jump in the fluxes. This derivation is fundamental and any discontinuous solution of the equation 2.5 must verify it.

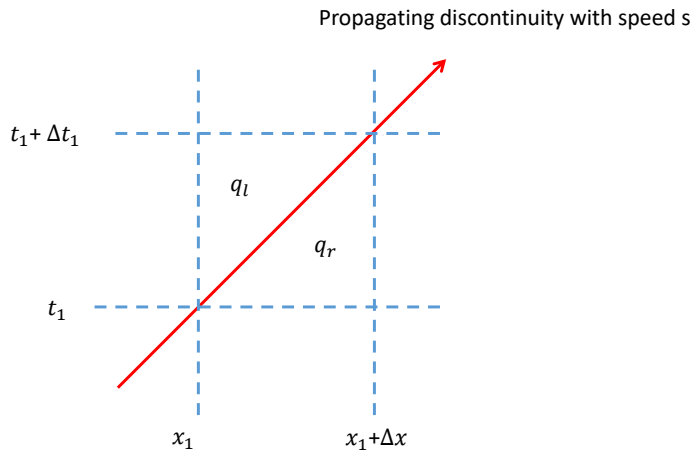


Figure 2.1: Discontinuity propagating with speed s , separating the pair of constant states (q_l, q_r) .

2.3.4 Linear hyperbolic systems

Gas dynamics and charge transport equations constitute a non-linear hyperbolic system. We will start with the mathematical framework for linear hyperbolic systems, fundamental to understand the non-linear hyperbolic systems theory. For simplicity, we will adopt again a one-dimensional approach. Consider a system of equations together with initial conditions

$$q_t + Aq_x = 0, \tag{2.12}$$

$$q(x, t = 0) = q_0(x), \tag{2.13}$$

where $q \in \mathbb{R}^m$ and $A \in \mathbb{R}^{m \times m}$. Here, $f(q) = Aq$. The linear system is said to be hyperbolic if A is diagonalizable with real eigenvalues. Let λ^p and r^p denote the eigenvalues and eigenvectors respectively. Since A is diagonalizable, the set $\{r^p, p = 1, \dots, m\}$ is linearly independent and then, it is a basis of \mathbb{R}^m . Any solution of the system of equations 2.12 can

2. ELECTRO-HYDRODYNAMIC MODEL

be written as a linear superposition of m waves

$$q(x, t) = \sum_{p=1}^m \omega^p(x, t) r^p, \quad (2.14)$$

where the $\omega^p(x, t)$ are known as characteristic variables. We can write previous equation in matrix form as

$$q(x, t) = R w(x, t), \quad (2.15)$$

where R is the matrix of the right eigenvectors in columns and w is the vector q in the basis $\{r^p\}$. Under these conditions the inverse matrix R^{-1} exists (*LeVeque, 2002*) and we can express the system of equations 2.12 in terms of the characteristic variables as

$$\omega_t + \Lambda \omega_x = 0. \quad (2.16)$$

Here, $\Lambda = R^{-1} A R$ is a diagonal matrix obtained by writing A in the basis of eigenvectors. What we have now is a set of m decoupled scalar equations

$$\omega_t^p + \lambda^p \omega_x^p = 0. \quad (2.17)$$

Any of these equations is a simple advection equation with a solution of the form

$$\omega^p(x, t) = \omega^p(x - \lambda^p t, t = 0) = \omega_0^p(x - \lambda^p t). \quad (2.18)$$

This implies that the solution at (x, t) depends on the initial data at the set of points $\{x - \lambda^p t\}$. Then, we can define a domain of influence of the point (\bar{x}, \bar{t}) as

$$\mathcal{D}(\bar{x}, \bar{t}) = \{x = \bar{x} + \lambda^p \bar{t}, p = 1, \dots, m\}. \quad (2.19)$$

We can associate to the pair $\{\lambda^p, r^p\}$ and ω^p a one-parameter family of curves called characteristics that satisfy the following initial value problem (IVP)

$$\frac{dx(t)}{dt} = \lambda^p, \quad (2.20)$$

$$x(0) = x_0. \quad (2.21)$$

The solution to the IVP is

$$x(t) = x_0 + \lambda^p t. \quad (2.22)$$

Along the characteristics, ω^p fulfills:

$$\frac{d\omega^p(x(t), t)}{dt} = \frac{\partial\omega^p(x(t), t)}{\partial x} \lambda^p + \frac{\partial\omega^p(x(t), t)}{\partial t} = 0. \quad (2.23)$$

That is, the quantity ω^p remains constant and so the initial profile $\omega_0^p(x)$ propagates without distortion with characteristic speed λ^p .

2.3.5 Riemann problem

A Riemann problem consists of a hyperbolic system of equations (2.12) together with piecewise constant initial conditions of the form (figure 2.2)

$$q(x, t = 0) = \begin{cases} q_l & x < 0 \\ q_r & x > 0 \end{cases}. \quad (2.24)$$

In general, to find a numerical solution to the problem at hand, we require space and time discretization. In particular, when applying finite volume methods, we are introducing small discontinuities. In fact, we need to solve a Riemann problem repeatedly at every cell edge to advance the solution to the next time step.

As we saw in the previous section, the solution q is a superposition of m -waves ω^p (2.14) propagating at constant speed λ^p . Therefore, we can expand the initial data (2.24) in terms of the eigenvector basis:

$$q_l = \sum_p^m \omega_l^p r^p, \quad (2.25)$$

$$q_r = \sum_p^m \omega_r^p r^p. \quad (2.26)$$

2. ELECTRO-HYDRODYNAMIC MODEL

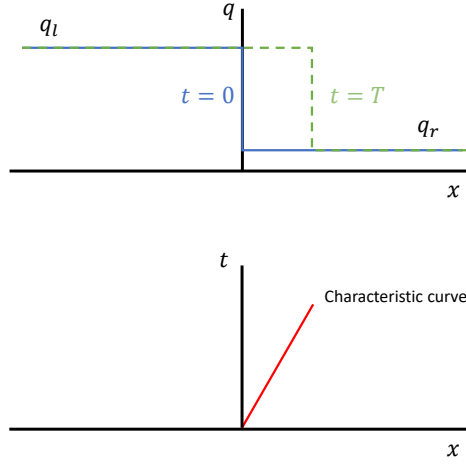


Figure 2.2: The Riemann problem is characterized by piecewise constant data q_l and q_r , jump discontinuities that propagate along characteristic curves. The characteristic curve tracks the position of the discontinuity along the x -axis.

In term of the characteristic variables, the initial conditions write as

$$\omega^p(x, t = 0) = \begin{cases} \omega_l^p & x < 0 \\ \omega_r^p & x > 0 \end{cases}, \quad (2.27)$$

and the solution is

$$\omega^p(x, t) = \begin{cases} \omega_l^p & x - \lambda^p t < 0 \\ \omega_r^p & x - \lambda^p t > 0 \end{cases}. \quad (2.28)$$

Note that q can be written as

$$q(x, t) = \sum_{p=1}^{P(x,t)} \omega_l^p r^p + \sum_{p=P(x,t)+1}^m \omega_r^p r^p, \quad (2.29)$$

where

$$P(x, t) = \sup \{p/x - \lambda^p t < 0\}. \quad (2.30)$$

If we consider the Riemann problem 2.24 with the characteristic curves sketched in figure 2.3, we can see that the states are constant in the wedges defined by them. Following the example depicted in fig. 2.3 we can write

$$q_l = \omega_l^1 r^1 + \omega_l^2 r^2 + \omega_l^3 r^3, \quad (2.31)$$

and

$$q_l^* = \omega_r^1 r^1 + \omega_l^2 r^2 + \omega_l^3 r^3. \quad (2.32)$$

Hence, when we cross a p -characteristic (horizontal dashed line in figure 2.3), in this case, that associated with λ^1 , there is a jump in q :

$$q_l - q_l^* = (\omega_l^1 - \omega_r^1) r^1. \quad (2.33)$$

Generally, the solution can be written in term of these jump discontinuities as follows:

$$q(x, t) = q_l + \sum_{\lambda^p < \frac{x}{t}} \alpha^p r^p = q_r + \sum_{\frac{x}{t} < \lambda^p} \alpha^p r^p, \quad (2.34)$$

$$\alpha^p \equiv \omega_r^p - \omega_l^p. \quad (2.35)$$

We will denote the discontinuity through the p -characteristic as $W^p \equiv \alpha^p r^p$ that we will call it the p -wave. Note that these waves (or jumps) are eigenvectors of the matrix A and verify the Rankine-Hugoniot condition:

$$f(\omega_r^p) - f(\omega_l^p) = A(\omega_r^p - \omega_l^p) r^p = \lambda_p (\omega_r^p - \omega_l^p) r^p. \quad (2.36)$$

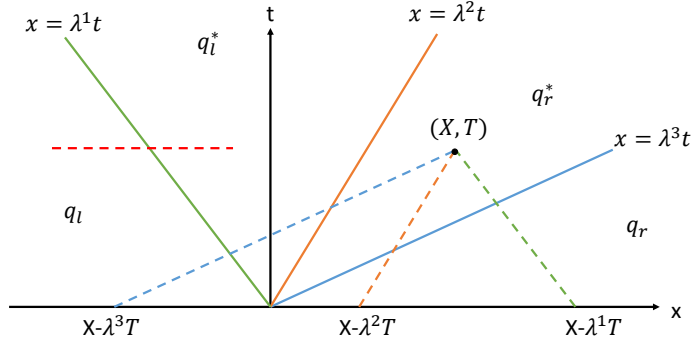


Figure 2.3: The initial discontinuity that separates the pair of constant states (q_l, q_r) splits into three jump discontinuities that propagate with characteristic speeds $\{\lambda^1, \lambda^2, \lambda^3\}$. As a result, two new intermediate states q_l^* and q_r^* are defined between the wedges limited by the characteristic curves.

2.3.6 Non-linear hyperbolic system

Many of the features that we have described for linear hyperbolic systems are valid for non-linear hyperbolic systems. Consider the one-dimensional system of equations

$$q_t(x, t) + f_x(q(x, t)) = 0, \quad (2.37)$$

with initial conditions

$$q(x, t = 0) = q_0(x), \quad (2.38)$$

where $q \in \mathbb{R}^m$ and $f \in \mathbb{R}^m$. In quasi-linear form

$$q_t(x, t) + A(q)q_x = 0, \quad (2.39)$$

being

$$A(q) = f'(q). \quad (2.40)$$

The system is said to be hyperbolic if the Jacobian $A(q)$ has real eigenvalues λ^p and linearly independent eigenvectors r^p for any $q \in \mathbb{R}^m$.

As we already did in the linear case, we could try to build a solution by following the characteristic curves. Locally, we can extend the definition of the characteristic in the following way:

$$\frac{dx}{dt} = \lambda^p(q) \tag{2.41}$$

$$x(0) = x_0. \tag{2.42}$$

As for the linear case,

$$x = x_0 + \lambda^p(q(x_0, 0))t. \tag{2.43}$$

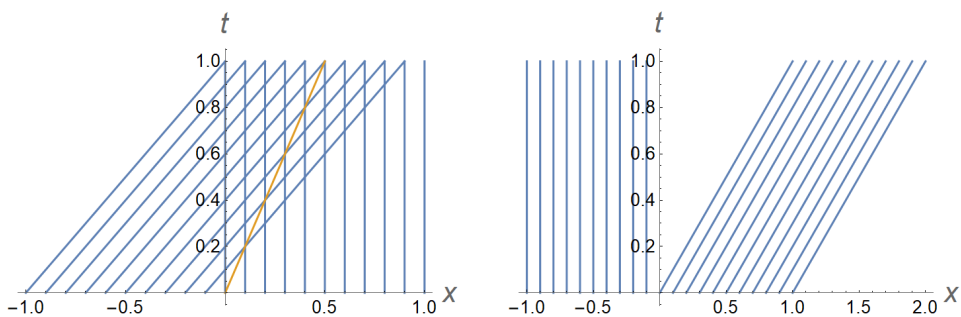


Figure 2.4: Example of colliding and diverging characteristic lines obtained from the inviscid Burgers equation $q_t + qq_x = 0$. The orange line on the left graph shows the shock wave front. On right graph, characteristics diverge and do not cover the entire x-t plane.

In the linear case we had that $\lambda(q) = \text{const.}$ and therefore the characteristic curves were parallel to each other. However, in the non-linear case, the characteristic speed depends on the solution itself, thus, in general, the characteristics are not parallel lines anymore

2. ELECTRO-HYDRODYNAMIC MODEL

and could cross at some point. This is a key feature of non-linear problems. The time at which the characteristics cross is known as the breaking time and from there, we cannot follow the evolution of the system with the characteristics approach. A classic example of a non-linear hyperbolic equation is Burgers equation (*LeVeque, 2002*):

$$q_t + qq_x = 0. \quad (2.44)$$

This apparently simple equation shows many of the features associated with non-linearity. Take a look at the left graph in figure 2.4. If we wanted to evolve the system up to a point (x^*, t^*) that belongs to the orange line, we could have come from two different initial states. Therefore, the solution is double-valued. However, this is not physically acceptable as we could not have two different density values at a point, for example. For the solution beyond the breaking time we need to allow for discontinuous solutions, that is, weak solutions, as we explained before.

Notice that, even though we had smooth initial data, the non-linearity may induce discontinuous solutions (figure 2.5) as the crossing of characteristics reveals. From the discussion above, the main consequences are (figure 2.4):

- Characteristics are straight lines.
- They may intersect with each other.
- They do not necessarily cover the entire (x, t) space.

2.3.7 Entropy condition and uniqueness

When it comes to weak solutions, uniqueness is not guaranteed. These weak solutions can be non-physical and violate fundamental principles in Physics. Therefore, we need a new constraint to properly isolate the physically acceptable weak solution. This condition is known as entropy condition and for smooth solutions is an equality of the form

$$s(q)_t + \psi(q)_x = 0, \quad (2.45)$$

where s is the conserved entropy and ψ is the entropy flux. For discontinuous solutions it is an inequality. A detailed discussion on this topic can be found in *LeVeque (2002)*.

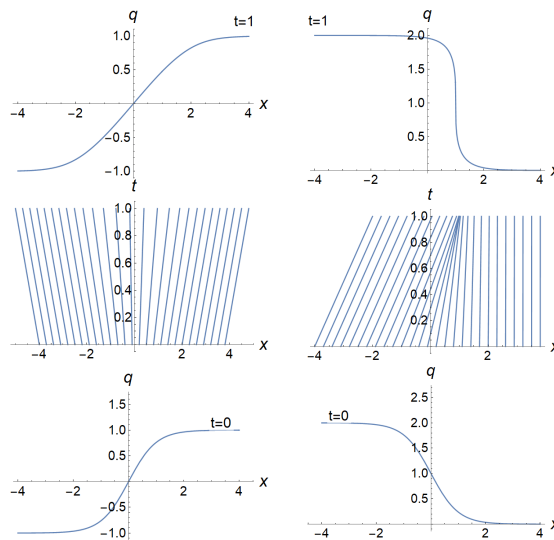


Figure 2.5: Solution of the inviscid Burgers equation (2.44) for two different initial conditions $q(x, t = 0) = \tanh(x)$ (left column) and $q(x, t = 0) = 1 - \tanh(x)$ (right column). This is a simple case that illustrates how non-linear hyperbolic equations can lead to discontinuities starting with smooth data. The second row shows the characteristic curves. On the left, they diverge giving rise to the so called rarefaction wave whereas on the right, they collide to form a shock wave.

2.3.8 Riemann problem for a non-linear hyperbolic system

In the linear case, the solution is a superposition of m propagating discontinuities traveling at the characteristic speeds of the linear system. In the non-linear case, the solution consists in a set of waves in each characteristic family, separating regions where the solution is constant. These waves may be discontinuities such as shocks (right column in figure 2.5) and contact discontinuities or smooth transition waves such as rarefaction waves (left column in figure 2.5). A rigorous and detailed treatment of this topic falls out of the scope of this chapter and therefore, we refer to *LeVeque* (2002) for the interested reader.

2.3.9 p -characteristic field: Linear degeneration and genuinely non-linear

In the previous section we mentioned that contact and shock waves are discontinuities. Here we characterize both of them. The p -characteristic field $\nabla \lambda^p$ is said to be degenerate

if

$$\nabla \lambda^p \cdot r^p \equiv 0 \quad \forall q \in \Omega, \quad (2.46)$$

and genuinely non-linear if

$$\nabla \lambda^p \cdot r^p \neq 0 \quad \forall q \in \Omega. \quad (2.47)$$

A shock wave is a discontinuity in a genuinely non-linear p -characteristic. On the other hand, a contact discontinuity is a discontinuity in a linearly degenerated field. As with any discontinuity, both need to verify the Rankine-Hugoniot condition.

2.4 Finite Volume Methods

In this section, we will work out the basics of finite volume methods (FVM) in one dimension. The numerical solution in higher dimensions can be accomplished by repeatedly applying the one-dimensional approach. For a more thoughtful discussion on this and higher dimensions, see *LeVeque* (2002). FVM allow us to solve numerically integral conservation laws (2.5). This is an advantage over Finite Difference methods when considering discontinuous solutions. In FVM, we start by discretizing our computational domain and then we average the solution to form the numerical approximation to 2.5. Let us consider a grid cell $C_i \in [x_{i-\frac{1}{2}}, x_{i+\frac{1}{2}}]$. In each grid cell, at time t_n we define the quantities

$$Q_i^n \approx \frac{1}{\Delta x} \int_{C_i} q(x, t_n) dx, \quad (2.48)$$

$$F_{i\pm\frac{1}{2}}^n \approx \frac{1}{\Delta t} \int_{C_i} f\left(q\left(x_{i\pm\frac{1}{2}}, t_n\right)\right), \quad (2.49)$$

where Δx is the grid cell length and Δt is the time step used to advance our solution from t_n to t_{n+1} . Q_i^n and $F_{i\pm\frac{1}{2}}^n$ are an approximation to the "volume" average of the conserved quantities q and the flux. If we apply the integral form of the conservation law to the cell C_i , we get

$$Q_i^{n+1} - Q_i^n = -\frac{\Delta t}{\Delta x} \left(F_{i+\frac{1}{2}}^n - F_{i-\frac{1}{2}}^n \right). \quad (2.50)$$

This equation is the fundamental numerical scheme of finite volume methods. As the continuous counterpart, the discrete scheme reflects the fact that changes in the solution in cell C_i are due to the flux through the boundaries. This idea is captured in figure 2.6. One of the key tasks when applying finite volume methods is to find the proper numerical flux. As we have seen, in hyperbolic problems information travels at a finite speed, therefore, it is reasonable to think that at first order, the numerical flux at t_n and $x_{i+\frac{1}{2}}$ is a function of the left and right states Q_i^n and Q_{i+1}^n

$$F_{i+\frac{1}{2}}^n = \mathcal{F}(Q_i^n, Q_{i+1}^n). \quad (2.51)$$

Hence, for sufficiently small time steps Δt , only the adjacent cells affect our solution in the cell C_i . We can rewrite equation 2.50 as

$$Q_i^{n+1} = Q_i^n - \frac{\Delta t}{\Delta x} \left[\mathcal{F}(Q_i^n, Q_{i+1}^n) - \mathcal{F}(Q_i^n, Q_{i-1}^n) \right]. \quad (2.52)$$

The specific method to advance the system from $Q_i^n \rightarrow Q_i^{n+1}$ depends on the function \mathcal{F} . However, any of them will be an explicit 3-point stencil method.

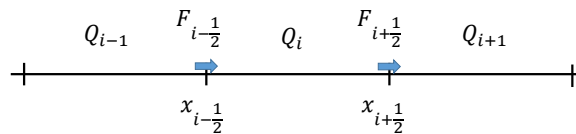


Figure 2.6: Discontinuity propagating with speed s , separating the pair of constant states (q_l, q_r) .

2.4.1 The Courant-Friedrichs-Lewy (CFL) condition

As we said, it is reasonable to think that at first order the numerical flux is a function of the left and right states around the cell edge. We can make this statement more precise by limiting the length of the time step, making sure that only information coming from the immediately adjacent grid cells is crossing the edge $x_{i+\frac{1}{2}}$. The CFL condition is what we are looking for and in fact, it is a necessary condition for our FVM to be numerically stable (*LeVeque*, 2002). Any FVM must fulfill the CFL condition given by the inequality:

$$\lambda \frac{\Delta t}{\Delta x} \leq 1. \quad (2.53)$$

The propagating speed (λ) of the wave is an outcome, while the space resolution is fixed by the requirements of the phenomenon that we want to explore. We are left with one degree of freedom, the time step that we will have to vary depending on the two other parameters.

2.4.2 First order Godunov's method for hyperbolic linear systems

Godunov introduced his method as an approach to solving the Euler equations of gas dynamics. If we approximate the solution $q(x, t)$ at the cell C_i by means of the corresponding cell average, that is

$$q(x_i, t_n) \approx \tilde{q}(x_i, t_n) = Q_i^n, \quad (2.54)$$

we have the following Riemann problem at each cell edge $x_{i-\frac{1}{2}}$:

$$\tilde{q}(x, t_n) = \begin{cases} Q_i^n & x_{i-\frac{1}{2}} < x, \\ Q_{i-1}^n & x < x_{i-\frac{1}{2}}. \end{cases} \quad (2.55)$$

Therefore, advancing our solution a time step at C_i according to 2.52 requires solving two Riemann problems at the left and right edges of the cell. As we have seen in previous sections, the Riemann problem centered at $x_{i-\frac{1}{2}}$ has a similarity solution that is constant along the ray

$$\frac{x - x_{i-\frac{1}{2}}}{t - t_n} = \text{const.} \quad (2.56)$$

Let us denote the exact solution to the Riemann problem at $x_{i-\frac{1}{2}}$ and t_n by $q_\downarrow(Q_{i-1}^n, Q_i^n)$, if the time step, that is $|t_{n+1} - t_n|$, is small enough, then we have that

$$F_{i-\frac{1}{2}}^n = \frac{1}{\Delta t} \int_{t_n}^{t_{n+1}} f\left(q_\downarrow(Q_{i-1}^n, Q_i^n)\right) dt = f\left(q_\downarrow(Q_{i-1}^n, Q_i^n)\right). \quad (2.57)$$

In summary, Godunov's method consists of the following steps:

1. At each time step t , solving the Riemann problem at each grid edge $x_{i-\frac{1}{2}}$ with left and right states (Q_{i-1}, Q_i) to compute $q_\downarrow(Q_{i-1}^n, Q_i^n)$.
2. Compute the flux $F_{i-\frac{1}{2}}^n = \mathcal{F}(Q_{i-1}^n, Q_i^n)$ by means of equation 2.57.
3. Advance the solution to the next step by using the flux difference equation 2.50.

2.4.3 Approximate Riemann solvers

Finding the exact solution to a Riemann problem is computationally intensive, specially for non-linear hyperbolic systems and higher-dimensional problems. The exact solution of a Riemann problem requires finding the full-wave structure and wave speeds to locate where the information is coming from at a specific point. Many times it suffices to find an exact solution to an approximate Riemann problem at each cell interface. Approximate Riemann solvers are cheaper than the exact solvers and results are fairly good. However, they also come with other issues as we will briefly see. A typical approach consists of using a local linearized Jacobian:

$$f'(q) \rightarrow \hat{A}(q_l, q_r), \quad (2.58)$$

where \hat{A} is a constant matrix. By solving this related Riemann problem, we can determine the numerical flux and advance our solution to the next time step according to what we have discussed so far.

The matrix \hat{A} must fulfill some basic requirements such as having real eigenvalues $\{\lambda^p\}$ and a set of linearly independent eigenvectors $\{r^p\}$. The matrix \hat{A} should also smoothly converge to the Jacobian matrix

$$q_l, q_r \rightarrow q \implies \hat{A}(q_l, q_r) \rightarrow f'(q). \quad (2.59)$$

As we have already explained, the solution to a linear Riemann problem consists of a set of traveling waves W_p propagating at a given speed by the eigenvalues λ^p of the Jacobian. In some cases it is also required that the approximate solution is conservative, that is, it obeys a conservation law in a region surrounding the Riemann solution

$$f(q_r) - f(q_l) = \sum_p \lambda^p W^p. \quad (2.60)$$

The right-hand side represents the rate of change of the solution due to the moving jump discontinuities and the left-hand side net effect of the fluxes.

2.4.4 Roe's solver

Roe's solver is one of the most popular approximated Riemann solvers. It was originally proposed by Roe to solve the Euler equations. The idea here is to determine a solution \hat{q} to the Riemann problem given by

$$\hat{q}_r + \hat{A}(q_l, q_r) q_x = 0, \quad (2.61)$$

where $\hat{A}(q_l, q_r)$ is a locally linearized version of the original Jacobian $f'(q)$. The issue now is to determine the linear matrix. Roe suggested the following:

1. $\hat{A}(q_l, q_r)(q_r - q_l) = f(q_r) - f(q_l)$.
2. $\hat{A}(q_l, q_r)$ is diagonalizable with real eigenvalues.
3. $q_l, q_r \rightarrow q \implies \hat{A}(q_l, q_r) \rightarrow f'(q)$ smoothly.

The first condition has two nice effects. One is that any flux-difference splitting defined with the linear matrix \hat{A} , will be a flux-difference splitting with the true flux. The other is that if we consider a solution consisting of just a single shock wave we can solve this exactly:

$$s(q_r - q_l) = f(q_r) - f(q_l) = \hat{A}(q_l, q_r)(q_r - q_l). \quad (2.62)$$

The first equality is the Rankine-Hugoniot condition and the second equality holds due to the first point. Essentially, we have that the difference $q_r - q_l$ is an eigenvector of the matrix $\hat{A}(q_l, q_r)$. In this case, the approximate solution is also conservative.

A way to fulfill points 1. and 2. is to build \hat{A} upon what is named as Roe's average state $\hat{q}(q_l, q_r)$

$$\hat{A}(q_l, q_r) = f'(\hat{q}(q_l, q_r)). \quad (2.63)$$

This Roe's average state depends on the system in particular. An extensive discussion about this can be found in *LeVeque (2002)*.

Godunov's method gives weak solutions satisfying correct entropy conditions. However, approximate Riemann solvers are discontinuous and converge to discontinuous entropy violating conditions, even when the solution is a smooth rarefaction wave. Roe's solver is prone to this kind of problem and requires an "entropy fix", which consists of using an entropy condition (see section 2.3.7).

2.4.5 Wave propagation algorithms

Godunov's method was originally built upon flux-differences. Nonetheless, there is an alternative and useful approach. The solution to a Riemann problem at $x_{i-\frac{1}{2}}$ can be seen as a series of jumps $W_{i-\frac{1}{2}}^p$ propagating at speed $s_{i-\frac{1}{2}}^p$, so we can express the jump with left and right states (Q_{i-1}^n, Q_i^n) as

$$Q_i^n - Q_{i-1}^n = \sum_p^{M_w} W_{i-\frac{1}{2}}^p. \quad (2.64)$$

A right-going wave $W_{i-\frac{1}{2}}^p$ will modify Q_i^n an amount $\frac{\Delta t}{\Delta x} s_{i-\frac{1}{2}}^p W_{i-\frac{1}{2}}^p$. Analogously, at the edge $x_{i+\frac{1}{2}}$, the left going wave $W_{i+\frac{1}{2}}^p$ will modify Q_i^n an amount $\frac{\Delta t}{\Delta x} s_{i+\frac{1}{2}}^p W_{i+\frac{1}{2}}^p$, so that the net effect on Q_i^n can be written as:

$$Q_i^{n+1} = Q_i^n + \frac{\Delta t}{\Delta x} \left[\sum_p \left(s_{i-\frac{1}{2}}^p \right)^+ W_{i-\frac{1}{2}}^p + \sum_p \left(s_{i+\frac{1}{2}}^p \right)^- W_{i+\frac{1}{2}}^p \right]. \quad (2.65)$$

Note that the wave has gone through a re-averaging process by multiplying by the factors $\frac{s_{i\pm\frac{1}{2}}^p}{\Delta x}$. If we denote $\mathcal{A}^+ \Delta Q_{i-\frac{1}{2}} \equiv \sum_p \left(s_{i-\frac{1}{2}}^p \right)^+ W_{i-\frac{1}{2}}^p$ and $\mathcal{A}^- \Delta Q_{i+\frac{1}{2}} \equiv \sum_p \left(s_{i+\frac{1}{2}}^p \right)^- W_{i+\frac{1}{2}}^p$, we can write the expression above as

$$Q_i^{n+1} = Q_i^n + \frac{\Delta t}{\Delta x} \left[\mathcal{A}^+ \Delta Q_{i-\frac{1}{2}} + \mathcal{A}^- \Delta Q_{i+\frac{1}{2}} \right]. \quad (2.66)$$

2. ELECTRO-HYDRODYNAMIC MODEL

$\mathcal{A}^- \Delta Q_{i-\frac{1}{2}}$ and $\mathcal{A}^+ \Delta Q_{i+\frac{1}{2}}$ are called left and right going fluctuations respectively and represent the net effect of the left and right going waves on the cell average Q_i^n . This approach is applicable for hyperbolic systems in non-conservative form. When applied to hyperbolic systems in conservative form, this approach has to verify

$$f(Q_i) - f(Q_{i-1}) = \mathcal{A}^+ \Delta Q_{i-\frac{1}{2}} + \mathcal{A}^- \Delta Q_{i+\frac{1}{2}}. \quad (2.67)$$

If we use an approximate Riemann solver, the above relation is equivalent to

$$f(Q_i) - f(Q_{i-1}) = \sum_p^{M_w} s_{i-\frac{1}{2}}^p W_{i-\frac{1}{2}}^p. \quad (2.68)$$

2.4.6 High resolution methods

As we have seen through the chapter, discontinuities readily appear when solving hyperbolic equations. So far we have described Godunov's method, which uses an exact or approximate solution of the Riemann problem and does not produce oscillations around shock or contact discontinuities. However, it is first-order accurate and it smooths discontinuities out and shows slow convergence around them. Higher-order methods such as Lax-Wendroff, are second-order away from discontinuities and exhibit spurious oscillations near them. This calls for high-resolution methods able to describe sharp transition regions while accurate in smooth regions. Godunov's method seems to be a good starting point but we need to revise it to improve it. Godunov's method is based upon a piecewise constant reconstruction

$$\tilde{q}(x, t_n) = Q_i^n \quad \forall x \in C_i, \quad (2.69)$$

which results in an overall first-order accurate method.

We can improve this by allowing a linear dependence on x (figure 2.7):

$$\tilde{q}(x, t_n) = Q_i^n + \sigma_i^n (x - x_i) \quad \forall x \in C_i. \quad (2.70)$$

The slope essentially brings the idea of smoothness but it can also lead to overshooting. Figure 2.7 shows how overshoots in the piecewise linear reconstruction function produce

overshoots in the solution. Slope limiter methods prevent these overshoots. Slope limiters are a topic of research on their own. For more details, see *LeVeque (2002)*. In summary, high-resolution methods achieve better accuracy by adding second-order corrections to the first-order method. After adding these corrections, 2.52 is read as:

$$Q_i^{n+1} = Q_i^n - \frac{\Delta t}{\Delta x} \left(\mathcal{A}^- \Delta Q_{i+\frac{1}{2}} + \mathcal{A}^+ \Delta Q_{i-\frac{1}{2}} \right) - \frac{\Delta t}{\Delta x} \left(\tilde{F}_{i+\frac{1}{2}} - \tilde{F}_{i-\frac{1}{2}} \right), \quad (2.71)$$

where the second-order correction to the fluxes $\tilde{F}_{i\pm\frac{1}{2}}$ is given by

$$\tilde{F}_{i\pm\frac{1}{2}} = \frac{1}{2} \sum_{p=1}^m \left| s_{i\pm\frac{1}{2}}^p \right| \left(1 - \frac{\Delta t}{\Delta x} \left| s_{i\pm\frac{1}{2}}^p \right| \right) \left(\phi W_{i\pm\frac{1}{2}}^p \right), \quad (2.72)$$

with ϕ being a limiter function.

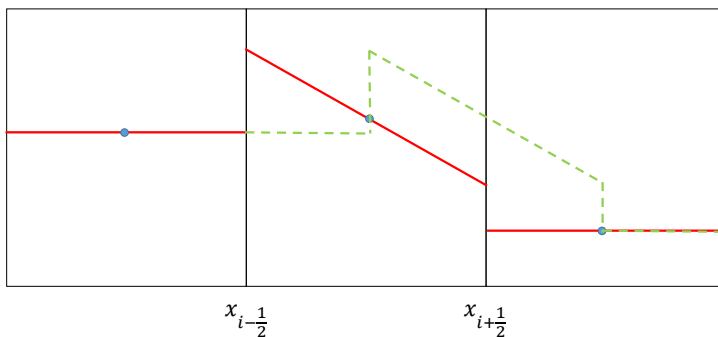


Figure 2.7: An overshoot in the piece-wise linear reconstruction (red solid line) 2.70 can lead to an overshoot in the solution (green solid line).

2.4.7 Multidimensional systems

So far we have been working with 1D hyperbolic systems of equations. The algorithms described above can be extended to higher dimensions. Essentially, at each cell interface

2. ELECTRO-HYDRODYNAMIC MODEL

we need to solve a 1-dimensional problem. For a 2-dimensional system the cell average is:

$$Q_{i,j}^n = \frac{1}{\Delta x \Delta y} \int \int \tilde{q}(x, y, t) dx dy. \quad (2.73)$$

In terms of the flux difference, the change in $Q_{i,j}^n$ is given by

$$Q_{i,j}^{n+1} - Q_{i,j}^n = -\frac{\Delta t}{\Delta x} \left(F_{i+\frac{1}{2},j}^n - F_{i-\frac{1}{2},j}^n \right) - \frac{\Delta t}{\Delta y} \left(G_{i+\frac{1}{2},j}^n - G_{i-\frac{1}{2},j}^n \right), \quad (2.74)$$

and in terms of the fluctuations

$$Q_{i,j}^{n+1} = Q_{i,j}^n - \frac{\Delta t}{\Delta x} \left(\mathcal{A}^- \Delta Q_{i+\frac{1}{2},j} + \mathcal{A}^+ \Delta Q_{i-\frac{1}{2},j} \right) - \frac{\Delta t}{\Delta y} \left(\mathcal{B}^- \Delta Q_{i+\frac{1}{2},j} + \mathcal{B}^+ \Delta Q_{i-\frac{1}{2},j} \right). \quad (2.75)$$

If we go to a higher dimension, we would have to add similar terms to the equation above. However, this is just first-order. If we wanted to include second order corrections, the previous equation is rewritten in the following way:

$$Q_{i,j}^{n+1} = Q_{i,j}^n - \frac{\Delta t}{\Delta x} \left(\mathcal{A}^- \Delta Q_{i+\frac{1}{2},j} + \mathcal{A}^+ \Delta Q_{i-\frac{1}{2},j} \right) - \frac{\Delta t}{\Delta x} \left(\mathcal{B}^- \Delta Q_{i,j+\frac{1}{2}} + \mathcal{B}^+ \Delta Q_{i,j-\frac{1}{2}} \right) - \frac{\Delta t}{\Delta x} \left(\tilde{F}_{i+\frac{1}{2},j} - \tilde{F}_{i-\frac{1}{2},j} \right) - \frac{\Delta t}{\Delta y} \left(\tilde{G}_{i,j+\frac{1}{2}} - \tilde{G}_{i,j-\frac{1}{2}} \right). \quad (2.76)$$

2.4.8 Source terms

In our derivations we have only considered conservation equation laws and not balance equations. The most popular method to solve an equation of the form

$$q_t + q_x = \Psi \quad (2.77)$$

is the fractional step method, which consists of solving at each time step the conservation equation

$$q_t + q_x = 0, \quad (2.78)$$

and then solving

$$q_t = \Psi. \quad (2.79)$$

This is a quite simple but robust approach in most cases. However, this method does not work well when there is an steady-state since $q_x \approx \Psi$. As a result, the fractional step method is not able to properly resolve the steady-state. For our purpose in this thesis, the fractional step method will be enough.

2.5 Poisson's equation

In the set of equations that we want to solve, the electric field appears explicitly in the advection terms but also implicitly through parameters such as the mobility of charged species or the rate coefficients in the source terms. The determination of the electric field with enough accuracy is fundamental when dealing with propagation phenomena such as streamer discharges. In these discharges, a high electric field is confined to regions whose thickness is just a few micrometers at atmospheric pressure.

Poisson's equation is an elliptic partial differential equation that relates the electric potential and its sources. The problem at hand consists of a boundary value problem (BVP),

$$\begin{aligned} \Delta\phi(\mathbf{x}) &= f(\mathbf{x}), \quad \mathbf{x} \in \Omega \\ \phi(x) &= g(x), \quad \mathbf{x} \in \partial\Omega \end{aligned} \quad (2.80)$$

where $f(\mathbf{x}) = -\sum_s \frac{q_s n_s(\mathbf{x})}{\epsilon_0}$ and $g(x)$ denotes the boundary conditions. Unfortunately, this BVP is analytically solvable in very few cases, with simple charge distributions and domain geometries. This calls for numerical methods that provide a way to solve such a fundamental equation in physics.

2.5.1 Discretization

Finite difference methods approximate derivatives with finite differences. We start from ordinary/partial differential equations (O/PDE) and transform them into a system of linear

2. ELECTRO-HYDRODYNAMIC MODEL

equations that can be solved with different numerical methods that we will shortly describe later. Since we are working with a 2-D cylindrically symmetric system, the Laplacian operator in equation 2.80 takes the form:

$$\Delta \doteq \frac{1}{r} \frac{\partial}{\partial r} \left(r \frac{\partial}{\partial r} \right) + \frac{\partial^2}{\partial z^2}, \quad (2.81)$$

where r represents the radial coordinate and z the axial coordinate.

Now we discretize our computational domain by means of a grid with uniform spacing $\Delta r = \Delta z = h$. Each node is labeled by the pair (i, j) , with coordinates $r_i = \frac{h}{2} + (i - 1)h$ for $i = 1, \dots, m$ and $z_j = \frac{h}{2} + (j - 1)h$ for $j = 1, \dots, n$. We will be working in a staggered grid and then we will calculate the electric field at the cell faces. The potential at each node $\phi(r_i, z_j)$ is denoted by ϕ_{ij} . For our study, we require a second order approximation of the derivatives. Then, Poisson's equation is written in the following way:

$$\phi_{i+1,j} \left(1 + \frac{h}{2r_{i,j}} \right) + \phi_{i-1,j} \left(1 - \frac{h}{2r_{i,j}} \right) - 4\phi_{i,j} + \phi_{i,j+1} + \phi_{i,j-1} = h^2 f_{i,j}. \quad (2.82)$$

This can be rearranged as a linear system, in a matrix form $\mathbf{Ax} = \mathbf{b}$ where

$$\mathbf{X} = (\phi_{11}, \phi_{21}, \phi_{31}, \dots, \phi_{12}, \dots)^T, \quad (2.83)$$

\mathbf{A} contains the coefficients of the linear system and \mathbf{b} contains the inhomogeneous terms.

2.5.2 Boundary conditions

As we have argued, our problem is complete when we consider some boundary conditions. The two most common boundary conditions are Dirichlet and Neumann. In Dirichlet boundary conditions, the potential is specified at the boundary,

$$\phi_{i,n+1} = 2\phi_{i,n+\frac{1}{2}} - \phi_{i,n}. \quad (2.84)$$

In Neumann boundary conditions, what we specify is the value of the electric field. So for a null electric field at the boundaries

$$\phi_{i,n+1} = \phi_{i,n}. \quad (2.85)$$

2.5.3 Poisson's solvers

Now that we have got Poisson's equation as a linear system, we need the methods to solve it. There are two main categories of solvers, iterative and direct. Iterative methods start with an initial guess and improve it after each iteration until convergence is achieved. They only need matrix multiplication and there is no need to access matrix elements. However, their efficiency depends on good preconditioners. On the other hand, direct solvers go through different steps as converting the system of equations into an augmented matrix, then an upper-triangular matrix and finally solve. After a certain number of steps, we arrive at a final solution. Direct solvers are more computationally expensive however they are very good at solving small matrices reliably and quickly.

2.6 Numerical code

The hydrodynamic and advection-diffusion-reaction part of our numerical code is built upon CLAWPACK/PETCLAW (*Alghamdi et al.*, 2011; *LeVeque*, 2002), a library that implements Finite Volume Methods. PETCLAW is built upon PETSc (*Balay et al.*, 2016a,b) and allows us to split the simulation domain into different subdomains (problems) that can be solved in parallel. Poisson's equation is solved using the Improved Stabilized version of BiConjugate Gradient solver from the PETSc numerical library. The adaptive time-step is constrained by a Courant-Friedrichs-Lewy number, the shortest chemical time scale $\tau_s = n_s(dn_s/dt)^{-1}$ and the Maxwell relaxation time (eq. 1.20) among all species s . A few samples of our code are available at https://gitlab.com/amaro/space_stem and <https://gitlab.com/amaro/streamer2d>.

2. ELECTRO-HYDRODYNAMIC MODEL

Chapter 3

A domain-decomposition method to implement electrostatic free boundary conditions for electric discharges

3.1 Introduction

In this thesis, we deal with leader and streamer discharges, which are characterized by a large aspect ratio $\frac{Length}{Width}$. For instance, streamers are thin filaments of ionized air that precede most electric discharges in long gaps at atmospheric pressure. The main challenge for simulating streamers is the wide separation between length scales: whereas the total length of the streamer channel at atmospheric pressure ranges from about one to some tens of centimeters, the ionization of air molecules is mostly confined to a layer thinner than one millimeter. Despite this difficulty, there are many numerical codes that explain most of the observed properties of streamers *Ebert et al. (2006)*; *Liu and Pasko (2006)*; *Luque and Ebert (2012)*; *Liu et al. (2015)*; *Qin and Pasko (2015)*; *Teunissen and Ebert (2018)*. In the past decades these models have gradually improved and successfully overcome many of the challenges posed by streamer physics. However, they are still computationally intensive and often require days of runtime to produce meaningful simulations.

3. A DOMAIN-DECOMPOSITION METHOD TO IMPLEMENT ELECTROSTATIC FREE BOUNDARY CONDITIONS FOR ELECTRIC DISCHARGES

In this chapter, we look at one of the problems that prominently impacts numerical codes built upon uniform grids and that is behind these long running times: the large aspect ratio of a single-channel discharge. Whereas the width of an atmospheric-pressure streamer is at most about one centimeter, its length spans many times this extension. In order to minimize the amount of work performed in a simulation, one strives to adapt the computational domain to the dimensions of the streamer, which means using a narrow cylindrical domain with a diameter only slightly larger than the streamer width. However, in such a narrow domain the electrostatic interaction between separate points in the channel is strongly affected by the boundary conditions imposed on the electric potential at the outer boundaries.

One widespread approach used in streamer simulations to avoid this artifact while keeping a narrow domain around the streamer is to calculate the boundary values of the potential by direct integration of the electrostatic Green's function in free space *Babaeva and Naidis* (1996, 2000); *Liu and Pasko* (2004, 2006); *Bourdon et al.* (2007):

$$\phi(\mathbf{r}_{boundary}) = \int_{\Omega} \frac{\rho_c(\mathbf{r}')}{|\mathbf{r}_{boundary} - \mathbf{r}'|} dV'. \quad (3.1)$$

These values are then imposed as inhomogeneous Dirichlet boundary conditions in the solution of the Poisson equation. In a cartesian grid with M cells in the radial direction and N cells in the axial direction the direct integration of the Green's function at each of the N nodes in the external boundary requires about MN^2 operations. Since the work employed by fast Poisson solvers scales as $MN \log(MN)$ (MN for multigrid solvers), the computation of boundary values by direct integration may easily dominate the work employed in the electrostatic calculations. This is mitigated in part by using a coarse-grained charge distribution in the integration. However, in that case there is a tradeoff between the degree of coarsening and the minimal radial extension of the domain required for a tolerable error.

Another simple and common approach affordable for codes that incorporate Adaptive Mesh Refinement (AMR) techniques is to make a sufficiently large domain so that the boundary conditions effects are negligible.

Beyond these common approaches used to solve Poisson's equation in electric discharges, some other methods have been developed. A family of these methods has been

built upon the idea of the decoupling of local and far-field effects (*Anderson, 1986*) and the computation of the boundary potential by means of a potential generated by a set of screening charges located in the outer surface of the computational domain (*James, 1977*). Based on these two methods mentioned above, *Balls and Colella (2002)* use a domain decomposition approach to exploit parallel computing capabilities; first, Poisson's equation subject to unbounded boundary conditions is solved in a set of disjoint patches. As a second step a coarse-grid representation of the space charge is obtained and Poisson's equation is again solved in a global coarse-grid whose solution is used to communicate far-field effects to local patches. Finally, Poisson's equation is solved in a fine grid using boundary conditions computed from the coarse-grid solution corrected with local field information.

A different family of methods uses the convolution with Green's function subject to free boundary conditions. They manage the singular behaviour of Green's function by either regularizing it (*Hejlesen et al., 2013*), or by replacing the singular component to the integrand of the convolution by an analytical contribution (*Anderson, 2016*). These methods have achieved an order of convergence greater than two.

In this chapter, we adapt to the cylindrical geometry of electric discharges the domain-decomposition method described by *Anderson (1989)* (see also *Bayliss et al. (1982)* for a review of similar techniques). In section 3.2 we will apply the method to a discharge that develops between two planar electrodes. As we discuss below, this method requires two calls to the Poisson solver but otherwise the leading term in its algorithmic complexity follows the scaling of the Poisson solver itself. Therefore for large grid sizes our approach is more efficient than the direct integration method. Furthermore, as we do not reduce the resolution, we do not introduce any numerical error in addition to the discretization error of the Poisson equation. We believe that the method we present is simple enough that it can be easily implemented on top of any existing streamer simulation code. As a benchmark, we present a simple test of a spherical charge density. We have also applied the domain-decomposition method to our streamer codes and we present the results too.

Some applications may also require free boundary conditions for the z -direction: for instance, when the discharge develops far from the electrodes. In those cases one may also reduce the computational domain in the longitudinal direction while the core of the

simulation remains inside the computational domain. We have considered this topic of interest in section 3.3 where we have applied the domain decomposition method to obtain free boundary conditions also in the longitudinal direction. This extension requires an extra solution of Poisson's equation. To test our approach, we have run several streamer simulations, where the streamer develops far from one of the electrodes that we set at infinity by applying free boundary conditions at $z = L$.

Note that streamers are not the only type of discharge that typically exhibits a large aspect ratio and that therefore our scheme is also applicable to other processes such as leaders and arcs.

3.2 Electrostatic free boundary conditions in the radial direction

3.2.1 Domain decomposition

The most convenient decomposition of the domain depends on the problem at hand. The decomposition we present here is suitable for elongated discharges and probably some other applications but the procedure and the highlighted ideas are not restricted to this particular scheme.

We consider the geometry sketched in figure 3.1, where an elongated, cylindrically symmetrical streamer propagates between two planar electrodes. With minimal changes, our scheme can be extended to more complex geometries commonly employed in streamer simulations, such as protrusion-plane, protrusion-protrusion and sphere-plane. The electrostatic potential ϕ satisfies the Poisson equation with appropriate boundary conditions:

$$\begin{aligned} \Delta\phi &= f & \text{in } \Omega, \\ \phi &= g & \text{on } \partial\Omega, \end{aligned} \tag{3.2}$$

where $f = -q/\epsilon_0$, with q being the charge density and ϵ_0 the vacuum permittivity. In principle an arbitrary boundary condition, here denoted by g , can be applied to the upper and lower electrodes. However, to simplify our discussion we limit ourselves to the most common case where $g = 0$, meaning $\phi = 0$ at $z = 0$ and $z = L$ (to impose a potential difference V between the two electrodes we simply add $\phi_{\text{inhom}} = zV/L$ to the solution

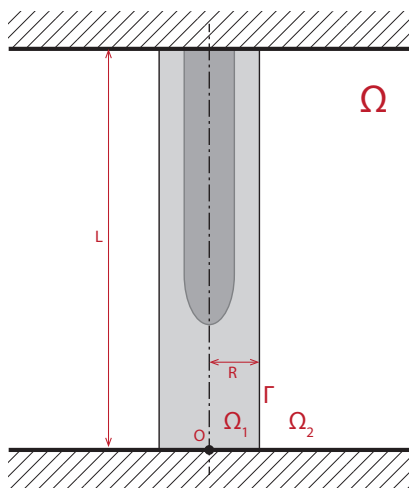


Figure 3.1: Geometry of the discharge considered in this work. An elongated channel propagates between two conducting electrodes. The space between these electrodes, Ω is divided into two domains: the inner domain Ω_1 is our computational domain and contains all the space charge. The outer domain Ω_2 extends indefinitely outwards from the external boundary of Ω_1 and does not contain any space charge. The cylindrical surface Γ is the common boundary between Ω_1 and Ω_2 .

3. A DOMAIN-DECOMPOSITION METHOD TO IMPLEMENT ELECTROSTATIC FREE BOUNDARY CONDITIONS FOR ELECTRIC DISCHARGES

of the homogeneous problem). The domain Ω is the space between the two electrodes, defined as

$$\Omega = \left\{ x \equiv (\rho, \theta, z) \in \mathbb{R}^3 / 0 \leq \rho, 0 \leq \theta < 2\pi, 0 \leq z \leq L \right\}. \quad (3.3)$$

Since our geometry is cylindrically symmetrical, we will henceforth omit the variable θ and consider the two-dimensional domain spanned by the variables (ρ, z) .

Our purpose is to decompose the physical domain Ω into two, which we name Ω_1 and Ω_2 , such that $\Omega = \overline{\Omega}_1 \cup \overline{\Omega}_2$ ($\overline{\Omega}_i$ is the closure of the set Ω_i), $\Omega_1 \cap \Omega_2 = \emptyset$ and $\text{supp}(f) \subset \Omega_1$, i.e. all the space charge is contained in Ω_1 . The inner domain Ω_1 , extending up to a given radius R , is our computational domain and therefore must be selected to be as narrow as possible.

Under this domain decomposition the problem (3.2) turns into two coupled problems:

$$\begin{aligned} \Delta\phi_i &= f & \text{in} & \quad \Omega_i, \\ \phi_i &= 0 & \text{on} & \quad \partial\Omega_i \setminus \Gamma, \\ \phi_i &= \phi_\Gamma & \text{on} & \quad \partial\Gamma, \end{aligned} \quad (3.4)$$

where $i = 1, 2$ and $\Gamma = \partial\Omega_1 \cap \partial\Omega_2$ is the cylindrical surface at $\rho = R$ that separates the two domains.

Since at the interface Γ both, ϕ_1 and ϕ_2 , are equal to the boundary value ϕ_Γ , they fulfill $\phi_1 = \phi_2$. But besides this condition, in order for ϕ_1 and ϕ_2 to be consistent with the solution ϕ of the original problem (3.2), they must also satisfy

$$\frac{\partial\phi_1}{\partial\rho} = \frac{\partial\phi_2}{\partial\rho} \text{ on } \Gamma. \quad (3.5)$$

The continuity of the radial derivatives follows from applying Gauss' law

$$\oint_{\partial A} \mathbf{E} \cdot d\mathbf{S} = \frac{1}{\varepsilon_0} \int_A \rho dV, \quad (3.6)$$

to a Gaussian pillbox A with two ends locally parallel to Γ . These ends can be made arbitrarily close together and, in the limit, the only contribution will be

$$\oint_{\partial A} \mathbf{E} \cdot d\mathbf{S} = -\frac{\partial\phi_1}{\partial\rho} + \frac{\partial\phi_2}{\partial\rho} = 0 \text{ on } \Gamma. \quad (3.7)$$

3.2.2 Linearity

The linearity of the Poisson problems (3.4) with respect to their sources f allows us to decompose the potentials as

$$\phi_i = \bar{\phi}_i[\phi_\Gamma] + \tilde{\phi}_i[f_i], \quad (3.8)$$

where $\bar{\phi}_i[\phi_\Gamma]$ results from the boundary values ϕ_Γ at the interface Γ and $\tilde{\phi}_i[f_i]$ results from the original sources f restricted to Ω_i (we use $[\cdot]$ to denote a functional dependence). The precise definitions read

$$\begin{aligned} \Delta \bar{\phi}_i &= 0 & \text{in } & \Omega_i, \\ \bar{\phi}_i &= 0 & \text{on } & \partial\Omega_i \setminus \Gamma, \\ \bar{\phi}_i &= \phi_\Gamma & \text{on } & \partial\Gamma, \end{aligned} \quad (3.9)$$

and

$$\begin{aligned} \Delta \tilde{\phi}_i &= f & \text{in } & \Omega_i, \\ \tilde{\phi}_i &= 0 & \text{on } & \partial\Omega_i \setminus \Gamma, \\ \tilde{\phi}_i &= 0 & \text{on } & \partial\Gamma. \end{aligned} \quad (3.10)$$

In terms of these components the flux equation (3.5) can be expressed as

$$\frac{\partial \bar{\phi}_1}{\partial \rho} [\phi_\Gamma] - \frac{\partial \bar{\phi}_2}{\partial \rho} [\phi_\Gamma] = - \frac{\partial \tilde{\phi}_1}{\partial \rho} [f] \text{ on } \Gamma, \quad (3.11)$$

where on the right-hand side we have used that $\tilde{\phi}_2 = 0$, since $f = 0$ in Ω_2 .

3.2.3 Expansion in orthonormal solutions of the Laplace equation

The potentials $\bar{\phi}_i$ in (3.9) are solutions of the Laplace equation in cylindrical geometry and they can be expanded using an orthogonal basis of solutions (see e.g. *Jackson (1975)*):

$$\bar{\phi}_1 = \sum_{m=1}^{\infty} \alpha_m I_0(k_m \rho) \sin(k_m z), \quad (3.12a)$$

$$\bar{\phi}_2 = \sum_{m=1}^{\infty} \beta_m K_0(k_m \rho) \sin(k_m z), \quad (3.12b)$$

where α_m and β_m are expansion coefficients, $k_m = m\pi/L$ and $I_n(x)$ and $K_n(x)$ are the modified n -order Bessel functions of the first and second kind respectively. Note that the set $S = \{\sin(k_m z)\}_{m=0}^{\infty}$ is an orthogonal basis of

$$\mathcal{L}^2([0, L]) = \left\{ f : [0, L] \mapsto \mathbb{R} : \int |f(z)|^2 dz < \infty \right\}, \quad (3.13)$$

3. A DOMAIN-DECOMPOSITION METHOD TO IMPLEMENT ELECTROSTATIC FREE BOUNDARY CONDITIONS FOR ELECTRIC DISCHARGES

that is, the space of real functions in $[0, L]$, with finite L^2 -norm.

Therefore, ϕ_Γ can be expanded as:

$$\phi_\Gamma(z) = \sum_{m=1}^{\infty} a_m \sin(k_m z). \quad (3.14)$$

If ϕ_Γ is continuous and piecewise differentiable on $[0, L]$, $\phi'_\Gamma \in \mathcal{L}^2([0, L])$ and ϕ_Γ satisfies homogeneous Dirichlet boundary conditions, then the sine series converges to ϕ_Γ uniformly on $[0, L]$. Note that the term with $m = 0$ vanishes due to the homogeneous boundary conditions at $z = 0$ and $z = L$.

The boundary conditions at $z = 0$ and $z = L$ restrict the basis of solutions. Homogeneous Dirichlet boundary conditions are simpler because there is only need for sine functions. However, if we had some other boundary conditions such as homogeneous Neumann, the convenient basis should also include cosine functions to allow for non-zero values of the potential at $z = 0$ and $z = L$.

3.2.4 Continuity of the normal derivative

Imposing that $\bar{\phi}_1 = \bar{\phi}_2 = \phi_\Gamma$ at $\rho = R$ we solve for α_m and β_m and write (3.12) as

$$\bar{\phi}_1 = \sum_{m=1}^{\infty} a_m \frac{I_0(k_m \rho)}{I_0(k_m R)} \sin(k_m z), \quad (3.15a)$$

$$\bar{\phi}_2 = \sum_{m=1}^{\infty} a_m \frac{K_0(k_m \rho)}{K_0(k_m R)} \sin(k_m z). \quad (3.15b)$$

Using these expressions into the equation for the normal derivatives (3.11) we obtain

$$\sum_{m=1}^{\infty} a_m k_m \left[\frac{I_1(k_m R)}{I_0(k_m R)} + \frac{K_1(k_m R)}{K_0(k_m R)} \right] \sin(k_m z) = - \frac{\partial \bar{\phi}_1}{\partial \rho} \Big|_{\rho=R}, \quad (3.16)$$

where we have used the identities $I'_0(x) = I_1(x)$, $K'_0(x) = -K_1(x)$. As we have expanded our solutions in terms of an orthogonal basis S , we can easily obtain equations for the coefficients a_m :

$$\frac{L}{2} k_m a_m \left[\frac{I_1(k_m R)}{I_0(k_m R)} + \frac{K_1(k_m R)}{K_0(k_m R)} \right] = - \int_0^L dz \sin(k_m z) \frac{\partial \bar{\phi}_1}{\partial \rho} \Big|_{\rho=R}. \quad (3.17)$$

In a space discretization based on a cartesian grid the integral in the latest expression is approximated by a finite sum with the form of a Discrete Sine Transform (DST). This leads to the following expression for the coefficients a_m

$$a_m = -\frac{2}{m\pi} \left[\frac{I_1(k_m R)}{I_0(k_m R)} + \frac{K_1(k_m R)}{K_0(k_m R)} \right]^{-1} \sum_{i=1}^N h \sin(k_m z_i) \left. \frac{\partial \tilde{\phi}_1}{\partial \rho} \right|_{\rho=R, z=z_i} + \mathcal{O}(h^2), \quad (3.18)$$

where h is the grid size and $\{z_i\}_{i=1}^N$ are the solution nodes in the z -direction. In a discrete problem the series in (3.14) is also truncated above $m = N$.

3.2.5 Algorithm

We are now ready to detail the domain-decomposition algorithm that allows us to solve the Poisson equation in the reduced computational domain Ω_1 with free boundary conditions in the radial direction:

1. Solve the Poisson equation in Ω_1 with the source term f and homogeneous Dirichlet boundary conditions at the boundary Γ . Call the result $\tilde{\phi}_1$.
2. Calculate the normal derivative of $\tilde{\phi}_1$ at Γ . Apply a DST and use expression (3.18) to obtain the coefficients a_m .
3. Use these coefficients to obtain the boundary values ϕ_Γ by means of a second DST and expression (3.14).
4. Solve again the Poisson equation in Ω_1 but now use ϕ_Γ as inhomogeneous Dirichlet boundary condition at Γ . The result, ϕ_1 is the solution of the Poisson equation with free boundary conditions.

To this algorithm we add the following remarks:

1. After obtaining the coefficients a_m one is tempted to use (3.15a) together with $\phi_1 = \bar{\phi}_1 + \tilde{\phi}_1$ to avoid solving the Poisson equation a second time. However, in a grid of $M \times N$ cells this procedure takes about MN^2 operations whereas solving the Poisson equation requires only $MN \log(MN)$ or MN operations.

3. A DOMAIN-DECOMPOSITION METHOD TO IMPLEMENT ELECTROSTATIC FREE BOUNDARY CONDITIONS FOR ELECTRIC DISCHARGES

2. The computational domain Ω_1 has to be as narrow as possible in order to reduce the computational cost of the simulation. Of course this narrowing is limited by the constraint that Ω_1 contains the support of the space charge density. In an electrostatic discharge the charge density typically decays smoothly away from the channel so in some cases one has to decide at which level it is safe to truncate the charge density with an acceptable error. Nevertheless, given the fast decay of the charge away from the channel, this is probably not a serious concern in most cases.

3.2.6 Tests and sample implementation

3.2.6.1 Tests

In order to test our scheme we consider now a simple setup where the Poisson equation has a closed-form solution. An example of such a configuration is an uniformly charged sphere located between two grounded, infinite planar electrodes. The electrostatic potential in this setup can be calculated by the method of images (see e.g. (*Jackson, 1975*)) and equals the potential created in free space by an infinite series of spheres with alternating charges.

Suppose a sphere centered at $(\rho, z) = (0, z_0)$ with radius $a < \min(z_0, L - z_0)$ and total charge Q . At a point with cylindrical coordinates (ρ, z) the potential reads

$$\phi(\rho, z) = \phi_0(\rho, z) + \frac{Q}{4\pi\epsilon_0} \sum_{\substack{k=-\infty \\ k \neq 0}}^{\infty} \frac{(-1)^k}{[\rho^2 + (z - z_0 - 2k(L - z_0))^2]^{1/2}}, \quad (3.19a)$$

with

$$\phi_0(\rho, z) = \frac{Q}{4\pi\epsilon_0} \begin{cases} \frac{1}{[\rho^2 + (z - z_0)^2]^{1/2}} & \text{if } \rho^2 + (z - z_0)^2 > a^2, \\ \frac{3a^2 - \rho^2 - (z - z_0)^2}{2a^3} & \text{if } \rho^2 + (z - z_0)^2 \leq a^2. \end{cases} \quad (3.19b)$$

Figure 3.2 shows a comparison between the electric fields computed using expression 3.19 and using the approach described in section 3.2. Here we took $a = 3$ mm, $L = 10$ mm, $Q = 10^{13}$ e (e is the elementary charge), $z_0 = L/2$. For the discretized solution we used $\Delta r = \Delta z = 10^{-2}$ mm and a radial extension of the computational domain $R = 5$ mm. We also include the electrostatic potential calculated by imposing homogeneous Neumann boundary conditions at the external boundary.

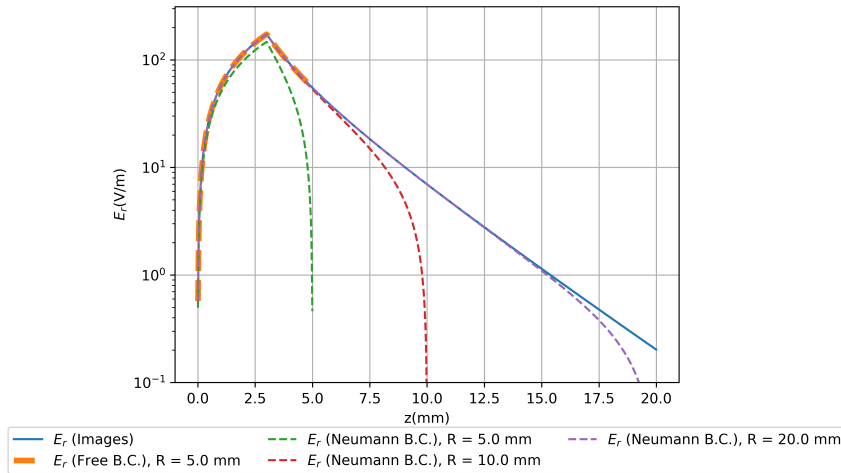


Figure 3.2: Comparison between electric fields created by an uniformly charged sphere between two planar infinite electrodes calculated by the approach presented in this work, by the method of images and by imposing homogeneous Neumann boundary conditions at the external boundary of the computational domain. Note the overlap between the lines corresponding to free boundary conditions and to the method of images.

We see that the field calculated with the approach presented here is indistinguishable from the field from the method of images. The homogeneous Neumann conditions, on the other hand, produce an electric field that at the surface of the sphere deviates by about 15% from the other two in the worst case, i.e. with $R = 5$ mm. To investigate the convergence of the homogeneous Neumann solution we extended the computational domain by computing the field also for $R = 10$ mm and $R = 20$ mm. As we move the external boundary away, the solution with Neumann conditions approaches our reference solution (Method of Images). The Neumann condition forces a stronger screening of the electric field as the external boundary moves closer to the charged sphere. As we will see, applied to streamer simulations, this leads to slightly lower values of the electric field in the streamer head and therefore less ionization.

3.2.6.2 Order of accuracy

We have checked that the method described above does not change the order of accuracy of the discretization of the Poisson equation by constructing a closed-form solution of the

3. A DOMAIN-DECOMPOSITION METHOD TO IMPLEMENT ELECTROSTATIC FREE BOUNDARY CONDITIONS FOR ELECTRIC DISCHARGES

Poisson equation that satisfies homogeneous Dirichlet boundary conditions in the upper and lower electrodes. We have used the potential

$$\phi = \sin\left(\pi \frac{z}{L}\right) e^{-\frac{r^2}{\sigma^2} - \frac{(z-z_0)^2}{\sigma^2}}, \quad (3.20)$$

whose Laplacian has the form

$$\Delta\phi = \frac{1}{L^2\sigma^4} \left\{ 4L\pi\sigma^2 (z - z_0) \cos\left(\pi \frac{z}{L}\right) + \left[\pi^2\sigma^4 + L^2(-4r^2 + 6\sigma^2 - 4(z - z_0)^2) \right] \right\} \times \sin\left(\pi \frac{z}{L}\right) e^{-\frac{r^2}{\sigma^2} - \frac{(z-z_0)^2}{\sigma^2}}. \quad (3.21)$$

Although this charge density is not strictly bounded, the contribution of charges excluded from the domain decays super-exponentially as the domain becomes wider and can thus be neglected as long as the external radius of the computational domain is significantly longer than σ .

We have solved the Poisson equation corresponding to the Laplacian (3.21) with $L = 1$ m, $\sigma = 0.1$ m and $z_0 = 0.5$ m within a cylindrical domain with a radius $R = 0.5$ m, where we imposed free boundary conditions with the method described above. In this manner we checked that the convergence in the ℓ^2 -norm is of second order, the same as that of the finite difference scheme. This is as expected because $\tilde{\phi}_1$ and the Fourier coefficients (3.18) retain convergence of order $\mathcal{O}(h^2)$.

We are also interested in the convergence as we expand the outer boundary. Following the example of the previous section, this time we change the radius of the sphere to 0.1 mm and the mesh spacing to 1 μm . Errors are presented in Table 3.1. As we can see, ℓ^2 -norm and ℓ^1 -norm increases with increasing radius. Enlarging the domain and therefore adding more points to the computation just increases the error estimated with these two norms. On the other hand, the ℓ^∞ -norm reveals that the maximum difference between the exact solution and our approximation reduces as we extend the radius. We can have the outer radius as close as 0.15 mm without a significant increase in error.

$r_{max}(\text{mm})$	$\ \varepsilon\ _2$	$\frac{\ \varepsilon\ _2}{\ \phi\ _2}$	$\ \varepsilon\ _1$	$\frac{\ \varepsilon\ _1}{\ \phi\ _1}$	$\ \varepsilon\ _\infty$	$\frac{\ \varepsilon\ _\infty}{\ \phi\ _\infty}$
0.15	5.164×10^{-5}	4.582×10^{-4}	1.947×10^{-2}	6.194×10^{-4}	2.897×10^{-7}	3.525×10^{-4}
0.3	6.960×10^{-5}	5.710×10^{-4}	3.756×10^{-2}	8.127×10^{-4}	2.879×10^{-7}	3.504×10^{-4}
0.6	9.593×10^{-5}	7.702×10^{-4}	7.372×10^{-2}	1.273×10^{-3}	2.877×10^{-7}	3.501×10^{-4}

Table 3.1: Error obtained with change in outer radius

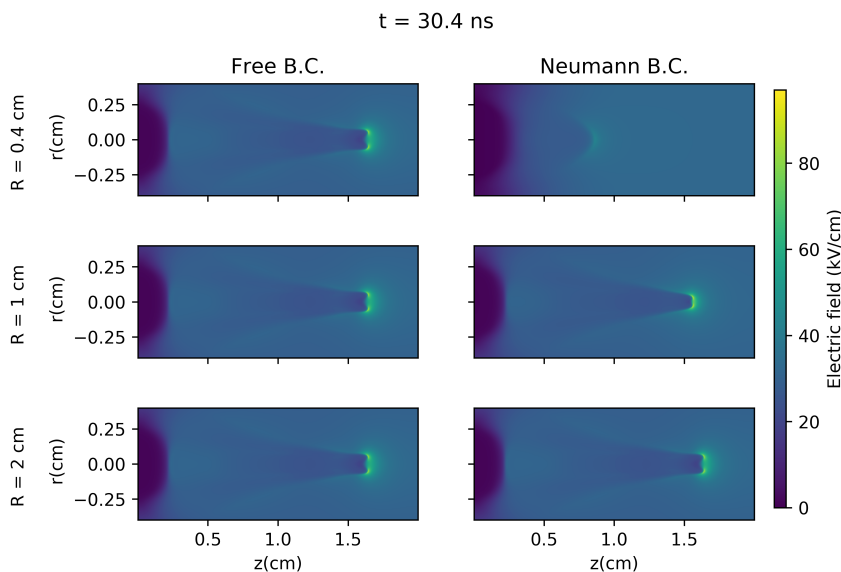


Figure 3.3: Streamer simulations using free boundary conditions (left column) and homogeneous Neumann boundary conditions (right column) in the external boundary of the computational domain. For each selection of the boundary conditions we show three simulations where the computational domain extends to a radius $R = 0.5$ cm (top), $R = 1$ cm (middle) and $R = 2$ cm (bottom).

3.2.7 Streamer simulations

In elongated electric discharges, Neumann boundary conditions are often considered more appropriate than Dirichlet to be applied at r_{max} because there is not a physical electrode in the radial direction, and therefore there is no reason to keep constant the potential there. The development of electric discharges is driven by long range interactions and therefore boundary conditions certainly affect the solution inside the computational domain. These effects can be reduced by enlarging the domain in the radial direction at the expense of a higher computational cost. The procedure we have described allows us to keep the boundary r_{max} close to the core of the simulation without noticeable numerical effects on the electric discharge. The following simulations clearly illustrate the features mentioned.

We simulated the propagation of streamer discharges between two planar electrodes with our in-house electro-hydrodynamic code described in chapter 2. The chemical model includes impact ionization and dissociative attachment. The Poisson equation is solved

3. A DOMAIN-DECOMPOSITION METHOD TO IMPLEMENT ELECTROSTATIC FREE BOUNDARY CONDITIONS FOR ELECTRIC DISCHARGES

using the Improved Stabilized version of BiConjugate Gradient solver from the PETSc numerical library *Balay et al.* (2016b,a).

We selected an inter-electrode gap of $L = 2$ cm and a background electric field of 27 kV/cm. The streamer is initiated by a neutral gaussian seed attached to the electrode at $z = 0$, on the central axis. The peak electron density in this seed is 10^{14} cm⁻³ and the e -folding length is 0.7 mm.

As we are interested in the effect of the external boundary conditions, we run simulations both with free boundary conditions, implemented as described above, and with homogeneous Neumann conditions for the electrostatic potential (as mentioned above, it is generally assumed that Neumann boundary conditions introduce slightly smaller artifacts). We also use different radii of the computational domain, $R = 0.5$ cm, $R = 1$ cm and $R = 2$ cm. In figure 3.3 we show snapshots of the electric field resulting from these simulations at time $t = 30$ ns, shortly after the streamer branches in the simulations with free boundary conditions. Note however that the cylindrical symmetry of the simulations prevents proper branching.

In the plots we see that the simulations with free boundary conditions are essentially identical regardless of the lateral extension of the computational domain. The simulations with homogeneous Neumann conditions on the other hand depend artificially on the radius of the computational domain. The streamer barely develops with $R = 0.5$ cm and only the simulation with $R = 2$ cm reproduces accurately the branching time of the simulations with free boundary conditions. We conclude that, even in this case where the aspect ratio of the discharge is not extremely high, the computational gain from reducing the domain size (roughly a factor 4) more than compensates for the cost of solving twice the Poisson equation, resulting in an overall improvement of about a factor 2.

3.3 Full free boundary conditions

Throughout this chapter we have described a method to implement free boundary conditions in the outer boundary of a discharge confined between two parallel plates. This method can also be extended to implement free boundary conditions in all boundaries of a simulation with cylindrical symmetry. In this section we describe this extension.

3.3.1 Domain decomposition

In section 3.2 we solved the Poisson equation in the space between two infinite, parallel planes. We can build the solution in free space upon this procedure. First, we decompose the full-space domain Ω into three disjoint subdomains, which we name Ω_0 , Ω_1 and Ω_2 (see figure 3.4). We assume now that the support of the charge distribution f is contained in Ω_0 and thus arrive at the three coupled problems

$$\begin{aligned} \Delta\phi_0 &= f & \text{in } & \Omega_0, \\ \phi_0 &= \phi_{\Gamma_{0i}} & \text{on } & \partial\Gamma_{0i}, i = 1, 2, \end{aligned} \quad (3.22a)$$

and

$$\begin{aligned} \Delta\phi_i &= f & \text{in } & \Omega_i, \\ \phi_i &= \phi_{\Gamma_{0i}} & \text{on } & \partial\Gamma_{0i}, \end{aligned} \quad (3.22b)$$

where $i = 1, 2$ and $\Gamma_{0i} = \partial\Omega_0 \cap \partial\Omega_i$ are the surfaces $z = 0$ and $z = L$ respectively.

Since there are two interfaces, the normal derivative is subject to two conditions:

$$\frac{\partial\phi_0}{\partial z} = \frac{\partial\phi_i}{\partial z} \text{ on } \Gamma_i, i = 1, 2. \quad (3.23)$$

3.3.2 Linearity

As we did before, due to the linearity of the equations, we can split the problem into

$$\begin{aligned} \Delta\bar{\phi}_0 &= 0 & \text{in } & \Omega_0, \\ \bar{\phi}_0 &= \phi_{\Gamma_{0i}} & \text{on } & \partial\Gamma_{0i}, i = 1, 2, \end{aligned} \quad (3.24a)$$

$$\begin{aligned} \Delta\tilde{\phi}_0 &= f & \text{in } & \Omega_0, \\ \tilde{\phi}_0 &= 0 & \text{on } & \partial\Gamma_{0i}, i = 1, 2 \end{aligned} \quad (3.24b)$$

3. A DOMAIN-DECOMPOSITION METHOD TO IMPLEMENT ELECTROSTATIC FREE BOUNDARY CONDITIONS FOR ELECTRIC DISCHARGES

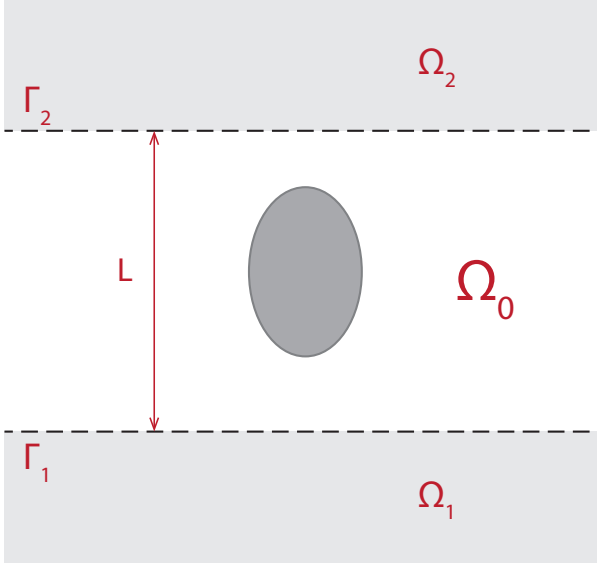


Figure 3.4: Geometry of the problem. Ω is divided into three subdomains: Ω_0 , Ω_1 and Ω_2 . The three extend indefinitely outwards and the latter two also downwards and upwards respectively.

and for $i = 1, 2$,

$$\begin{aligned} \Delta \bar{\phi}_i &= 0 & \text{in } \Omega_i, \\ \bar{\phi}_i &= \phi_{\Gamma_{0i}} & \text{on } \partial\Gamma_{0i}, \end{aligned} \quad (3.25a)$$

$$\begin{aligned} \Delta \tilde{\phi}_i &= f & \text{in } \Omega_i, \\ \tilde{\phi}_i &= 0 & \text{on } \partial\Gamma_{0i}. \end{aligned} \quad (3.25b)$$

Since there is no charge outside the computational domain, $\tilde{\phi}_i = 0$ for $i = 1, 2$. These equations naturally fulfill the condition that the potential vanishes at $-z, z, \rho \rightarrow \infty$.

Note now that the problem (3.24b) can be solved by the procedure described in section 3.2, since $\tilde{\phi}_0$ is the union of the solutions to the problems at (3.4).

In terms of these components, the flux equation (3.5) can be expressed as

$$\frac{\partial \bar{\phi}_0}{\partial z} [\phi_{\Gamma_{0i}}] - \frac{\partial \bar{\phi}_i}{\partial z} [\phi_{\Gamma_{0i}}] = -\frac{\partial \tilde{\phi}_0}{\partial z} [f] \text{ on } \Gamma, \forall i. \quad (3.26)$$

3.3.3 Expansion in solutions of the Laplace equation

The potentials $\bar{\phi}_i$ in (3.25a) are solutions of the Laplace equation in cylindrical coordinates and they can be expanded using a set of solutions (see e.g. *Jackson (1975)*). Since the domain is unbounded in the radial direction, instead of a series expansion we obtain an integral transform, which we can write in terms of the zero-order Hankel transform as:

$$\bar{\phi}_0 = \int_0^\infty k dk [A(k) e^{kz} + B(k) e^{-kz}] J_0(k\rho), \quad (3.27a)$$

$$\bar{\phi}_1 = \int_0^\infty k dk C(k) e^{kz} J_0(k\rho), \quad (3.27b)$$

$$\bar{\phi}_2 = \int_0^\infty k dk D(k) e^{-kz} J_0(k\rho), \quad (3.27c)$$

where $J_0(x)$ is the zero-order Bessel function of the first kind and the functions A, B, C, D weight the independent solutions to the Laplace equation. Note that, although the factor k can be absorbed into these functions, it appears explicitly in order to show the Hankel transform structure.

The function $\phi_{\Gamma_{0i}}$ can also be written as:

$$\phi_{\Gamma_{0i}}(\rho) = \int_0^\infty k dk E_i(k) J_0(k\rho). \quad (3.28)$$

Casting these equations in the form of a Hankel transform is important because as the Hankel transform can be inverted (it is its own inverse) we can use the fact that, subject to some regularity assumptions,

$$\int_0^\infty k dk F(k) J_0(k\rho) = 0 \iff F(k) = 0. \quad (3.29)$$

3.3.4 Continuity of the normal derivative

Imposing that $\bar{\phi}_0 = \bar{\phi}_i = \phi_{\Gamma_{0i}}$ at $z = 0$ and L , we solve for A, B, C, D using (3.29) and write (3.27) as

$$\bar{\phi}_0 = \int_0^\infty \frac{k dk}{e^{2kL} - 1} \left[(E_2 e^{kL} - E_1) e^{kz} + (-E_2 + E_1 e^{kL}) e^{-k(z-L)} \right] J_0(k\rho), \quad (3.30a)$$

3. A DOMAIN-DECOMPOSITION METHOD TO IMPLEMENT ELECTROSTATIC FREE BOUNDARY CONDITIONS FOR ELECTRIC DISCHARGES

$$\bar{\phi}_1 = \int_0^\infty k \, dk \, E_1 e^{kz} J_0(k\rho), \quad (3.30b)$$

$$\bar{\phi}_2 = \int_0^\infty k \, dk \, E_2 e^{-k(z-L)} J_0(k\rho). \quad (3.30c)$$

Using these expressions into the equation for the normal derivative (3.26) we obtain

$$\int_0^\infty \frac{2e^{kL}k^2 \, dk}{e^{2kL} - 1} (E_2 - E_1 e^{kL}) J_0(k\rho) = - \left. \frac{\partial \tilde{\phi}_0}{\partial z} \right|_{z=0}, \quad (3.31a)$$

$$\int_0^\infty \frac{e^{kL}k^2 \, dk}{e^{2kL} - 1} (E_2 e^{kL} - E_1) J_0(k\rho) = - \left. \frac{\partial \tilde{\phi}_0}{\partial z} \right|_{z=L}. \quad (3.31b)$$

The Bessel functions fulfil the closure relation and in particular the zero-order Bessel function

$$\int_0^\infty r J_0(kr) J_0(k'r) \, dr = \frac{1}{k} \delta(k - k'), \quad (3.32)$$

where $\delta(k - k')$ represents the Dirac delta function.

We can obtain the coefficients E_1 and E_2 going back to the k -space by means of the Hankel transform and using the closure relation (3.32):

$$E_1(k) = \frac{1}{2} (e^{-kL} I_L - I_0), \quad (3.33a)$$

$$E_2(k) = \frac{1}{2} (I_L - e^{-kL} I_0), \quad (3.33b)$$

where

$$I_{0,L}(k) = -\frac{1}{k} \int_0^\infty \rho \, d\rho \left. \frac{\partial \tilde{\phi}_0}{\partial z} \right|_{z=0,L} J_0(k\rho). \quad (3.34)$$

In this expression $\tilde{\phi}_0$ and its normal derivative are known from the algorithm described in 3.2.5. Therefore we can compute $I_{0,L}$ and, using (3.33) $E_{1,2}$. These functions in turn can be inserted in (3.28) to yield the boundary condition to impose on $\Gamma_{1,2}$.

So far we have got $\phi_{\Gamma_{1,2}}$, however, we need to calculate again the boundary conditions at $r = R$ using equation 3.30a.

3.3.5 Algorithm

We are now ready to detail the domain-decomposition algorithm that allows us to solve the Poisson equation in the reduced computational domain Ω_0 with free boundary conditions in the radial direction and at the top and bottom boundaries of the computational domain:

1. Compute $\tilde{\phi}_0$ by following the algorithm in section 3.2.5.
2. Calculate the normal derivative of $\tilde{\phi}_0$ at $z = 0, L$. Apply a Hankel transform and use expressions 3.33 to obtain the coefficients E_1 and E_2 .
3. Use these coefficients to obtain the boundary values $\phi_{\Gamma_{1,2}}$ by using a second Hankel transform (3.30b, 3.30c).
4. Update boundary values at $r = R$ with an additional Hankel transform (3.24a)
5. Solve the Poisson equation in Ω_0 with the boundary conditions computed in the previous steps.

3.3.6 Tests and sample implementation

3.3.6.1 Tests

In order to test our scheme we consider now a simple setup where the Poisson equation has a closed-form solution. An example of such a configuration is an uniformly charged sphere located in free space (see e.g. (*Jackson, 1975*)).

Suppose a sphere centered at $(\rho, z) = (0, z_0)$ with radius $a < R$ and total charge Q . At a point with cylindrical coordinates (ρ, z) the potential reads

$$\phi(\rho, z) = \frac{Q}{4\pi\epsilon_0} \begin{cases} \frac{1}{[\rho^2 + (z - z_0)^2]^{1/2}} & \text{if } \rho^2 + (z - z_0)^2 > a^2, \\ \frac{3a^2 - \rho^2 - (z - z_0)^2}{2a^3} & \text{if } \rho^2 + (z - z_0)^2 \leq a^2. \end{cases} \quad (3.35)$$

Figure 3.2 shows a comparison between the potential along the z -axis computed using expression 3.35 and the approaches described in section 3.2 and Section 3.3. Here we took $a = 3$ mm, $R = 5$ mm, $Q = 10^{13}$ e (e is the elementary charge), $z_0 = 5$ mm. For the discretized solution we used $\Delta r = \Delta z = 25 \times 10^{-3}$ mm and a longitudinal extension of the computational domain $\Delta L = 10$ mm.

3. A DOMAIN-DECOMPOSITION METHOD TO IMPLEMENT ELECTROSTATIC FREE BOUNDARY CONDITIONS FOR ELECTRIC DISCHARGES

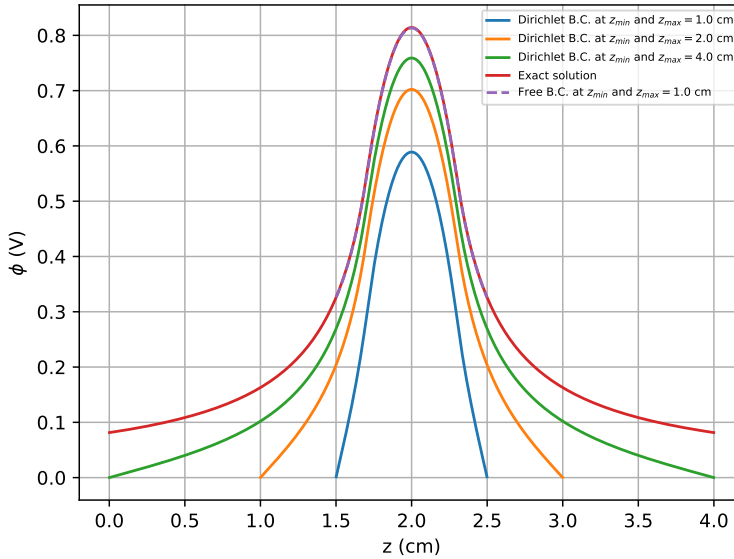


Figure 3.5: Comparison between the electrostatic potential along the z -axis created by a uniformly charged sphere in free space using the approach described in section 3.3, the potential 3.35 and solving Poisson’s equation with Dirichlet boundary conditions in three domains of increasing length. Note the overlap between the lines corresponding to free boundary conditions and the reference solution 3.35.

The potential calculated with the approach presented in this section is indistinguishable from the analytic solution (3.35). Dirichlet boundary conditions at the two ends, on the other hand, produce a potential that deviates nearly 25% from the analytic solution at the center of the sphere. To investigate the convergence of the homogeneous Dirichlet solution we extended the computational domain and computed the potential for $L = 20$ mm and $L = 40$ mm. As we move z_{min} and z_{max} away from the center of the charged sphere, the solution with Dirichlet conditions approaches our reference solution (3.35). As the charged sphere gets closer to the electrodes, the electric potential shows a more prominent drop to fulfill the condition $\phi(z = 0, L) = 0$. In streamer simulations this causes slightly higher values of the electric field at the streamer head as we will see in the next section.

3.3.6.2 Order of accuracy

We have checked that the method described above does not change the order of accuracy of the discretization of the Poisson equation by constructing a closed-form solution of the Poisson equation that decays at infinity. We have used the potential

$$\phi = e^{-\frac{r^2}{\sigma^2} - \frac{(z-z_0)^2}{\sigma^2}}, \quad (3.36)$$

whose Laplacian has the form

$$\Delta\phi = \frac{1}{\sigma^4} \left[4r^2 - 6\sigma^2 + 4(z-z_0)^2 \right] \times e^{-\frac{r^2}{\sigma^2} - \frac{(z-z_0)^2}{\sigma^2}}. \quad (3.37)$$

Although this charge density is not strictly bounded, the contribution of charges excluded from the domain decays super-exponentially as the domain becomes larger and can thus be neglected as long as $z_{max} - z_0$ and $z_{min} - z_0$ are sufficiently larger than σ .

We have solved the Poisson equation corresponding to the Laplacian (3.37) with $L = 1$ m, $\sigma = 0.1$ m and $z_0 = 0.5$ m within a cylindrical domain with a radius $R = 0.5$ m. We have imposed free boundary conditions at every boundary of the domain. In this manner we checked that the convergence in the ℓ^2 -norm is of second order, the same as that of the finite difference scheme.

We are also interested in the convergence as we move the boundaries z_{min} and z_{max} away from the charged sphere. Following the example in subsection 3.3.6.1, this time we change the radius of the sphere to 0.1 mm, $R = 10$ mm and the mesh spacing to $10 \mu\text{m}$. Errors are presented in Table 3.2.

$\Delta L(\text{mm})$	$\ \varepsilon\ _2$	$\frac{\ \varepsilon\ _2}{\ \phi\ _2}$	$\ \varepsilon\ _1$	$\frac{\ \varepsilon\ _1}{\ \phi\ _1}$	$\ \varepsilon\ _\infty$	$\frac{\ \varepsilon\ _\infty}{\ \phi\ _\infty}$
0.3	2.539×10^{-3}	1.773×10^{-2}	1.385	2.393×10^{-2}	5.504×10^{-6}	5.586×10^{-3}
0.6	1.811×10^{-3}	1.095×10^{-2}	1.401	1.429×10^{-2}	2.491×10^{-6}	2.753×10^{-3}
1.2	1.265×10^{-3}	6.941×10^{-3}	1.385	8.965×10^{-3}	1.216×10^{-6}	1.344×10^{-3}

Table 3.2: Errors obtained with changes in the longitude of the domain

3.3.7 Streamer simulations

As we did before for the case of free boundary conditions in the radial direction, in this subsection, we present the results of several negative streamer simulations where we apply

3. A DOMAIN-DECOMPOSITION METHOD TO IMPLEMENT ELECTROSTATIC FREE BOUNDARY CONDITIONS FOR ELECTRIC DISCHARGES

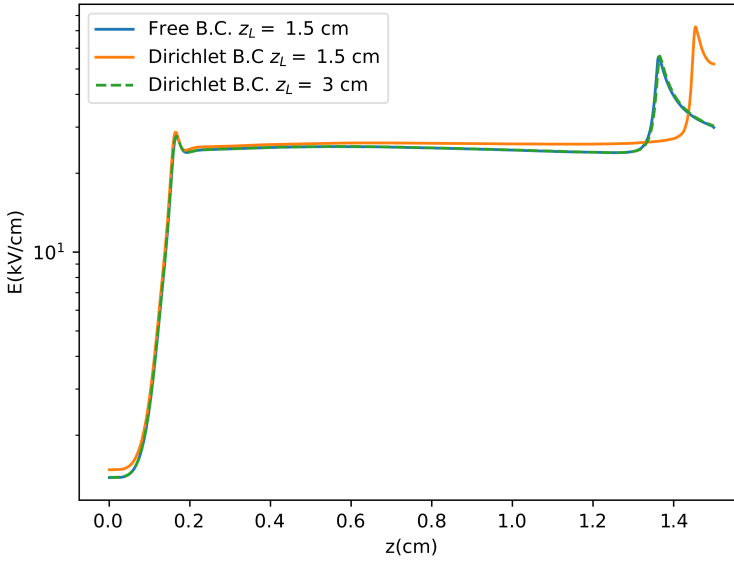


Figure 3.6: Comparison of the module of the electric field along the z -axis for a streamer simulation with Dirichlet boundary conditions at $z = 0$ (solid blue line), Dirichlet boundary conditions at both ends with domain lengths 1.5 cm (solid orange line) and 3.5 cm (dashed green line). As the streamer approaches the electrode at $z_L = 1.5$ cm (solid orange line), the electric field at the streamer head increases since the electrostatic potential drop occurs in a shorter distance.

electrostatic free boundary conditions at $r = R$ and $z = z_L$. The solution to this problem is obtained by simply considering the boundary values calculated at Γ_L and setting $I_0 = 0$ in equation 3.33b. As for the extent of the domain, $R = 0.4$ cm and we vary z_L in the three streamer simulations: two of the streamers simulations with Dirichlet boundary conditions at both ends $z_L = 1.5, 3$ cm and one streamer simulation with free boundary conditions at $z_L = 1.5$ cm.

Initial conditions are the same as in subsection 3.2.7, except for the background electric field that we set to 25 kV/cm here.

Figure 3.6 shows the results of the three simulations for the module of the electric field along the z -axis at $t = 40$ ns. The dashed line represents the reference solution ($z_L = 3$ cm) since the electrode is far enough from the streamer head. As we can see, the solution

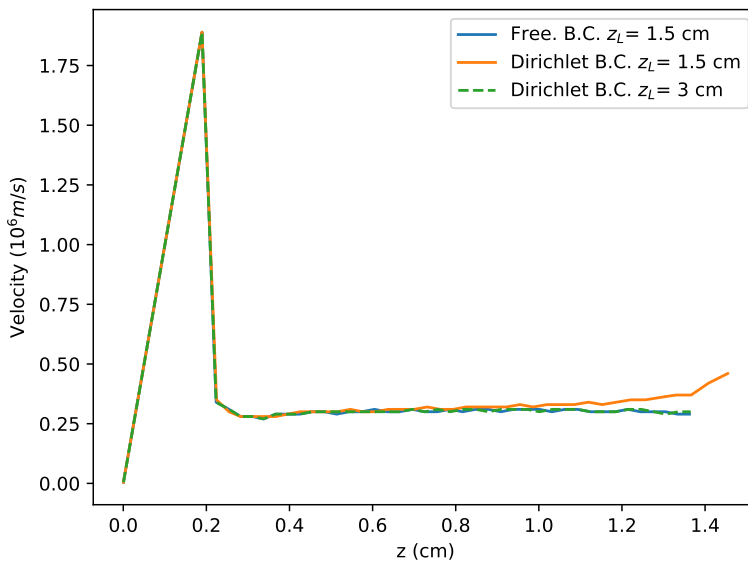


Figure 3.7: Comparison of streamer velocity for a streamer simulation with Dirichlet boundary conditions at $z = 0$ (solid blue line), Dirichlet boundary conditions at both ends with domain lengths 1.5 cm (solid orange line) and 3.5 cm (dashed green line). As the streamer approaches the electrode at $z_L = 1.5$ cm (solid orange line) the streamer head accelerates. This is not observed in the two other simulations where the streamer head keeps a constant velocity.

3. A DOMAIN-DECOMPOSITION METHOD TO IMPLEMENT ELECTROSTATIC FREE BOUNDARY CONDITIONS FOR ELECTRIC DISCHARGES

with free boundary conditions at $z_L = 1.5$ cm approximates the reference solution fairly well. On the other hand and as expected, the solution with Dirichlet boundary conditions at $z_L = 1.5$ cm deviates from the reference solution. The electric field in the streamer body/head is slightly overestimated, specially as the streamer approaches the electrode at $z = z_L$.

As a result of this, the propagation velocity of the the streamer head is different (fig. 3.7) and for the case of Dirichlet B.C. at $z_L = 1.5$ cm, the streamer head accelerates while for the other two cases, the streamer head keeps a constant velocity.

3.4 Discussion and conclusions

Most electric discharges develop as elongated channels. Despite different physical conditions and ionization mechanisms this feature is common to streamers, leaders and arcs. The underlying reason for this shared property is that all these processes are affected by a Laplacian instability *Arrayás et al. (2002); Derks et al. (2008)*, whereby small bumps in a discharge front enhance the electric field ahead and thus grow faster than the surrounding regions. This prevents the formation of wide, smooth discharges and creates branched discharge trees of many filaments *Luque and Ebert (2014)*.

Since this is the preferred shape of a discharge, it is reasonable to optimize our numerical models for elongated channels, selecting high-aspect-ratio computational domains. The method that we have presented here can be used to achieve this efficiently and without losing accuracy.

We have presented a first extension of this method, where we also set free boundary conditions at the upper and lower simulation boundaries. This can be useful for the investigation of discharges not attached to any electrode or, with appropriate modifications, attached to a single electrode. This extension can be computationally more expensive if Hankel transforms are not properly treated.

A second extension is to adapt the method to run in parallel in several processors. If we parallelize the Poisson solver by decomposing the domain, the application of the method described above requires collecting information about the initial solution around the external boundary and then performing a one-dimensional Fourier transform. The

overhead of these steps is small compared to the operations required for the solution of the Poisson equation so the method can be efficiently parallelized. This method has been integrated in our code and successfully runs in parallel (MPI framework) upon thousands of computing nodes.

Finally, one may ask about the suitability of this method for non-uniform meshes and, in particular, for adaptively refined meshes. Although the application of the method is in principle straightforward, a careful analysis is required to understand the error incurred due to a possibly coarser resolution around the boundary than around a localized charge density. This analysis, however, falls out of the scope of the present chapter.

Note that although we have focused on the solution of the Poisson equation, this method can be easily generalized to other elliptic partial differential equations. This can then be applied to other components of streamer simulation codes such as the speeding-up of photoionization calculations by approximating the interaction integral by combining solutions of a set of partial differential equations, as proposed in references *Ségur et al. (2006)*; *Luque et al. (2007)*; *Bourdon et al. (2007)*. Our code includes the computation of the photoionization term (see eq. 2.2) using this method.

3. A DOMAIN-DECOMPOSITION METHOD TO IMPLEMENT ELECTROSTATIC FREE BOUNDARY CONDITIONS FOR ELECTRIC DISCHARGES

Chapter 4

Spontaneous emergence of space stems ahead of negative leaders in lightning and long sparks

4.1 Introduction

One of the outstanding mysteries in atmospheric electricity concerns the progression of negative lightning leaders. Being hot and ionized channels, leaders are initiated in a thundercloud and expand bipolarly, with their positive and negative extremes advancing in more or less opposite directions. For some elusive reason, negative leaders advance in a stepped fashion, with waiting times of tens of microseconds punctuated by sudden jumps of microsecond time scale (*Dwyer and Uman, 2014*). This behavior is observed not only in lightning leaders but also in negative laboratory discharges longer than about two meters.

Besides being a fundamental but mysterious process in electric discharges, leader steps are relevant because they produce the Very High Frequency (VHF) radio pulses that reveal the development of lightning flashes in Lightning Mapping Arrays (*Thomas et al., 2001*). Leader steps are also correlated with X-ray emissions detected around a lightning discharge (*Dwyer et al., 2005*) and therefore they are possibly linked to Terrestrial Gamma-ray Flashes (TGFs) detected by satellites orbiting hundreds of kilometers above ground (*Fishman et al., 1994; Smith et al., 2005; Marisaldi et al., 2010; Briggs et al.,*

4. SPONTANEOUS EMERGENCE OF SPACE STEMS AHEAD OF NEGATIVE LEADERS IN LIGHTNING AND LONG SPARKS

2013).

The first observation of leader stepping can be traced back to the pioneering work of *Schonland et al.* (1935) in the 1930s, who coined the term “stepped leader” for the intermittent advance of downward negative lightning channels recorded in their streak camera. In the decades after Schonland’s work, advances in this topic arose mostly from laboratory experiments with meter-long spark discharges. The work of, among others, *Gorin et al.* (1976) and the *Les Renardières group* (1978a) revealed the dynamics of a negative leader step: the leader tip is preceded by a filamentary corona containing a bright nucleus termed “space stem”. After some microseconds the space stem evolves into a “space leader” that propagates in both directions and whose extremes are surrounded by additional coronas of both polarities. The leader completes one step when the space leader bridges the gap to the main leader channel.

Recordings with the high-framerate video cameras fielded in the last decade show that lightning leaders, although they involve slightly different space- and time-scales, follow the same pattern as long laboratory sparks. With integration times of a few microseconds, the observations of *Hill et al.* (2011) for natural stepped leaders and *Biagi et al.* (2014) and *Gamerota et al.* (2014) for leaders in triggered lightning captured images of the space stem ahead of the leader tip, embedded in a filamentary corona.

Despite these observational advances, our understanding about the physics of stepped leaders is still very incomplete. Measured optical spectra indicate that the leader temperature reaches around 5000 K (*Cooray*, 2003) and even 30 000 K (*Kieu et al.*, 2020) for laboratory discharges and up to 30 000 K in lightning leaders (*Orville*, 1968), which, in both cases and according to chemical models, suffices to sustain a high ionization (*Gallimberti*, 1979). On the other hand the filaments in the corona, called streamers, are not much above ambient temperature; their ionization, lower than that of leaders, is created mostly at their tips, where they enhance the electric field strongly enough to accelerate electrons up to the threshold of impact ionization (*Ebert et al.*, 2010). Models for the streamer-to-leader transition (*Popov*, 2003; *da Silva and Pasko*, 2013) successfully reproduce the transition time scale of around 1 μ s for atmospheric pressure but depend on manually imposing a total electric current that in reality is an outcome of the discharge physics. They also neglect the longitudinal inhomogeneity of the discharge and therefore they sideline leader

stepping and the formation of space stems. The physical mechanism governing the latter remains a mystery (see e.g. (*Biagi et al.*, 2010; and Raizer, 2010)); a recent review (*Dwyer and Uman*, 2014) included this problem in the top ten questions in lightning research.

In this chapter, we show that space stems originate from an attachment instability inside streamer channels. Since space stems are the key to leader stepping, our results open the door to the full understanding of this mechanism as well as its associated radio and energetic particle emissions. Originally investigated in the 1970s (*Douglas-Hamilton and Mani*, 1974; *Sigmond*, 1984), the attachment instability is triggered by regions of lower conductance per unit length (i.e. conductivity integrated over a cross-section) inside a corona, which we show arise spontaneously when a negative streamer emerges from a leader. One major and slightly counter-intuitive aspect of our work is that bright regions inside a corona reveal regions of lower, not higher, electron density. Although this is in complete correspondence with a regular electric circuit where energy is mostly dissipated in high-resistivity components, this insight has escaped previous interpretations of the space stem. At high-altitude, in leader-less discharges (sprites), the attachment instability forms standing patterns called beads and glows (*Luque et al.*, 2016b; *Luque and Ebert*, 2010; *Liu*, 2010).

4.2 Space stem

4.2.1 Model and Initial Conditions

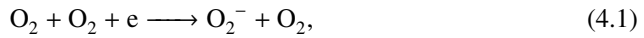
Since lightning leaders and long laboratory sparks share the same mechanism of propagation, to simplify our computations we choose to focus here on the propagation of a leader under laboratory conditions. Typical laboratory leaders span from tens of centimeters to around one meter and are surrounded by streamer coronas with roughly the same extension (*Kostinskiy et al.*, 2018). These dimensions are too computationally demanding so, as we detail below, our simulated system is somewhat smaller.

We opt for simulating a single streamer that emerges from a leader tip; our assumption here is that the surrounding corona is not an essential component of the physics of space stems. We cannot rigorously justify this assumption but it is beared out by the similarity between observations and our results.

4. SPONTANEOUS EMERGENCE OF SPACE STEMS AHEAD OF NEGATIVE LEADERS IN LIGHTNING AND LONG SPARKS

We thus investigate the formation of space stems ahead of a negative leader channel with our 2D cylindrically symmetric model (z, r) for electric discharges that includes heating and expansion of the background gas fully self-consistently (see chapter 2).

The kinetic scheme employed in our simulations includes impact ionization, attachment/detachment, and water cluster formation/breaking. A detailed description of the scheme can be found in the supplementary material of *Luque et al. (2017)*. The only difference is that for the three-body attachment reaction



here we have used the rate from *Kossyi et al. (1992)*.

We emphasize the presence of water in the chemical model of our simulations. The relevance of water vapor for the evolution of streamer channels was previously discussed by *Gallimberti (1979)* and *Luque et al. (2017)*. By clustering around negative ions, even a small quantity of water molecules effectively suppresses electron detachment and thus strongly influences the evolution of the electron density on time scales of tens of nanoseconds.

Streamer discharges develop as thin and elongated channels which call for a narrow computational domain. To achieve this while suppressing the influence of the radial boundary conditions in the Poisson's equation we use the domain decomposition method described in chapter 3. Using this method, we solve Poisson's equation with Dirichlet boundary conditions at $z = 0$ and free boundary conditions elsewhere to prevent boundary effects as the streamer grows. By free boundary conditions we mean: 1) the potential tends to zero as the distance tends to infinity and 2) they are consistent with the charge inside the domain. The full domain size is $25 \text{ cm} \times 3 \text{ cm}$.

The term Q_T^{eff} in equation 2.1 couples the electrodynamics and bulk gas dynamics and accounts for dissipated power due to the electric current inside the corona. But note that this power is distributed unequally among the degrees of freedom of the underlying gas. Since the time scales involved in the streamer-to-leader transition are too short to reach thermodynamic equilibrium, the fraction of energy deposited into different degrees of freedom depends on the local conditions and, in particular, on the local electric field (*Flitti and Pancheshnyi, 2009; da Silva and Pasko, 2013*). A small fraction is directly

converted into translational energy of gas molecules and quickly thermalized. A larger amount excites electronic and ionization states; this is responsible for the process of *fast-heating* (Popov, 2001) and relaxes into thermal energy at time scales on the order of 100 ns. Another fraction of the energy is spent in dissociation of oxygen and nitrogen molecules and, finally, the remaining energy excites vibrational states and its time to thermalization is on the order of one second at ambient temperature and only significant compared with our relevant time scales once the temperature reaches about 10^4 K: this relaxation is neglected in the present study. Since, as we describe later, most heating is due to energies dissipated at or around the conventional breakdown electric field, roughly 30 kV/cm, we take the energy branching ratios corresponding to this field, where about half of the energy is frozen into vibrational excitations (see e.g. figure 1 in (Flitti and Pancheshnyi, 2009)). Furthermore, since the characteristic time of gas temperature increase is much longer than 100 ns, for the sake of simplicity, we consider fast-heating to be instantaneous. Then, we arrive at

$$Q_T^{eff} = \eta \mathbf{j} \cdot \mathbf{E}, \quad (4.2)$$

where $\eta \approx 0.5$, $\mathbf{j} = \sum_s q_s n_s \mathbf{v}_s$ and s run over all the species involved in our model.

Our initial condition consists in a short portion of leader with a small ionization patch slightly ahead of the tip that mimicks an irregularity of the leader head. Thus, the initial electron density is the sum of a uniform background n_e^{bg} plus

$$n_e^{\text{leader}} = n_{e0} \exp\left(-\frac{\max(z - z_L, 0)^2}{2\sigma_L^2} - \frac{r^2}{2\sigma_L^2}\right), \quad (4.3a)$$

and

$$n_e^{\text{seed}} = n_{e0} \exp\left(-\frac{(z - z_S)^2}{2\sigma_S^2} - \frac{r^2}{2\sigma_S^2}\right), \quad (4.3b)$$

where $z_L = 5$ cm is the location of the leader tip, the seed center is at $z_S = 6.1$ cm, the e -folding lengths are $\sigma_L = 3$ mm, $\sigma_S = 1.5$ mm and the electron density peaks at $n_{e0} = 10^{21} \text{ m}^{-3}$. The initial electron density is neutralized by an identical density of positive ions. Note that we selected these initial conditions after a few trials where we disregarded cases in which the streamer branches because these cannot be captured by our cylindrically symmetrical model. Besides, as mentioned above, to keep our computations feasible, the initial leader is somewhat shorter than experimental stepped leaders.

4. SPONTANEOUS EMERGENCE OF SPACE STEMS AHEAD OF NEGATIVE LEADERS IN LIGHTNING AND LONG SPARKS

We have run two different simulations: one with photo-ionization ($n_e^{\text{bg}} = 0$) following the method presented by *Luque et al. (2007)*, and another with a pre-conditioning of the gas surrounding the leader due to preceding coronas by adding a constant background ionization level $n_e^{\text{bg}} = 10^{15} \text{ m}^{-3}$. In both cases, we observed similar formation of a space stem but the simulation with photo-ionization exhibited an oscillation of the electric field at the streamer head that we attribute to a numerical artifact due to insufficient resolution for the smallest length scales involved in photo-ionization (*Zhelezniak et al., 1982; Wormeester et al., 2010*). Henceforth we limit ourselves to the simulation without photo-ionization. To check that this does not affect our key results we used another numerical code at our disposal (PESTO, described by *Luque (2017)*) that includes photoionization but does not account for gas heating or long-term chemistry. Using PESTO, we run simulations with a numerical resolution of $6 \mu\text{m}$ that produced results similar to those described below.

The embedding gas is a mixture of 79% N_2 and 21% O_2 . Initially, the gas pressure is 1 atm and the mechanical energy is zero. The ambient temperature is 300K and the temperature of the leader follows the same distribution as n_e^{leader} with a peak value of 2700K. Note that our model does not include high-temperature chemistry for the leader: in our simulation the role of leader is merely to provide the electrostatic environment for the streamer propagation. Finally, the simulation is driven by an external electric field pointing towards the leader with magnitude $E_0 = 10 \text{ kV/cm} + (20 \text{ kVcm}^{-1} \mu\text{s}^{-1})t$, where t is the simulation time.

With these conditions we simulated the inception and propagation of a streamer emerging from the leader tip. Our total simulation time was limited to about 100 ns at which point the streamer leaves the simulation domain. As we see below, this time is enough to see the formation of the space stem but too short to observe the full streamer-to-leader transition.

4.2.2 Results

Figure 4.1A summarizes our simulation. As the streamer emerges from the leader it goes through a narrowing phase where the conductance per unit length decreases. The charge transport through the streamer channel tends to homogenize the electric current flowing across the streamer channel, which implies a higher electric field in the narrow section. As sketched in figure 4.1B, where we plot the effective ionization rate of air, this enhanced

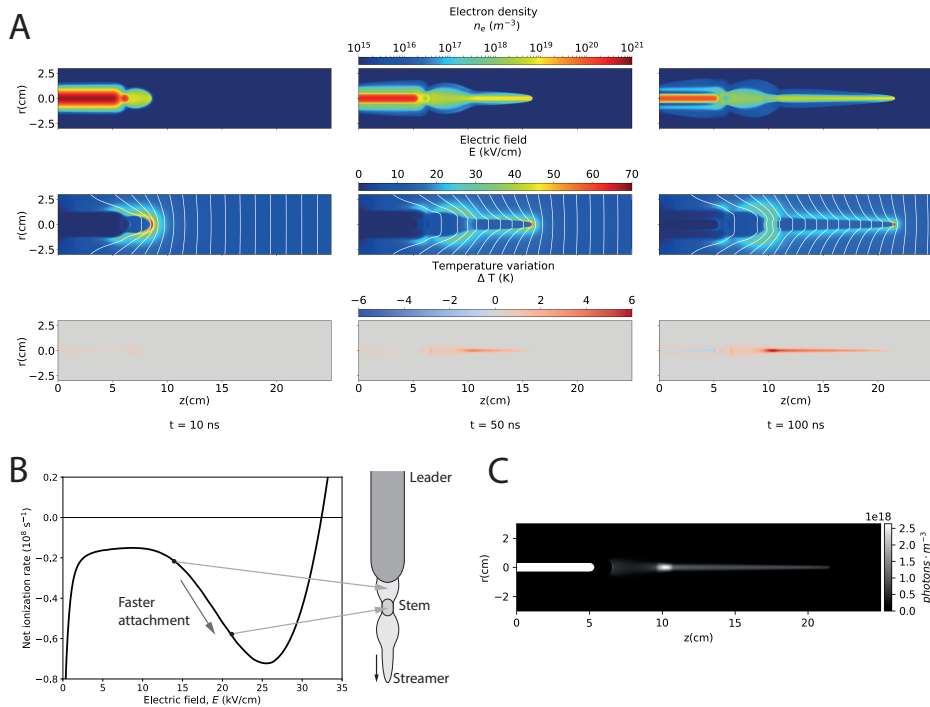


Figure 4.1: As a streamer propagates out of a leader tip it creates a segment of reduced conductivity that evolves into a space stem. Panel A summarizes the evolution of the streamer in terms of the electron density (top), electric field (middle), and temperature (bottom). The electric field row includes equipotential lines with constant spacing 12.5 kV, 13.5 kV and 14.5 kV (from left to right). The streamer leaves in its wake a segment of lower conductance per unit length that evolves into a space stem due to the attachment instability process sketched in panel B: a higher electric field accelerates the depletion of electrons, which in turns enhances the electric field. Finally, in panel C we show that our simulation reproduces the features of a space stem by plotting light emitted in the second positive system of the nitrogen molecule during the full simulation. We have masked (white region) leader emissions to focus on the space stem.

4. SPONTANEOUS EMERGENCE OF SPACE STEMS AHEAD OF NEGATIVE LEADERS IN LIGHTNING AND LONG SPARKS

field triggers an attachment instability (see chapter 1): the higher field increases the rate of dissociative electron attachment, decreasing further the conductance per unit length and increasing the field. This process enhances the electric field inside the narrow section of the channel until it saturates at an electric field where the net ionization curve slopes upward, between 25 and 30 kV/cm. A necessary condition for this process is that the electric field inside the streamer channel steps above the minimum of the effective attachment rate, around 10 kV/cm (see figure 4.1B). Hence, the emergence of space stems is favoured in streamers with high internal electric fields.

To check that the narrow segment with an enhanced electric field reproduces the observed features of a space stem, we computed the spatial distribution of light emissions. We included in our model the electron impact excitation of nitrogen molecules to the $N_2(B^3\Pi_g)$ and $N_2(C^3\Pi_u)$ electronic states, which are responsible respectively of the first and second positive systems of N_2 (see section A.1 in the Appendix for further details on the chemistry used to describe light emissions). We found that in our conditions the emissions of light are dominated by the second positive system and panel C of figure 4.1 shows these emissions integrated over the 100 ns of simulation. There we notice a bright spot embedded in a dim channel, clearly reminiscent of images in high-speed recordings of leader progression (*Hill et al.*, 2011; *Biagi et al.*, 2014; *Gamerota et al.*, 2014). Based on this resemblance we will henceforth use the name *stem* for this bright nucleus within the channel.

Let us now analyze the gas heating produced by the discharge. This is represented in the bottom row of panel A in figure 4.1, where we show the temperature variation relative to the initial conditions. The air in the stem heats up about 6 K in 100 ns. However, in our simulation the electron density decreases both in the stem and in the surrounding channel with a time scale close to 100 ns. This is consistent with previous models and experiments that investigated the effect of the repetition rate in streamer discharges (*Nijdam et al.*, 2014) and therefore it is unlikely that this electron depletion is due to shortcomings of our model. In our context it implies that the heating ratio diminishes: we do not expect a much higher temperature even if, by increasing our domain size, we extended our simulation time.

4.2.2.1 Formation of the Space Stem

Our key result is that the attachment instability is responsible for locally warmer regions ahead of a leader. A number of processes may reduce the channel conductance per unit length and trigger the instability, among them a jittering of the leader potential during the streamer propagation or pre-existing conductivity or gas-density perturbations along the streamer path (*Luque and Gordillo-Vázquez, 2011; Luque et al., 2016b*). Neither of these processes was included in our simulations and nevertheless the space stem formed spontaneously, which suggests that isolated stems are robust features of leader propagation.

In our simulation the stem results from a narrowing of the channel. Note that the narrowing of negative streamers ahead of a leader or a pointed electrode has been observed by *Kochkin et al. (2014)* and by *Kostinskiy et al. (2018)*. As we show in figure 4.2 the streamer head is initially wide because it is affected by the divergence of electric field lines emerging from the leader's curved tip. As this divergence decreases away from the leader tip, the streamer head shrinks. The narrowing of the streamer channel enhances more strongly the electric field at the tip, increasing the degree of ionization left in the streamer head's wake. The total conductance per unit length of the channel scales approximately as $R^2 n_e$, where R is the channel radius and n_e the electron density: initially the significant decrease of the radius dominates and the conductance per unit length diminishes; afterwards the increase of n_e due to a higher field at the tip overcomes the narrowing and the conductance per unit length increases again. The resulting minimum is the origin of the space stem as we show in the upper panel of 4.3. In the same figure (lower panel) and as we stated before, despite the noticeable variation of the conductance per unit length, the intensity is homogeneous across any section of the channel, including the space stem.

Let us now discuss the observed asymmetry between positive and negative leaders. Stepping is more prominent and readily observable in negative leaders but there are now clear observations (*Kostinskiy et al., 2018*) that under conditions of high relative humidity, positive leaders also experience stepped progression although space stems have never been observed in positive leaders. Our results provide a natural explanation for this asymmetry: the attachment instability is triggered by elevated electric fields inside a streamer channel and due to stronger ionization in positive streamers, these fields are higher in negative

4. SPONTANEOUS EMERGENCE OF SPACE STEMS AHEAD OF NEGATIVE LEADERS IN LIGHTNING AND LONG SPARKS

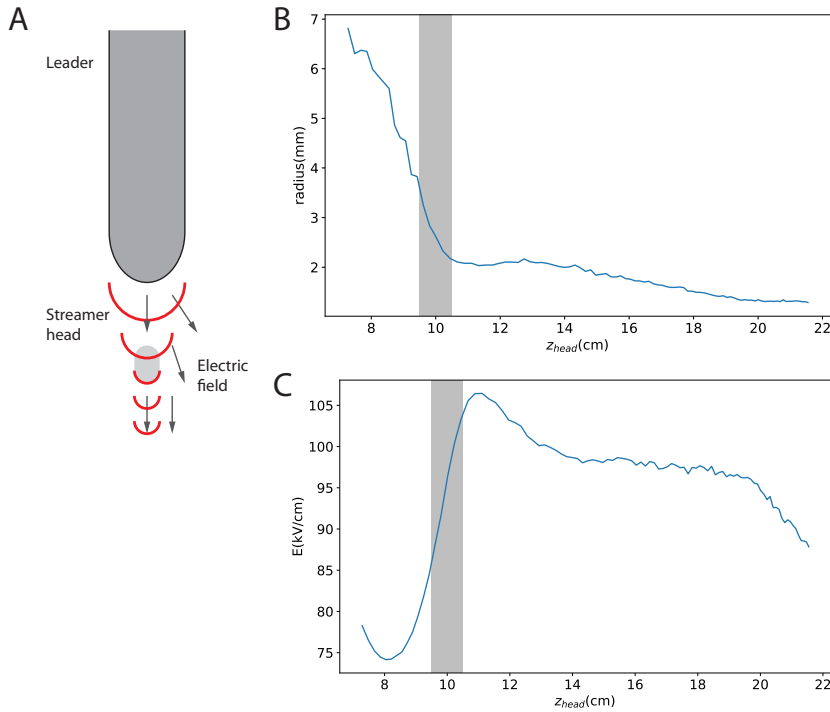


Figure 4.2: The space stem emerges due to the narrowing of the streamer channel. As sketched in panel A, when the streamer is still close to the leader tip it is widened by the diverging electric field lines around the curved leader tip; as it distances itself from the leader, the streamer is driven by a more homogeneous electric field and becomes narrower. This is shown in panel B, where we plot the streamer radius as a function of the streamer head position. The radius is defined here as the radius of curvature on the central axis of the surface defined by the maximum of the electric in the z direction around the head. The reduction of the radius leads to higher peak electric fields (panel C) and the resulting total channel conductance per unit length exhibits a minimum that afterwards evolves into the space stem as described in figure 4.1.

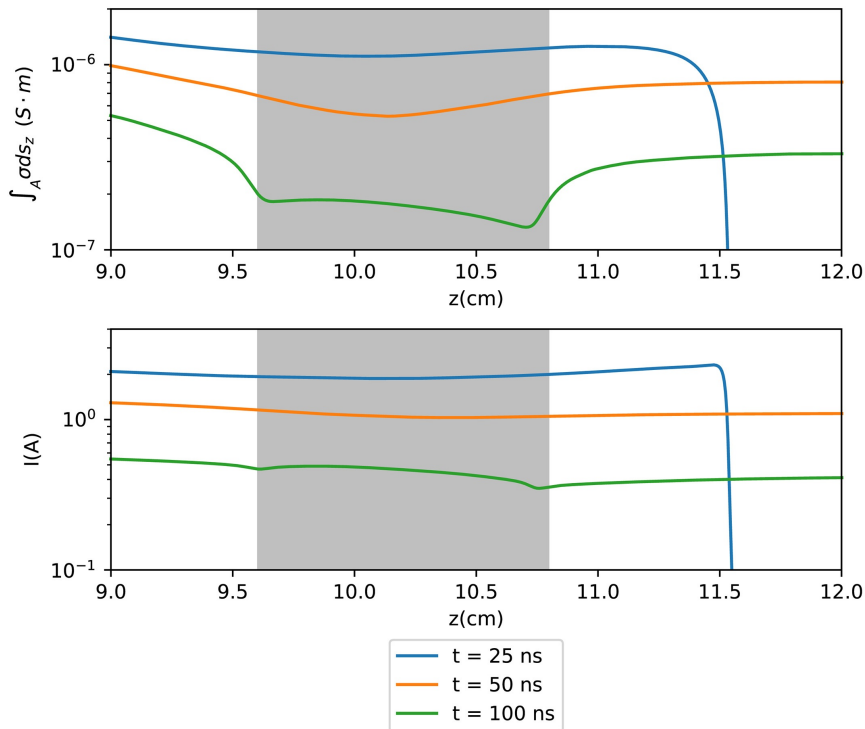


Figure 4.3: The upper panel shows the conductance per unit length around the space stem (grey area) at 25 ns, 50 ns and 100 ns. As the streamer propagates away from the leader tip (25 ns curve), the channel undergoes a narrowing until the conductance per unit length reaches a minimum (space stem). Right after, the channel starts to be able to compensate this narrowing with an increase of the electron density produced by a higher electric field and then the conductance per unit length rises. The two remaining curves show latter states of the conductance at the space stem, where the electron depletion is clear after attachment instability effects. The lower panel supports the idea that the low conductance in the space stem is countered by a high electric field to achieve an homogeneous intensity along the channel.

4. SPONTANEOUS EMERGENCE OF SPACE STEMS AHEAD OF NEGATIVE LEADERS IN LIGHTNING AND LONG SPARKS

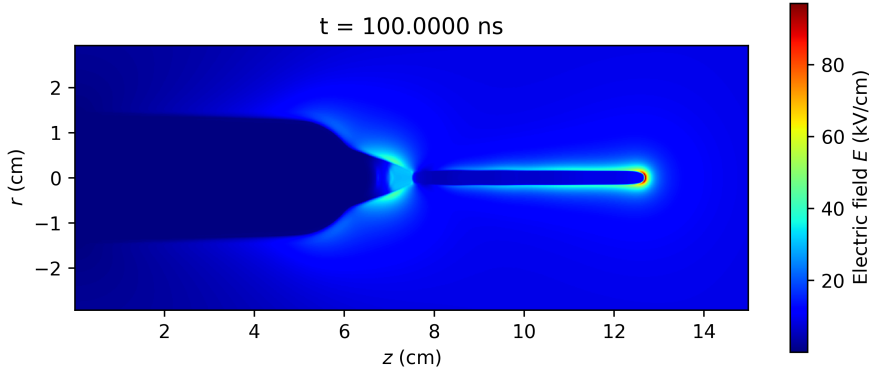


Figure 4.4: Positive streamer propagating in a background field of 7 kV/cm after 100 ns. The attachment instability is triggered close to the leader tip, where the electric field is locally enhanced. This supports the idea that isolated stems cannot exist in positive leader

streamers (*Luque et al.*, 2008) for the same external field. Besides, positive streamers are initiated more easily (*Liu et al.*, 2012) so they are launched from the leader tip at a lower potential and thus a lower driving electric field than negative streamers. To check this explanation we run simulations of positive streamers under driving electric fields of 10 kV/cm and 7 kV/cm; there the attachment instability was triggered only in regions of the channel very close to the leader tip (see fig. 4.4), supporting the idea that steps in positive leaders exist but they are so small that isolated space stems cannot be observed.

4.3 Two-Sphere Model for a Leader Corona

In the previous section we described in detail the initial 100 ns of the streamer-to-leader transition. This time is sufficient to establish the space stem but it is clearly too short to reach the characteristic temperatures inside a leader. Unfortunately, for the reasons explained there, currently microscopical models cannot be extended to long times. However, we may obtain a glimpse of the most important physics at these longer time scales.

We present here a streamlined and heavily simplified model of the corona ahead of a leader. Although it is clearly insufficient to produce accurate predictions, it illustrates two things of the physics of the streamer-to-leader transition: (1) that for the streamer-to-leader

transition to occur there must be a mechanism that either creates new streamers or increases the conductivity of existing channels by means of consecutive ionization waves and (2) that a small difference in initial electron density in the stem leads to large differences in the heating rate of this segment compared to the rest of the corona.

4.3.1 Model Description

The model's geometry is sketched in figure 4.5. The leader tip is mimicked by a conducting sphere of radius a at a potential V_L , whereas the electric charge in the corona is distributed within another sphere with radius b . The centers of the two spheres are separated by a length L . In order to simplify our calculations we assume that the corona sphere has a uniform potential V_C arising from a total corona charge Q_C . The electrostatic system of two conducting spheres with potentials V_L , V_C and charges Q_L and Q_C is defined by a capacitance matrix C such that

$$\begin{pmatrix} Q_L \\ Q_C \end{pmatrix} = \begin{pmatrix} C_{LL} & C_{LC} \\ C_{CL} & C_{CC} \end{pmatrix} \begin{pmatrix} V_L \\ V_C \end{pmatrix}, \quad (4.4)$$

where the elements of C can be calculated by repeated application of the method of images. From (4.4) we obtain

$$V_C = -\frac{C_{CL}}{C_{CC}}V_L + \frac{Q_C}{C_{CC}}. \quad (4.5)$$

The two spheres are connected by streamer channels, which this model represents as linear electric resistors. Of these, N are identical, unperturbed resistors of length L (we neglect differences in these distances) whereas one perturbed channel contains the space stem and is thus divided into three serially connected resistors: the space stem, of length ℓ is surrounded by two channels of length $(L - \ell)/2$.

The current inside each resistor is generated by the drift of current carriers, each with mobility μ_s , where $s = 1, \dots$ indexes the species (this includes electrons and positive and negative ions). The underlying charge carrier densities and mobilities in the streamers are respectively $n_{0,s}$ in the unperturbed, long channels, $n_{\text{stem},s}$ in the stem and $n_{1,s}$ in the two channel segments surrounding the stem. These densities are uniform within the channels, all of them of cylindrical shape and with a radius r .

4. SPONTANEOUS EMERGENCE OF SPACE STEMS AHEAD OF NEGATIVE LEADERS IN LIGHTNING AND LONG SPARKS

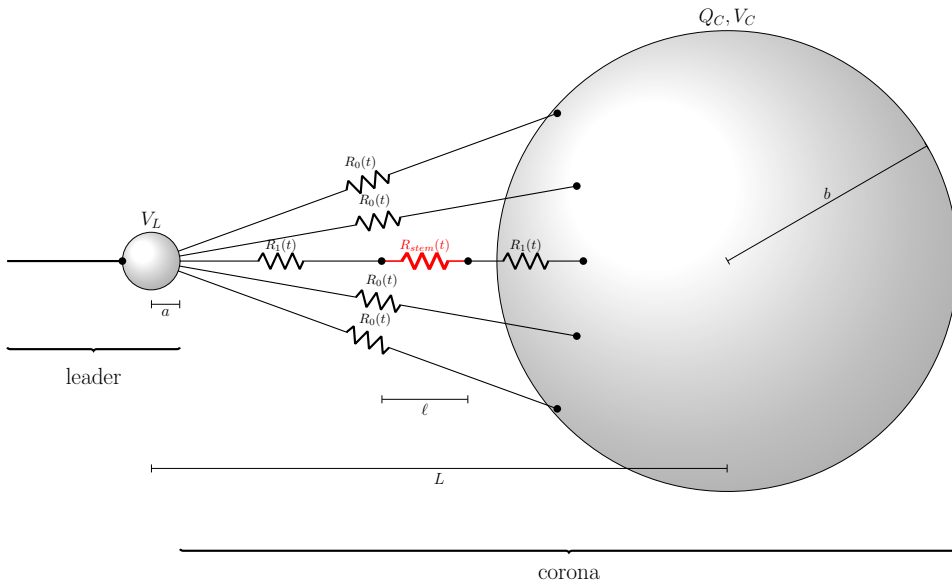


Figure 4.5: Sketch of the model. Two conducting spheres, representing respectively the leader tip and the corona space charge are connected by channels representing the streamer discharges. Most of these channels are uniform and modeled as single resistors. One of the channels is perturbed to contain a space stem, represented by a different resistor (shown in red).

Assuming now that the electric field that drives the charge carriers inside each channel can be approximated by its average, we obtain the current in the unperturbed channels as

$$I_0 = \frac{\pi r^2 e (V_L - V_C)}{L} \sum_s \mu_s n_{0,s} = \frac{V_L - V_C}{R_0}, \quad (4.6)$$

where the resistance R_0 is defined as

$$R_0 = \frac{L}{\pi r^2 e} \left(\sum_s \mu_s n_{0,s} \right)^{-1}. \quad (4.7)$$

Defining similarly the resistance of the stem as

$$R_{\text{stem}} = \frac{\ell}{\pi r^2 e} \left(\sum_s \mu_s n_{\text{stem},s} \right)^{-1}, \quad (4.8)$$

and that of the two channel surrounding the stem as

$$R_1 = \frac{(L - \ell)}{2\pi r^2 e} \left(\sum_s \mu_s n_{1,s} \right)^{-1}, \quad (4.9)$$

yields for the current in the perturbed channel

$$I_1 = \frac{V_L - V_C}{R_{\text{stem}} + 2R_1}. \quad (4.10)$$

The charge accumulation in the corona then follows

$$\frac{dQ_C}{dt} = NI_0 + I_1. \quad (4.11)$$

The species densities evolve according to the chemical system described in the main text subjected to electric fields averaged over the extension of each path, which can be calculated from Ohm's law as $\bar{E}_c = R_c I_c / l_c$, where c indicates the kind of channel (unperturbed, stem or stem-neighbors) and l_c is the channel's length. Furthermore, each channel dissipates energy at a rate $R_c I_c^2$ and therefore its temperature increases at a rate

$$\frac{dT}{dt} = \frac{\eta R_c I_c^2}{\pi r^2 l_c n_{\text{air}} c_V}, \quad (4.12)$$

where n_{air} is the number density of air at standard temperature and pressure and c_V is the specific heat capacity of air, which we take as $c_V = (5/2)k_B$, k_B being Boltzmann's constant.

4. SPONTANEOUS EMERGENCE OF SPACE STEMS AHEAD OF NEGATIVE LEADERS IN LIGHTNING AND LONG SPARKS

Parameter	Value
L	1 m
a	1 cm
b	25 cm
r	0.5 mm
V_L	1 MV
N	50

Table 4.1: Parameter values employed in our simulations.

Note that as the stem heats up some processes that are not included in our chemical model, such as vibrational-translational relaxation, play an increasingly significant role. Therefore high temperatures in this simplified model cannot be considered as quantitative predictions.

The parameters used in the following simulations are listed in table 4.1. As initial conditions we set an electron density $n_e = 10^{19} \text{ m}^{-3}$, balanced by N_2^+ and O_2^+ in a ratio matching the air fractions of molecular nitrogen and oxygen. In the “stem” resistor this initial density is reduced by a factor 0.75. Once this different initial condition is set, all resistor follow the same evolution equations. Note that our input values have not been fine-tuned to obtain the results described below.

4.3.2 Single Corona Discharge

As a first step, let us check that results from this simplified model are broadly consistent with the fluid model described in section 4.2. Figure 4.6 shows the evolution of the most relevant variables of the model. The main result is that, as we noticed in section 4.2, the electron density is depleted with a time scale of around 100 ns. Hence the temperature in any of the channels does not increase further than a few Kelvin. However, the small perturbation in electron density introduced in the “stem” channel is sufficient to excite the attachment instability described and thus drives this component to higher electric fields and more dissipation. The increase in temperature is thus significantly higher in this segment but still far below that needed to transition to a leader.

Note however that the potential drop between the leader and the corona has barely

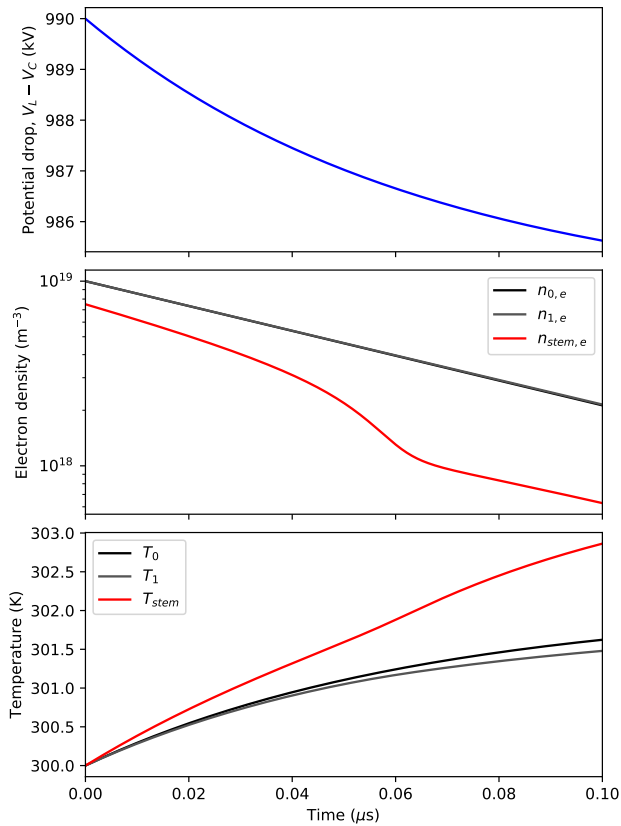


Figure 4.6: Simulation of a single corona discharge in the two-sphere model. Here we show 100 ns of simulation. The top panel shows a small decrease in the potential drop; the central panel shows that the electron density decays quickly, faster in the space stem than in the other channels. Finally, the lower panel plots a small increase of gas temperature, which is nevertheless much more significant in the stem.

4. SPONTANEOUS EMERGENCE OF SPACE STEMS AHEAD OF NEGATIVE LEADERS IN LIGHTNING AND LONG SPARKS

bulged and there is still a high potential in the leader that is available to initiate new discharges.

4.3.3 Multiple Discharges

We hypothesize that the large electrostatic potential remaining at the leader tip after the electron density has been depleted generates subsequent ionization waves that prevent the conductivity region ahead of the leader tip to disappear completely. To substantiate this hypothesis we provide here an example of how the physics of the streamer-to-leader transition may work on long time scales after the space stem has formed.

Assume then that due to its high potential, the leader tip launches successive streamer-like ionization waves that propagate along or close to previous existing channels. A similar process was observed by *Nijdam et al.* (2014). As an example, let us assume that these waves are launched every 100 ns and that their effect is to increase the channel ionization by a factor 10. Given their fast time scales, these ionization waves can be implemented in our model by instantaneous increases of the electron and ion densities.

The result is plotted in figure 4.7, where we show the evolution of the system after 10 ionization waves. The gas heating in this case is stronger, with the stem reaching a temperature close to 800 K compared to only about 400 K for the rest of the corona channels.

4.4 Discussion and Conclusions

Our simulations show that the attachment instability explains the features of space stems ahead of propagating leaders. However at around 100 ns the overall conductivity of a streamer channel decays, stalling the increase in temperature. Our results thus stress the role in maintaining the corona played by poorly understood processes such as the inception of counter-propagating streamers (*Kochkin et al.*, 2016; *Luque et al.*, 2016b) or the propagation of successive ionization waves along pre-existing channels (*Phelps*, 1974; *Nijdam et al.*, 2014; *Babich et al.*, 2015; *Rison et al.*, 2016). Previous models (*Popov*, 2003; *da Silva and Pasko*, 2013) missed the relevance of these processes because they were not self-consistent and set a constant current intensity in the channel. In these models a reduction

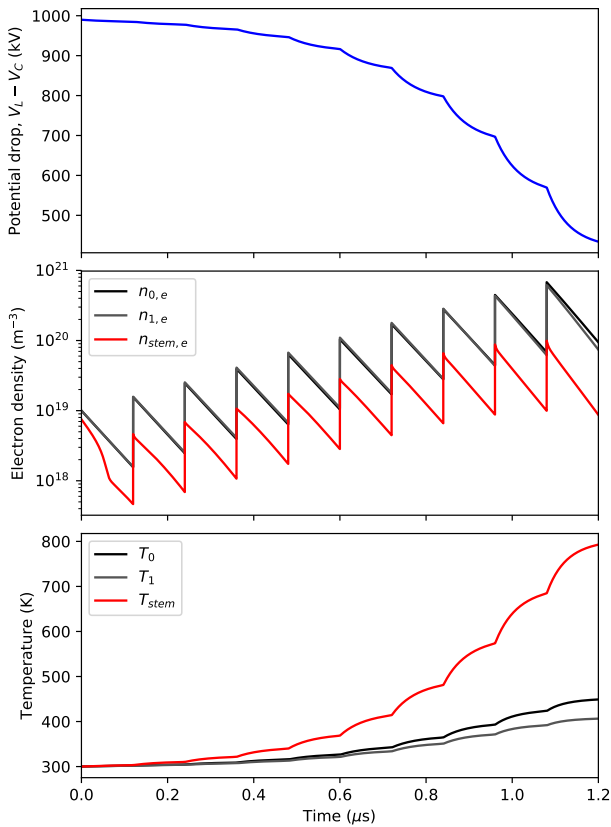


Figure 4.7: Corona discharge followed by multiple ionization waves that sustain a high ionization in the streamer channels. In this case the electrostatic potential drop (top panel) decays significantly, whereas the electron density (middle panel) increases slowly. The temperature of the channels (lower panel) increases up to around 800 K for the stem and only to around 400 K for the rest of the channels.

4. SPONTANEOUS EMERGENCE OF SPACE STEMS AHEAD OF NEGATIVE LEADERS IN LIGHTNING AND LONG SPARKS

of the electron density is immediately counteracted by an increase in the applied electric field so electrons are never significantly depleted. However, no physical mechanism with such an effect has been described in the literature.

As we have already shown, a single streamer discharge is unable to dissipate enough power to transit into a leader. Nonetheless, the relatively poor conductivity of a streamer corona together with a variable potential at the leader tip imply that there is often a significant electric field within the corona. This field triggers either new streamer bursts, as observed by *Kochkin et al.* (2014) or ionization waves retracing previous streamers, as proposed by *Babich et al.* (2015). It is also responsible for counter-streamers seeded by charges in existing stems. Remarkably, all of these mechanisms have been linked to X-ray emissions from long sparks (*Kochkin et al.*, 2015; *Østgaard et al.*, 2016; *Ihaddadene and Celestin*, 2015; *Köhn et al.*, 2017; *Babich and Bochkov*, 2017; *Luque*, 2017; *Babich et al.*, 2015) and these X-rays are in turn linked to leader stepping (*Dwyer et al.*, 2005).

To check that these mechanisms may indeed explain the streamer-to-leader transition within the currently established observational constraints, we have developed a simplified model of a leader corona that we describe in section 4.3. The model shows that ionization waves increasing the electron density a factor of ten and repeating every 100 ns would lead to a significant increase of the temperature of the channel. But the main outcome is that a small difference in initial electron density in the stem leads to large differences in the heating rate of this segment compared to the rest of the corona.

An important simplification of our model is the assumption that a space stem can form within a single streamer channel and that streamer branching, even if present, is not an essential ingredient in the process. We base this assumption in two key observations: (1) space stems are generally observed as bright segments within longer, dimmer channels (*Biagi et al.*, 2010; *Hill et al.*, 2011) and (2) in laboratory images negative streamer coronas contain thick, almost-straight channels with extensions of up to one meter (*Kochkin et al.*, 2014; *Kostinskiy et al.*, 2018). Although these channels are surrounded by smaller streamers, there is no reason to believe that these short bifurcations play an essential role in the dynamics of the main channel. Interestingly, this is not the case for positive coronas (*Kochkin et al.*, 2012; *Kostinskiy et al.*, 2018), which may be yet another reason for the polarity asymmetry in leader propagation.

Our results explain the formation of brighter and warmer inhomogeneities ahead of a negative leader channel. This is the first stage in the streamer-to-leader transition in a stepped leader. The subsequent evolution of the space stem is still not understood: namely we do not know the mechanism that maintains the corona conductivity long enough to reach thousands of degrees. A full understanding of lightning progression and associated phenomena such as the emission of X-rays will only result from the successful investigation of this mechanism.

4. SPONTANEOUS EMERGENCE OF SPACE STEMS AHEAD OF NEGATIVE LEADERS IN LIGHTNING AND LONG SPARKS

Chapter 5

On the emergence mechanism of carrot sprites

5.1 Introduction

First reported by *Franz et al.* (1990), sprites are filamentary electric discharges that develop tens of kilometers above thunderclouds (55-80 km altitude). Early work by *Pasko et al.* (1996, 1998); *Raizer et al.* (1998) suggested that sprite filaments are streamers, as was later confirmed by high-speed observations (*Stanley et al.*, 1999; *Cummer et al.*, 2006; *McHarg et al.*, 2007; *Stenbaek-Nielsen and McHarg*, 2008). Nowadays it is accepted that sprites originate from a quasi-electrostatic field produced by uncompensated electric charges due to lightning in the troposphere (*Pasko et al.*, 1995, 1997). Several works (*Luque and Ebert*, 2009; *et al.*, 2015; *Köhn et al.*, 2019; *Wu et al.*, 2019) point out to the presence of inhomogeneities as a requirement for the initiation of sprite streamers.

After the streamer head passage, the streamer wake develops column-like (glows) and spot-like (beads) intricate luminous patterns (*Stenbaek-Nielsen and McHarg*, 2008; *Stenbaek-Nielsen et al.*, 2020). Here we adopt the term "glow" following previous works (*Stenbaek-Nielsen et al.*, 2013; *Luque et al.*, 2016a). These structures fade out on time scales spanning from a few milliseconds to a few hundred milliseconds (*Luque et al.*, 2016a). Observations (*Stenbaek-Nielsen and McHarg*, 2008; *Stenbaek-Nielsen et al.*, 2020) report glows expanding and merging with beads, sometimes seeding the launch of upward-

5. ON THE EMERGENCE MECHANISM OF CARROT SPRITES

sideways streamers. Previous work about the launch of upward streamers in sprites assumed that they emerge from the negative tip of a double-headed streamer (*Qin et al.*, 2012, 2013b), but this does not seem to be supported by observations.

Different numerical models indicate that the long-lasting emissions from glows (*Luque and Ebert*, 2010; *Liu*, 2010) and beads (*Luque and Gordillo-Vázquez*, 2011) stem from a persistent electric field and current. *Luque et al.* (2016a) suggested the attachment instability (*Douglas-Hamilton and Mani*, 1973, 1974) as the mechanism responsible for glows and beads. Simulations show the formation of glow-like structures at altitudes above which the electric field can excite the attachment instability. The situation for beads is still unclear: they often appear as periodic patterns in observations. *Luque et al.* (2016a) proposed that they emerge from pre-existing horizontal modulations of the atmosphere.

Based on their shape, sprites are classified as carrot-sprites or column-sprites (*Wescott et al.*, 1998; *Stenbaek-Nielsen and McHarg*, 2008). The main difference is that column sprites only propagate downwards whereas carrot sprites also shoot upward-sideways streamers in a second stage of evolution. The inception of these streamers is related to the evolution of the inner electric field in the streamer body and therefore it depends on the transport of charge and the dominant plasma chemistry.

In the previous chapter, we showed the spontaneous emergence of a space stem precursor due to the action of the attachment instability in a region of the streamer channel separated from the leader tip. Nonetheless, after 100 ns the temperature stops increasing as a result of a decreasing conductivity in the streamer channel. In sufficiently long spark discharges, space stems are promoted to space leaders through the heating caused by an electric current flowing through them. The mechanisms maintaining the current are so far uncertain as we have discussed in chapter 4. However, experiments (*Kochkin et al.*, 2016) show that space stems are able to shoot counter-propagating streamers which may be responsible for extending the space stem lifespan. As we have described above, a similar phenomenology is observed in a sprite streamer glow, reminiscent of a "cold" space stem precursor.

In this chapter we aim to study the mechanism underlying the development of carrot-sprites. From this we can get an insight into the mechanism that enables space stems to shoot counter-propagating streamers and understand its later development.

This chapter is organized as follows: in section 5.2 we describe the 3D model used to study sprite glows and the emergence of upward streamers. This model is implemented in Afivo-streamer code (Teunissen and Ebert, 2017; and Teunissen, 2019), based on the Afivo framework (Teunissen and Ebert, 2018). In section 5.3 we provide observations of a carrot sprite. In section 5.4 we present and discuss our simulation results and compare them with the observation.

5.2 Sprite streamer model

To study the evolution of the upward streamer and the glow itself we use a 3D streamer model. The equations underlying this model are described in chapter 2. This model does not include the gas dynamics so we are left with the drift-diffusion-reaction equations for electron and ions 2.2 and the Poisson equation 2.3.

Here, we consider ions as motionless over time scales of interest (a few milliseconds).

Regarding the chemistry, we have tested two kinetic schemes. The first one (Luque *et al.*, 2016a) includes electrons, N_2 , O_2 , O_2^+ , N_2^+ and O^- and accounts for impact ionization and dissociative attachment. The second one is an extended version with more species and some other processes such as electron detachment. A detailed description of this second model can be found in the supplementary material of Luque *et al.* (2017). Whereas the first model agrees well with observations, the second does not reproduce the long lasting emissions from glows and beads and the exponential decay of the channel reported by observations (a similar problem was discussed by Luque *et al.* (2016a)). Hence, we only present the results of the simpler chemical scheme.

To validate our results against observations, we computed the electron impact excitation of nitrogen molecules to the $N_2(B^3\Pi_g)$ and $N_2(C^3\Pi_u)$ electronic states which radiate in the first and second positive systems of N_2 (for details, see section A.1 in the Appendix).

Our starting point is a single sprite streamer channel right after the streamer head passage. Thus, our initial condition consists of a vertical neutral column. Detailed streamer simulations show that 1) the radial electron density profile is well approximated by a truncated parabola (Luque and Ebert, 2014) and that 2) $n_e \propto n_{air}$ when the streamer runs into increasing air density (Luque and Ebert, 2010). As the streamer propagates downwards,

5. ON THE EMERGENCE MECHANISM OF CARROT SPRITES

branching or not, it transports positive charge to the lower region that leads to the decay of the sprite. To model this we add neutral electron-ion densities in the shape of a truncated funnel attached to the bottom of the column. Figure 5.1 shows the initial electron density, that reads (Luque *et al.*, 2016a)

$$n_{e,ch}(r, z) = \begin{cases} n_{e0,ch}(z) \frac{a_0^2}{a(z)^2} \max\left(0, 1 - \frac{r^2}{a(z)^2}\right), & \forall r \quad 50 \text{ km} < z < 80 \text{ km} \\ 0 & \text{elsewhere,} \end{cases} \quad (5.1)$$

where $n_{e0,ch}(z) = C n_{air}(z)$ is the electron density at the axis of the column, $n_{air}(z) = n_{air,0} e^{(-z/7.2 \text{ km})}$ is the air density scaled at altitude z from the ground air density $n_{air,0} = 2.5 \times 10^{25} \text{ m}^{-3}$ and $C = 3.33 \times 10^{-11}$. The value of C is determined from the equality $n_{e0,ch}(60 \text{ km}) = 2 \times 10^{11} \text{ m}^{-3}$. The factor $a_0^2/a(z)^2$ ensures that the total electron density integrated in a horizontal cross section extends smoothly from the funnel to the column. The term a_0 is the radius of the column and $a(z)$ is a continuous piecewise linear function modeling the radius of the channel and the funnel. The funnel is characterized by the radius of the base (5 km), its altitude ($z_b = 50 \text{ km}$) and the vertex altitude ($z_u = 60 \text{ km}$):

$$a(z) = \max\left(a_0, \frac{z_u - z}{z_u - z_b} \times 5 \text{ km}\right). \quad (5.2)$$

Outside the channel our background electron density follows a Wait-Spies profile (Wait and Spies, 1964), $n_{e,bg} = 10^{-2} \text{ cm}^{-3} \exp\left(-\frac{z-60 \text{ km}}{2.86 \text{ km}}\right)$ (Hu *et al.*, 2007).

For the results that we present in this chapter the computational domain is a $20 \times 20 \times 40 \text{ km}^3$ box starting at 40 km altitude and the finest resolution is 1 m. To solve Poisson's equation, we ground the bottom boundary and set the top boundary to 2.9 MV. This is equivalent to a background electric field of 72.38 V/m pointing downwards, that yields a reduced electric field E/n_{air} of approximately 120 Td at around 77 km. For the lateral boundaries we set homogeneous Neumann boundary conditions. We also apply Neumann boundary conditions at the six boundaries to solve electron and ions equations.

Our 3D model is implemented in Afivo-streamer code (Teunissen and Ebert, 2017; and Teunissen, 2019), which is based on the Afivo framework (Teunissen and Ebert, 2018). This framework includes geometric multigrid methods to solve Poisson's equation, octree-based adaptative mesh refinement and OpenMP parallelism. Plasma-chemical reactions

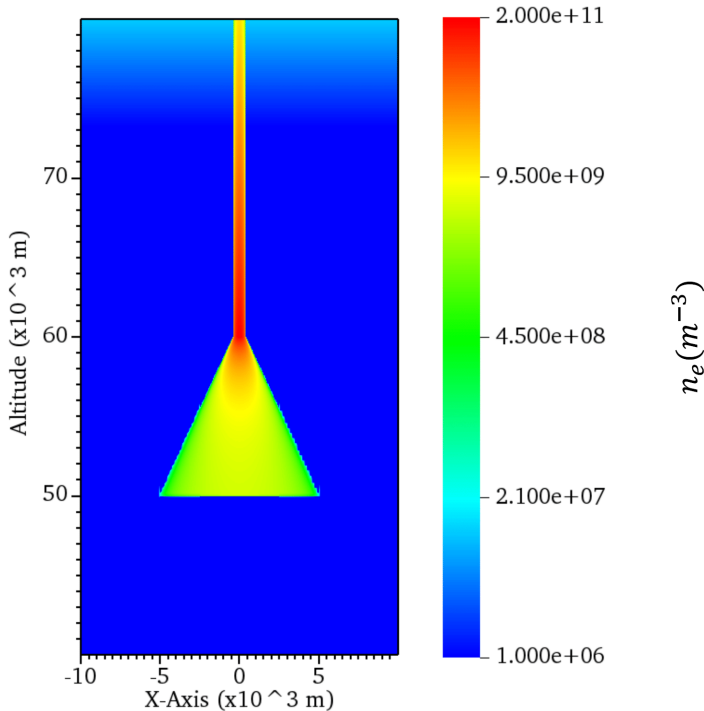


Figure 5.1: The initial electron density consists of a vertical column and a truncated funnel attached to the bottom of it. The funnel models the effect of a propagating positive streamer corona on the background electric field.

and variations in the air density are newly added in Afivo-streamer code for the present simulations.

Afivo-streamer code also includes a 2D cylindrically symmetric version of the model explained above. We have used this 2D version as a probe for suitable conditions to launch upward streamers. These tests show that a sufficiently high vertical electric field suffices to launch upward conical ionization waves. In 3D, this implies that many streamers would emerge from the glow since there is no preferred direction. Under these conditions, our 3D simulations are unapproachable because the extent of the finest grid would be too large. Therefore, we add a small lateral component to the background electric field to break the symmetry. By doing this we are able to study the propagation of single upward

streamer, although more streamers emerge at later stages of our simulations. We have tested several lateral electric fields, however we present the results of a representative simulation, $\mathbf{E}_{\text{background}} = (18, 0, -72.38) \text{ V/m}$. The initial (neutral) charge distribution will rapidly evolve to screen the background electric field.

One typical 3D simulation, where the finest grid size is 1 m, took 3 days in 32 cores. We have checked the convergence of our results by systematically increasing the resolution in our simulations, down to a mesh size of 0.5 m. Practically the same results were obtained for a grid cell size at and below 1 m. Therefore, in this chapter we show results calculated for 1 m grid spacing.

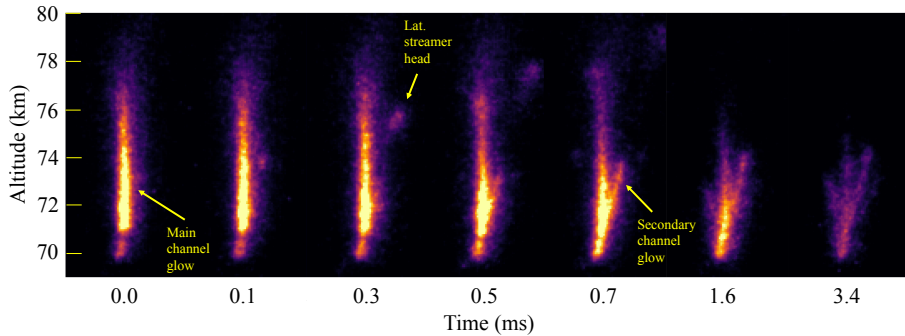


Figure 5.2: Time series from high-speed video observations of a sprite. The sequence shows the sprite glow and the upward streamer launch, propagation and the optical extinction of the glow. The time origin was set in the first frame prior to the launch of the upward streamer. To emphasize the main milestones of the evolution, intervals between the snapshots are not uniform.

5.3 Observations

In this section we present observations of the emergence of an upward streamer from a glowing segment. After inspecting multiple high-speed sprite observations provided by courtesy of H. C. Stenbaek-Nielsen and M. G. McHarg, we selected one event where this process is particularly clear. Consistent with earlier results by *McHarg et al. (2007)*, in all these observations we did not find any event where it could be definitely concluded that an upward streamer did *not* emerge from a glow.

The selected event occurred on 5 July 2011 at 08:54:14 UTC and was associated with a large thunderstorm complex over north-eastern South Dakota, USA. The event was observed with a Phantom high-speed imager recording at 10,000 frames per second onboard an aircraft flying at 14.4 km altitude over south-eastern South Dakota about 180 km north of the storm.

Figure 5.2 shows a time sequence of the recorded event with seven 3.29×1.55 degree subsections from the original 15.23×7.54 degree field of view Phantom images. Once the main channel glow is established, a negative streamer launches and propagates upward, causing a noticeable decrease of the light emissions of the upper part of the glow. Also remarkable is the formation of a secondary channel glow as highlighted in the figure.

We do not have the location of the event or the causal lightning stroke, but NLDN reported 5 strikes within about 1 second of the event, all in the region within the Phantom field of view. Assuming that the event is over that region, the range of 180 km mentioned above, defines the altitude scale shown. Because sprites may occur several tens of km from the causal strike (Stenbaek-Nielsen et al., 2008) there is considerable uncertainty on the altitude. This event was observed at an elevation angle of about 18 degrees and an increase in range by 10 km will increase the altitude by 3.3 km.

5.4 Results and Discussion

Now we focus on our numerical simulations. Figure 5.3 shows the evolution of the sprite channel through different milestones: glow formation, upward streamer launch and propagation and glow deactivation. After 1 ms the initial channel appears sharply segmented into high and low conductivity regions below and above 70 km respectively. The emissions in the First Positive System of molecular nitrogen (1PN2) (third row in fig. 5.3), can be compared with the recorded event shown in Fig. 5.2. In both simulation and observations, the lower region is almost dark whereas the low conductivity region glows strongly. 1PN2 emissions are determined by the electron density and the reduced electric field. Despite its low conductivity, the upper region emits more intensely because the excitation rate of the 1PN2 is highly non-linear in the reduced electric field as figure 5.4 shows. This glowing structure in the upper part of the channel agrees with observations, as the first frame

5. ON THE EMERGENCE MECHANISM OF CARROT SPRITES

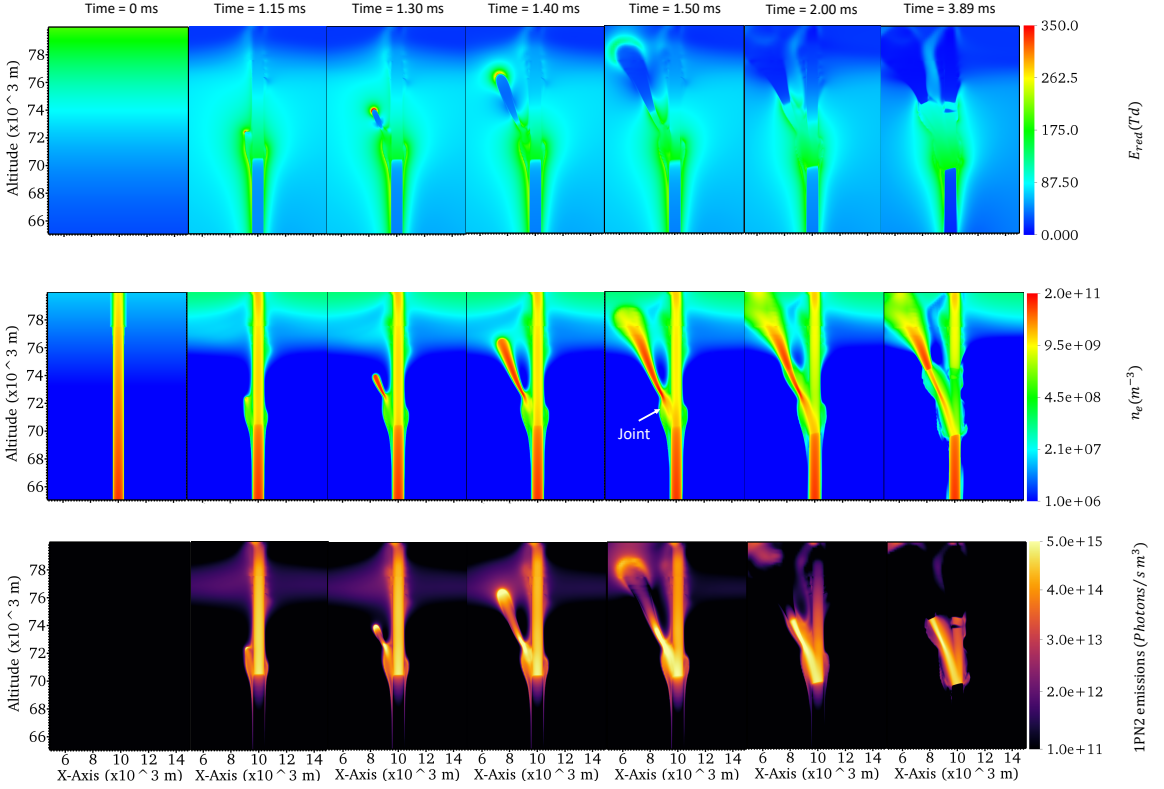


Figure 5.3: Cross sections of a 3D simulation in a box domain $20 \text{ km} \times 20 \text{ km} \times (40 - 80) \text{ km}$. We show the evolution in terms of the reduced electric field (top row), the electron density (middle row) and the emissions in the First Positive System of molecular nitrogen (1PN2). The channel develops a sharply defined region above 70 km characterized by high reduced electric fields and low conductivity that strongly emits in the 1PN2 for a long time. At 1.15 ms, a negative streamer emerges close to the lower boundary of the glowing structure, propagates upwards and connects to the electron reservoir in the upper region of the computational domain. The rightmost two columns highlight the effect of the upward streamer on the 1PN2 emissions for altitudes above 76 km.

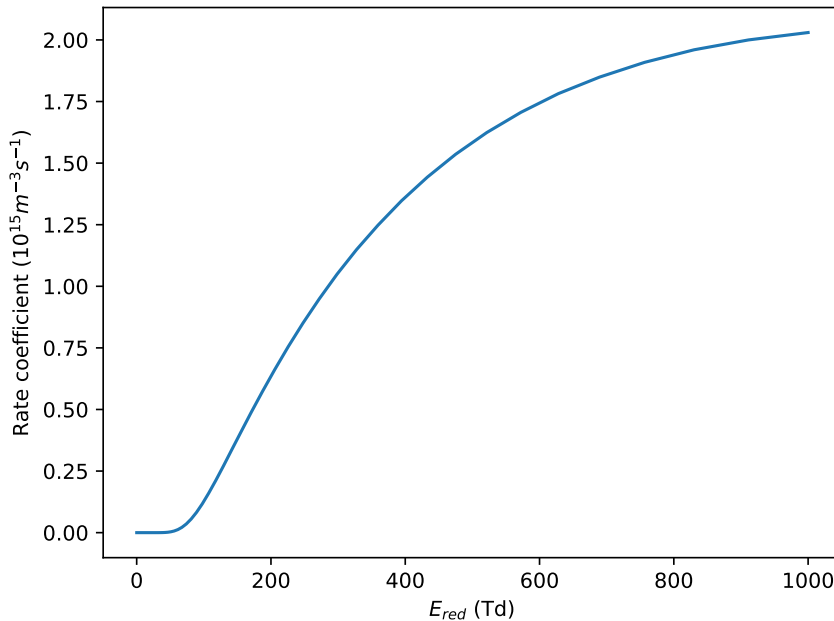


Figure 5.4: Non-linear behaviour of the rate coefficient for the production of $\text{N}_2(B^3\Pi_g)$.

of Fig. 5.2 shows. In chapter 4 we saw that the appearance of this glowing structure is driven by the attachment instability (*Douglas-Hamilton and Mani, 1973, 1974*), which is triggered by relatively high internal electric fields. This is the reason why sprite glows appear in the upper region of the sprite channel (*Luque et al., 2016a*).

The boundary of the glow region is characterized by a net negative charge density as previously shown by *Luque and Ebert (2010)*. This is due to current continuity: electrons drift upwards and, around 0.8 ms into our simulation, the electron density exceeds the density of positive ions. In the low conductivity region electrons are more effectively converted to negative ions which, being slower than electrons, accumulate there, leading to a surplus of negative charge that locally enhances the electric field. This electric field has both a vertical and a lateral component, and at some point, becomes high enough to launch a negative streamer near the lower boundary of the glow. The streamer propagates upwards with a velocity of 2×10^7 m/s, typical of streamer observations (*Stenbaek-Nielsen*

5. ON THE EMERGENCE MECHANISM OF CARROT SPRITES

et al., 2013), and connects to the electron reservoir in the lower ionosphere (see figure 5.3). This is very similar to previous works (*Pasko and Stenbaek-Nielsen*, 2002) and our results (fourth frame in fig. 5.3). Other works (*Li et al.*, 2011; *Bór*, 2013) show upward streamers bending towards the main streamer channel. In our simulation, the upward streamer propagation is mostly straight because we apply a small lateral field that charges negatively the side of the glow closer to the negative upward streamer, which is slightly repelled.

The left plot of fig. 5.5 shows the evolution of the electric current at different altitudes according to the following equation:

$$I = \int_{\Omega=\{r=[0,R],z=h\}} \mathbf{j} \cdot d\mathbf{s} = 2\pi \int_0^R j_z(r, z=h) r dr, \quad (5.3)$$

where j_z is the axial component of the current density at $z = h$, r is the radial coordinate (cylindrical coordinates) and R is the radial extent of the integration domain. Solid lines represent the electric current flowing through the main sprite channel ($R = 400$ m) while dashed lines are the current flowing through cross sections spanning the full lateral extent of the domain ($R = 20$ km). Initially in the main streamer channel (solid lines) the electric current at different altitudes quickly converges (~ 0.5 ms) to the same value despite the initial differences in the background electron density, air density and reduced electric field for each altitude. Afterwards (~ 1.4 ms), the upward streamer sets two regions below and above 70 km. In the whole system (dashed lines), we see sudden current increases at 74 km and 76 km. The peaks for those altitudes at 1.3 ms and 1.4 ms are due to the passing of the upward streamer head (*Luque et al.*, 2017).

As visible in fig. 5.3, the launch point of the upward streamer is slightly separated from the main channel. The resulting gap or joint initially has a low electron density but around 1.4 ms, this joint between the upward streamer and the main channel becomes more conductive (see Fig. 5.3) and, as a result, the currents at 68 km and 70 km slope upward. Right after, most of the current starts to flow through the secondary streamer channel, since its higher electron density allows for a higher conductivity, and within the next 0.3 ms and for altitudes above 70 km the current halves inside the central channel, which has lower electron density. In the system composed of both the main channel and the upward streamer channel, Kirchhoff's current law is a reasonable approximation despite not being strictly applicable to this finite-conductivity, non-steady-state system. The subsequent decay of

the currents at different altitudes seems to obey a similar decay constant. This decay is due to the transport of charges inside the streamer channel that increasingly screens the background electric field. Also noticeable is a current peak around 2.7-2.8 ms at 74 km. This is caused by two negative upward streamers that symmetrically emerge from the main channel, propagate upwards and reconnect to the main channel.

1PN2 emissions are useful to track the evolution of the main streamer channel and the impact of the secondary channel on it. In the right panel of fig. 5.5 we plot the evolution of the 1PN2 emissions integrated over 1 km-height boxes centered at the channel axis, with the lateral extension of the channel diameter (800 m). The emissions at 68 km rapidly drop due to the screening of the electric field. At other altitudes, specially at 76 km, the effect of the upward streamer is clear after the rise in conductivity in the joint between the upward streamer and the main channel (see Fig. 5.3). Above 70 km the upward streamer induces a reduction of the light emissions whereas below 70 km the emissions slightly increase. When the upward streamer effectively connects (joint becomes conductive enough) to the main streamer channel, the joint glows strongly (at around 1.5 ms in Fig. 5.3). In the observations of Fig. 5.2, this occurs around 0.3-0.5 ms. Later, the emissions in the upper section of the glow decay noticeably. The optical structure of the remnant emissions in the last two frames matches what we see in our simulations (Fig. 5.3), where most of the emissions come from the lower part of the glow and the region of the upward streamer channel closer to it.

The last stage in the evolution of the upward streamer in our simulation reveals an interesting result (fig. 5.3, last column). The secondary streamer channel develops a sharply defined glowing similar to the glow in the main channel. This portion of the secondary channel has entered the attachment instability regime at around 1.4 ms. As a result, the upper boundary of this structure is positively charged and, by a mechanism similar to the one we have described above, it may launch a positive downward streamer. The resulting optical emissions in that case would feature a vertical channel accompanied at its side by an inverted V. Although infrequently, this formation has indeed been observed and is called “angel” sprite (*Pasko et al.*, 2012; *Bór*, 2013).

As mentioned above, we tested two chemical models. We discarded one including detachment because it cannot reproduce long-lasting glows beyond the detachment time

5. ON THE EMERGENCE MECHANISM OF CARROT SPRITES

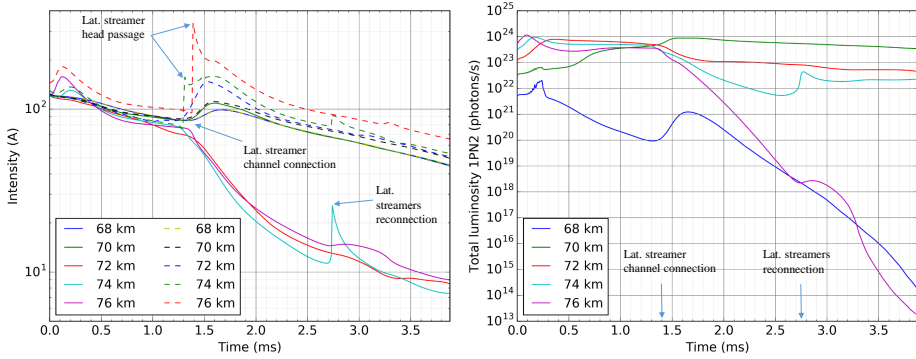


Figure 5.5: The left plot shows the evolution of the electric current flowing through the main streamer channel (solid lines) and the whole domain (dashed lines). Sudden peaks in the current reveal the passing of the upward streamer head at that altitude. At around 1.4 ms the upward streamer channel and the main streamer channel get effectively connected cutting off the current flowing in the main channel above 70 km. Subsequent peaks in the current at different altitudes are caused by two negative streamers that emerge from the glow and reconnect to the main channel. The plot to the right shows the emissions from the IPN2 integrated over a 1km-height box. It clearly shows the effect of the upward streamer, specially at 76 km. Nonetheless, there is also a decrease in the luminosity for 72 km and 74 km.

scale around 2 ms. An extensive discussion about the implications of detachment on the glow emissions can be found in *Luque et al. (2016a)*. According to other simulations that we do not provide here, detachment delays the upward streamer but does not prevent it as long as its onset occurs before 2 ms (in our simulations) .

The morphology of the sprite is related to the electric field at mesospheric altitudes. We tested electric fields with smaller vertical components, and we found that for lower electric fields the glow is shorter. This means that the upward streamer, if it were to appear, would emerge later. If the glow is too small to accumulate enough charge at the lower boundary, it is unlikely that it launches upward streamers. Column-sprites, which are associated to less intense electric fields (*Qin et al., 2013a,b*), would hardly launch upward streamers.

5.5 Conclusions

Our simulations show for the first time the evolution of a sprite streamer channel where a glow region forms in its upper part and launches several upward streamers. We have proposed a mechanism for the emergence of carrot sprites: the sprite glow results from an attachment instability that seeds the lower boundary of the glow with negative charge that locally enhances the electric field and finally launches an upward negative streamer. The evolution of the upward streamer and the glow itself agrees well with observations for the time scales we have simulated. Essentially, the upward streamer cuts off the current flowing from the lower part of the sprite channel to the glow region, which then darkens. This agrees with many observations where the glow gets dimmer once the upward streamers are emitted. Of course, the details depends on the strength and number of upward streamers. In their last stage, our simulations reveal a region in the upward streamer that mimics the glowing structure in the main channel. We have seen that positive charge accumulates in its upper boundary. This new region might be the origin of positive downwards streamers which would give rise to the “angel” sprite structure (*Pasko et al., 2012; Bór, 2013*). Observations rarely report “angel” sprites and in our simulations, we have not succeeded in reproducing them. Therefore, its production must be constrained to a small subset in our parameter space.

There is still a puzzling question concerning the electron detachment in sprite simulations. It is a process that we should consider to study the streamer propagation for sufficiently long times. However, results point out that detachment should somehow be suppressed or treated in a different way. At atmospheric pressure the presence of a sufficiently high water concentration effectively suppresses the electron detachment (see chapter 4). Noctilucent clouds reveal the presence of water at sprite altitudes. Whether this suffices to affect detachment noticeably is still unknown. Nevertheless, water is a candidate to be considered in future work.

In this chapter we have seen how the attachment instability is able to develop sharply defined regions in sprite streamer channels that readily launch upward-sideways streamers. This could be somehow similar to those streamers that emerge from the space stem precursor. We have also seen that the electron detachment is closely related to the lifetime

5. ON THE EMERGENCE MECHANISM OF CARROT SPRITES

of persistent glowing structures in sprites. In the next chapter we will explore the influence of water in the space stem development as well as the role of secondary streamers in sustaining the electron conductivity in this region.

Chapter 6

Stepping mechanism in humid air

6.1 Introduction

An outstanding problem in long spark discharges is the polarity asymmetry: Observations of natural and artificial lightning (*Hill et al.*, 2011; *Biagi et al.*, 2010, 2014; *Gamerota et al.*, 2014; *Jiang et al.*, 2017), as well as laboratory long spark discharges (*Les Renardières group*, 1978a; *Gorin et al.*, 1976), show that in virgin air negative leaders propagate in a stepped manner, mediated by an isolated segment in the streamer corona, the space stem. On the other hand, positive leaders propagate in a continuous fashion in the most common laboratory conditions of dry air and fast rise-time voltage generators. (*Les Renardières group*, 1978b; *Domens et al.*, 1991; *Gallimberti et al.*, 2002).

By stepping, we mean an abrupt elongation of the leader channel followed by a streamer corona outburst emerging from the new leader tip. The stepped propagation is not exclusive of negative leaders. In lightning, positive leaders exhibit both, continuous and stepped propagation (*Rakov and Uman*, 2003b; *Wang et al.*, 2016; *Srivastava et al.*, 2019; *Gao et al.*, 2020). Some authors (*Saba et al.*, 2015) argue that in some cases, the stepped propagation of positive leaders may be triggered by steps of a negative leader tip at the opposite end of the channel and therefore not a feature of its own. However, studies of laboratory positive leaders carried out by *Les Renardières group* (1978b) and more recently by *Kostinskiy et al.* (2018) observed the abrupt elongation of positive leaders in conditions where they could discard an induced stepped propagation.

Yet, an important feature is still missing in the positive leader stepping. The observation of space stems is limited. *Kostinskiy et al. (2018)*; *Huang et al. (2020)* observed the formation of space-stem-like structures in the streamer corona of positive stepped leaders under high humidity conditions. Similar structures were observed in stepped positive leaders in triggered lightning by *(Jiang et al., 2020)*. In none of these cases, it is clear whether these structures extend from the primary channel or there is an actual gap.

Humidity conditions seem to be a relevant factor to understand the stepped propagation of leader discharges. There are two well known effects on a streamer channel regarding the water vapor content of air (*Gallimberti, 1979*; *Phelps and Griffiths, 1976*): 1) an increase of the 3-body attachment rate and 2) it prevents the electron detachment from O^- and O_2^- through the formation of water clusters $O^-(H_2O)$ and $O_2^-(H_2O)_n$.

In chapter 4, we showed the formation of space stem precursors ahead of a leader channel and stressed the importance of water vapor on its onset. However, those results were limited to a time scale of 100 ns. This chapter is a step forward in the modeling of the streamer-to-leader transition. To do so, we update the model described in chapter 2 by extending the chemistry used in chapter 3, tracking the evolution of the N_2 vibrational energy, and taking into account the effects due to the non-equilibrium condition $T_V \gg T$. With our updated model we study the evolution of a space stem precursor for longer time scales under a current-driven approach in dry and humid air, trying to understand the effects of water vapor on the streamer-to-leader transition. The forced current is meant to mimic the effect of a counter-propagating streamer corona launched from the space stem.

6.2 Model

In this chapter, we study the early stages of the streamer-to-leader transition driven by an externally imposed electric current I that results from the inception of a counter-propagating streamer corona from the space stem. In chapter 3, we worked with temperatures of a few Kelvin above room temperature and therefore we considered the system decoupled from the vibrational degrees of freedom, i.e. the characteristic time of our system was much shorter than the vibrational-translational relaxation time scale.

This time, the system will reach 1000 K to 2000 K and a non-equilibrium vibrational evolution $T_V \gg T$. Thus, it is convenient to track the evolution of the vibrational energy of N_2 molecules, which is given by the following equation (*da Silva and Pasko, 2013*)

$$\frac{\partial \varepsilon_{vib}}{\partial t} + \nabla \cdot (\varepsilon_{vib} \mathbf{v}) = Q_{vib}^{eff}, \quad (6.1)$$

where ε_{vib} is the vibrational energy density and Q_{vib}^{eff} is the net energy density deposition rate in the vibrational degrees of freedom. The vibrational energy is related to the (effective) vibrational temperature T_V through the harmonic oscillator formula (*Capitelli et al., 2000*)

$$\varepsilon_{vib} = \frac{n_{N_2} \hbar \omega}{e^{\frac{\hbar \omega}{k_B T_V}} - 1}, \quad (6.2)$$

where $\hbar \omega = 0.29$ eV is the vibrational quantum of the N_2 molecule and n_{N_2} is the N_2 number density.

Note that in equation 6.1 we neglect the diffusion of vibrationally excited nitrogen molecules (*Shneider et al., 2012*) since the associated time scale is on the order of tens of microseconds, still far from the time scales that we will reach.

As we discussed in chapter 1, the drifting of charged species, that is, the electric current, underlies an energy exchange between charged particles and the neutral molecules of the background gas. The power density released by the electric current is given by equation 4.2. Figure 6.1 shows the energy flow of the Joule heating term Q . The ionic power Q_i is considered to instantly relax into translational energy (*da Silva and Pasko, 2013*). On the other hand, the electronic power Q_E is unequally distributed between the different degrees of freedom. Most of it goes to vibrationally excite nitrogen molecules (Q_V). The second largest contribution goes into the excitation of N_2 , O_2 and H_2O electronic states, including ionization. A small part of the electronic power is spent in elastic collisions Q_L and the excitation of rotational levels of N_2 but also O_2 and H_2O (*Capitelli et al., 2000*) Rotational levels quickly relax into translational energy and thus, we include them in the term Q_L . The electronic states are mainly deactivated by quenching collisions. The time scale associated with this energy exchange is shorter than the heating time scale and there-

6. STEPPING MECHANISM IN HUMID AIR

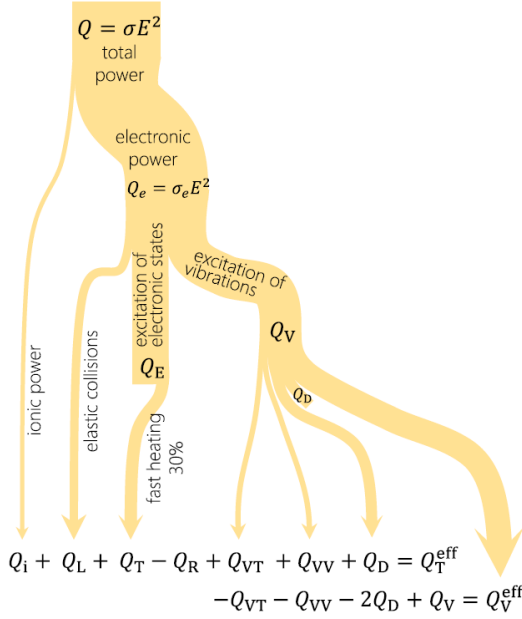


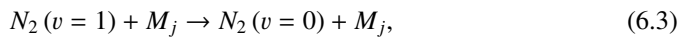
Figure 6.1: Energy flow chart that shows the partition of the Joule heating term Q into the different degrees of freedom of the background gas reproduced from *Liu and Becerra* (2017)

fore this contribution is referred as fast heating (*Popov*, 2011), usually denoted as Q_T . In this work we assume that $Q_T \approx 30\%Q_E$ (*Popov*, 2011).

Here, we calculate Q_V and Q_E using Bolsig+ (*Hagelaar and Pitchford*, 2005). For the electronic power, we take into account electron-impact reactions, step-wise ionization, excitation of electronic states, and electron-impact dissociation reactions (see section A.2 in the Appendix).

There are three different mechanisms for the vibrational-translational energy exchange that we note as Q_{VT} , Q_{VV} and Q_D in figure 6.1.

The term Q_{VT} refers to the vibrational-translational energy exchange in collisional-quenching deactivation of N_2 ($v = 1$) vibrations, that is,



where M_j denotes the species in Table 6.1. Q_{VT} is given by (Capitelli *et al.*, 2000)

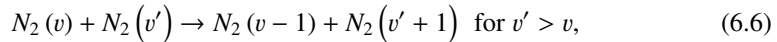
$$Q_{VT} = \frac{\varepsilon_{vib}(T_v) - \varepsilon_{vib}(T)}{\tau_{VT}}, \quad (6.4)$$

where τ_{VT} is the vibrational-translational relaxation time scale defined as (Chernyi, 2002)

$$\frac{1}{\tau_{VT}} = \left(1 - e^{-\frac{\hbar\omega}{k_B T}}\right) \sum_j k_j^{VT} n_j \mathcal{L}_j, \quad (6.5)$$

with k_j^{VT} being the de-excitation rate coefficient of the vibrations $N_2(v = 1)$ with j th species (see Table 6.1)) and \mathcal{L}_j the Losev correction factor (Capitelli *et al.*, 2000) that takes into account the dependence of Q_{VT} on the vibrational temperature and the anharmonicity of the N_2 potential. However, we will set $\mathcal{L}_j = 1$ since the correction in Q_{VT} due to these effects is negligible compared to the weight of the translational temperature in the vibrational-translational time scale.

A nitrogen molecule can be excited vibrationally ($v \rightarrow v'$, $v' > v$) by electron impact. This excitation requires a quantum of energy $\hbar\omega$. The energy is not indefinitely stored in the first level but can be exchanged through the vibrational-vibrational (VV) reaction



populating higher vibrational levels. However, due to anharmonicity effects (unequal energy spacing between vibrational levels) part of the quantum energy is lost to translational energy degrees of freedom. The rate of vibrational (translational) energy loss (gain) associated with VV exchange is denoted by Q_{VV} . Nonetheless, this is a minor effect compared to the mechanism associated with Q_{VT} . In this work, we will not consider this contribution.

The strong vibrational-translational non-equilibrium, i.e. $T_V \gg T$, increases the dissociation rate of N_2 molecules (see section A.2 in the Appendix) and therefore the density of vibrationally excited nitrogen molecules in the dissociation level $v = v_{max}$. The dissociation of N_2 molecules removes $2Q_D$ from the vibrational energy pool where $Q_D = \mathcal{E}_{N_2}^D S_D$, S_D is the net dissociation rate of reactions R_{81-85} and R_{96} , and $\mathcal{E}_{N_2}^D = 9.76$ K is the energy loss per dissociation act. The factor two in the energy rate removal comes from anharmonicity effects (Marrone and Treanor, 1963).

6. STEPPING MECHANISM IN HUMID AIR

Species	$k_j^{VT} \text{ (cm}^3 \text{s}^{-1}\text{)}$	Reference
N_2, O_2, NO	$6.4 \times 10^{-12} \exp(-137/T^{\frac{1}{3}})$	(<i>da Silva and Pasko, 2013</i>)
H_2O	$2.06 \times 10^{-11} \exp(-54.3/T^{\frac{1}{3}})$	(<i>Popov, 2016</i>)
N, O	$2.3 \times 10^{-13} \exp(-\frac{1280}{T}) + 2.7 \times 10^{-11} \exp(-\frac{10840}{T})$	(<i>Capitelli et al., 2000</i>)

Table 6.1: De-excitation rate coefficients of $N_2(v = 1)$ with the j th species.

Moving on to the initial conditions, our streamer channel consists of a pre-ionized neutral plasma with a depleted density around the center that mimics the space stem precursor of chapter 4 and is given by:

$$n_e = n_{e0} \exp\left(-\frac{r^2}{\sigma^2}\right) \left[1 - d \exp\left(-\frac{\left(z - \frac{L}{2}\right)^2}{\sigma_d^2}\right) \right], \quad (6.7)$$

where $n_{e0} = 2 \times 10^{20} \text{ m}^{-3}$ is the peak electron density, $d = 0.5$ is the depletion depth, $\sigma_d = 3 \text{ mm}$ is the depletion width and $\sigma = 0.3 \text{ mm}$ is the radial e-folding length (*da Silva and Pasko, 2013*).

Following the work by *Popov (2003)*; *da Silva and Pasko (2013)* we will use a driven-current approach so that the axial electric field is

$$E_z = E_{Ohm} - \frac{\partial \phi}{\partial z}, \quad (6.8)$$

where E_{Ohm} is calculated from the current I through Ohm's law (*Popov, 2003*)

$$E_{Ohm} = \frac{I}{\int_0^\infty \sigma(r) 2\pi r dr}, \quad (6.9)$$

and ϕ is the electrostatic potential created by space charges in the domain with homogeneous Dirichlet boundary conditions at $z = 0$ and $z = L$ and free boundary conditions at the outer radial boundary following the method of chapter 3. The actual size of the computational domain of our simulations is $2 \text{ cm} \times 0.3 \text{ cm}$. We set a current $I = 1 \text{ A}$ (*da Silva and Pasko, 2013*) and we vary the water content: from 0%, passing by 1.5% and till 3% of absolute humidity at STP.

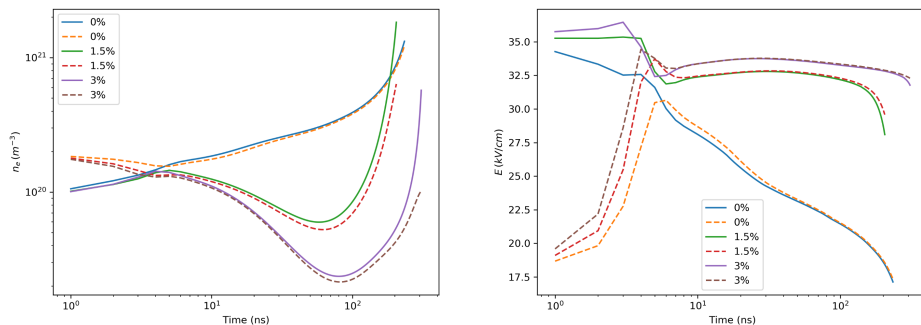


Figure 6.2: Evolution of the electron density (left panel) and electric field (right panel) at the space stem (solid lines) and far from it (dashed lines) under different humidity conditions. For humid air, the inhomogeneity is preserved and enhanced.

6.3 Results and discussion

Figure 6.2 shows the evolution of the electron density and the electric field for a point in the space stem region (solid lines) and far from it (dashed lines) in dry and humid air with a water content of 1.5% and 3%.

The first thing to notice is that the electron density experiences an inversion, i.e., the electron density at the space stem initially lower, surpasses the electron density outside of it. This is something that we expect in a constant drive-current approach: initially, those regions with a lower electron density are exposed to a higher electric field, in fact, above the breakdown value, which leads to a higher ionization rate.

After this quick ionization process that takes less than 10 ns, the electric field at the space stem decreases. In dry air, the subsequent electric field is above the breakdown value and the electron density increases. This is not the case for humid air, in which the electric field drops below breakdown leading to further electron depletion.

Nevertheless, in humid air, the electric field is significantly higher than in dry air. The main consequence is a more profuse production of O^- ions and atomic oxygen through the

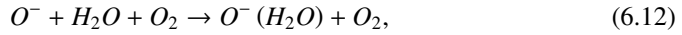
dissociative attachment reaction



In dry air, O^- quickly serves as the main source of electrons in the detachment reaction



However, in humid air, water molecules clusterize around O^- in the reaction



preventing an early detachment through reaction 6.11. As a result, (see fig. 6.2) in humid air, the inhomogeneity is preserved while it is removed in dry air. This also manifests in the evolution of the gas temperature (see Fig.6.3): the space stem heats up to significantly higher temperatures than the rest of the channel.

In humid air, an enhanced electric field is sustained around 100 ns, readily producing O^- ions and O atoms. Electron detachment through reaction 6.11 is the main mechanism supplying electrons back to the streamer channel once these two species become sufficiently abundant. Note that the electron density and temperature increase more abruptly in humid air than in dry air, due to this higher abundance.

6.4 Conclusions

In this chapter we have studied the evolution of a space stem precursor in a driven-current approach in dry and humid air. Under moderate electric fields, results show that water plays a role in preserving and enhancing electron inhomogeneities in the streamer channel as opposed to dry air, where they tend to dilute due to electron detachment processes.

As it has been discussed, space stems mediate the stepping propagation of negative leaders. Stepping has also been observed in positive leaders, but a clear sign of space stems is still absent. Our preliminary results and the experiments by *Kostinskiy et al.* (2018) highlight the relevance of water in the stepping mechanism.

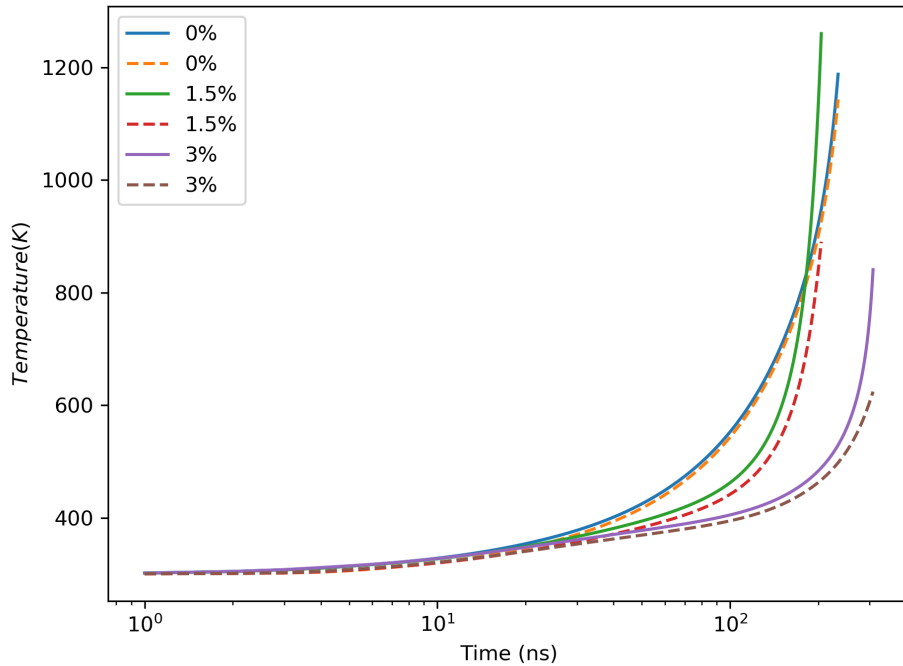


Figure 6.3: Evolution of the gas temperature at the space stem (solid lines) and far from it (dashed lines) for different content of water in air. In humid air, the space stem heats significantly faster increase of temperature is more abrupt than in dry air.

In chapter 3 we discussed the emergence of space stem precursors in streamer coronas at a smaller distance from the leader tip for positive polarity. As we argued, the attachment instability is favored by sufficiently high inner electric fields in the streamer channel, a condition that is more easily fulfilled in negative streamers. In humid air, clustering processes, enhanced attachment and electron-ion recombination lead to a more prominent electron depletion that turns into a high inner electric field in the streamer channel. These conditions are more suitable to produce space stem precursors in the streamer corona of positive leaders, away from the leader tip and therefore, easier to resolve in observations.

6. STEPPING MECHANISM IN HUMID AIR

Chapter 7

Summary and conclusions

7.1 Summary

Negative leaders in long spark discharges ($\gtrsim 2$ m) propagate in a stepped fashion, meaning that they suddenly jump after standing still for a few tens of microseconds. This propagation is mediated by the so-called space stem, an isolated, bright and warm plasma segment inside the streamer corona ahead of the leader. The space stem shoots counter-propagating streamers that pave the path for its bidirectional propagation until it connects to the main leader channel. In this way, the negatively charged end of the space stem becomes the new leader tip and a step is completed. Despite its relevance, the mechanism underlying the space stem onset remains elusive.

The sequence of events described above mostly comes from observations from natural lightning and artificial discharges. However, these observations are still far from resolving the smallest space and time scales that could shed some light on the formation of the space stem. At this point, numerical simulations turn out to be relevant. They allow us to study electric discharges in a controlled environment impossible to achieve in a laboratory.

To study the propagation of leader discharges we have developed a numerical model that couples the transport of charged species and their electrostatic interactions and gas expansion and heating. This model has been built on top of CLAWPACK, a library that implements Finite Volume Methods. Besides, long electric discharges involve widely separated scales that on uniform grids call for scalable models. In order to address this issue,

7. SUMMARY AND CONCLUSIONS

our model is based on the MPI framework.

State-of-the-art numerical models seek the efficient solution of the equations at hand. Our model is built upon a uniform grid. In these cases, solving Poisson's equation becomes a very time consuming task. To address this issue, we implemented a method that allows us to encapsulate the discharge in a narrow computational domain, halving the computing time. We have also applied this method to speed-up of the photoionization term. This method and the test simulations are presented in chapter 3 and published in *Malagón-Romero and Luque (2018)*.

Our model is scalable, meaning that it is able to run in thousands of computing cores. Taking advantage of this, we requested access to MareNostrum 4 and Picasso, supercomputers belonging to Red Española de Supercomputación (RES), where we have run most of the simulations presented in this thesis.

The first of our simulations was run in MareNostrum 4. We studied the propagation of a negative streamer emerging from the leader tip. We tested our hypothesis, whether an attachment instability is a feasible mechanism to explain the onset of space stem precursors. Our results showed that the space stem emerges in the streamer wake close to the non-uniform electric field adjacent to the leader tip. This non-uniform electric field causes a narrowing of the streamer channel that enhances the electric field triggering the attachment instability locally and leading to a locally warmer plasma inhomogeneity. However, after around 100 ns, the heating in the space stem stalls. As we argue in chapter 4, this is due to the drop of the electric current in the streamer channel. We then propose mechanisms to maintain this conductivity such as ionization waves or new streamer bursts emerging from the space stem. All the results and discussion about this topic are presented in chapter 4 and published in *Malagón-Romero and Luque (2019)*.

Experiments show counter-propagating streamers emerging from pilot-systems. In the literature, this is pointed out as a mechanism that promotes the heating in the space stem. Similar phenomenology is observed in high-altitude electric discharges known as sprites that develop structures known as glows that shoot counter-propagating streamers. Our next step was to understand how the charge is distributed in these structures so they can launch these streamers. To do that we used a 3D streamer model (AFIVO) and we simulated pre-ionized sprite streamer channels. We observed that glows emerge due to an attachment instability triggered in the upper region of the channel (above 70 km). This attachment instability leads to accumulation of negative charge in the lower boundary of the glow. Once the electric field in this region is high enough, numerous negative streamers are shot upwards. This is essentially the mechanism underlying the carrot-sprite structure. These results are discussed in chapter 5 and published in *Malagón-Romero et al. (2020)*.

Unlike negative leaders, positive leaders mostly propagate in a continuous fashion. Recently, experiments showed positive stepped propagation and possible signatures of space stems in highly humid environment. We then moved to study the influence of water molecules in the stepping mechanism. We know that current has to flow through the space stem to heat it up to several thousand degrees. Then, we assumed a constant current flowing through a pre-ionized streamer channel with a plasma inhomogeneity embedded in its center mimicking the space stem. We carried out simulations in dry air and humid air at different water concentrations. Our results show that under the same current, the inhomogeneity is wiped out in dry air while it is enhanced in humid air. This is mostly due to the clusterization of water molecules around O^- and O_2^- ions, that prevents the electron detachment, the main mechanism feeding the streamer wake with electrons after the streamer head passage. This topic is presented in chapter 6 and we are working to publish the results.

7.2 Conclusions

In this thesis we have investigated the propagation of leader channels in lightning and long spark discharges using our in-house electro-hydrodynamic code. These are the main conclusions from this work:

- **Chapter 3:** The performance of Poisson's solvers based on uniform grids depends on the computational domain size. Elongated discharges such as leader and streamers are suitable for narrow domains. The method that we propose, allows to tightly wrap the computational domain to the discharge, halving the computing time of the simulation for the test cases that we explored.
- **Chapter 4:** Space stems are one of the most enigmatic elements in the streamer-to-leader transition. They are readily produced in the advance of negative leaders in virgin air. The results of the numerical model described in Chapter 2 show that the propagation of streamer channels in highly non-homogeneous leader-like electric field environments lead to narrow regions in its wake where the attachment instability is triggered depleting electrons and leading to plasma inhomogeneities that resemble space stems. This confirms the attachment instability as a feasible mechanism for the onset of space stems.
- **Chapter 5:** Pilot system structures as shown in *Kochetov et al. (2011)* shoot counter-propagating streamers. These streamers are believed to heat the space stem to become a space leader. A similar phenomenology has been observed in sprite glows. Our results show how an attachment instability leads to a charge distribution that enables sprite glows to shoot counter-propagating streamers. This mechanism explains the well-known morphology of carrot sprites.
- **Chapter 6:** Space stems emerge in the streamer wake due to the action of an attachment instability in highly non-uniform electric fields and the charge distribution enables them to shoot counter-propagating streamers. These streamers force a current through the space stem. For the first time we show how the space stem develops in a forced-current approach in dry and humid air. Our results point out to the relevance of water vapor chemistry in the study of the space stem precursors. Water molecules prevent electron detachment by clustering around negative ions. As a result, electron inhomogeneities such as space stem precursors are enhanced in humid air.

Chapter 8

Future Work

8.1 Future Work

Using the model described in chapter 2 we have carried out two different kinds of simulations: 1) simulations where we consistently studied the evolution of the conductivity in a advancing streamer channel emerging from a leader-like tip (see chapters 4) and 2) simulations where we imposed a constant current in a pre-ionized streamer-like channel (see chapter 6).

Both types of simulations contributed to study the evolution of the conductivity in the streamer channel for different time scales. However, consistently following the microphysics of a propagating streamer channel is computationally challenging, not to mention the present unfeasibility to simulate the microphysics of a streamer corona. An alternative are the so-called tree-models (*Luque and Ebert, 2014*), where streamers are modeled as macroscopic channels with a velocity, radius, conductivity and branching probability. These models require some improvements such as time-dependent resistance. This resistance varies due to the balance of attachment and detachment processes that we have seen are the key to describe the formation and evolution of space stems.

The results obtained in this thesis provide a time evolution of single streamer channels, which can be used as an input for tree-models. Our next step is to couple the leader model with a circuit model for a streamer corona based on *Luque and Ebert (2014)* with the improvements mentioned above. The coupling of the streamer-corona model to the leader

8. FUTURE WORK

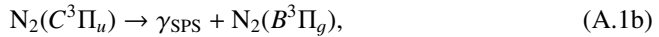
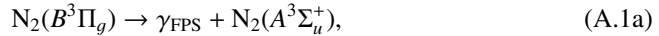
model takes place through the exchange of charge at the anchor points filaments-leader, that is, the boundaries of the former leader model, the electrostatic interactions leader-corona and the joule heating of air due to the current within the filaments.

Appendix A

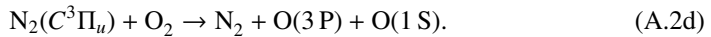
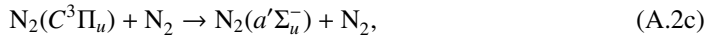
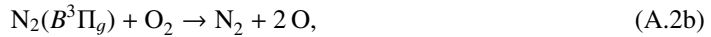
Chemical models

A.1 Light Emissions

Our discharge develops in a high pressure regime (atmospheric pressure), therefore the dynamics of the charged species is heavily dominated by collisions. A fraction of these collisions excites electronic states such as $N_2(B^3\Pi_g)$ and $N_2(C^3\Pi_u)$. These electronically excited states undergo radiative deactivation:



and produce emissions known as First Positive System (FPS)¹ and Second Positive System (SPS) respectively. These species can also be collisionally quenched:



In our code we used electron impact excitation rates for reactions (A.1) obtained from BOLSIG+ *Hagelaar and Pitchford* (2005) using the cross-section database *Phelps and*

¹Also denoted as 1PN2 in this thesis

Pitchford (1985). The reaction rates for the collisional quenching reactions (A.2) have been obtained from *Capitelli et al.* (2000).

A.2 Chemical model

Table A.1 lists all the chemical reactions considered in this chapter 6. This chemical model extends the model used by (*da Silva and Pasko, 2013; Liu and Becerra, 2017*), by adding water clusters around O^- and OH^- . These clusters turn out to be relevant by affecting the electron detachment time scale. The rates for reactions denoted as $f(E/N)$ indicate a dependence on the reduced electric field (E/N , with $N \equiv n_{air}$). These rates are calculated from Bolsig+ *Hagelaar and Pitchford* (2005), using the cross-section data from *Phelps and Pitchford* (1985) and *Itikawa* (2005), both retrieved from the Lxcat web (*Pancheshnyi et al., 2012*).

Now we move to explain the magnitudes appearing in table A.1. The electron temperature T_e as a function of the reduced electric field is given by

$$T_e = T + a_e \left(\frac{E/N}{1Td} \right)^{0.46}, \quad (\text{A.3})$$

where T is the background gas temperature and $a_e = 3648.6$ K (*Vidal et al., 2002*).

The ion temperature is calculated following *Benilov and Naidis* (2003) as

$$T_i = T + a_i \left(\frac{E/N}{1Td} \right)^2 \quad (\text{A.4})$$

being $a_i = 0.13$ K. The effective ion temperature T_{eff} is defined as (*Capitelli et al., 2000*)

$$T_{\text{eff}} = \frac{m_i T + m T_i}{m_i + m} \quad (\text{A.5})$$

where m_i and m are the masses of the colliding ion and neutral respectively.

A consequence of the vibrational-translational non-equilibrium is the acceleration of electron-impact processes due to super elastic collisions with $N_2(v = 1)$. We take into account this effect with a factor F following *Benilov and Naidis* (2003)

$$F = \exp \left[C \frac{\exp(-\hbar\omega/k_B T_v)}{(E/N)^2} \right] \quad (\text{A.6})$$

where k_B is the Boltzmann constant and $C = 6500 \text{ Td}^2$.

Another consequence of this non-equilibrium situation is the enhancement of the dissociation rate of N_2 . This effect is considered through the factor

$$Z(T, T_V) = \frac{1 - \exp(-\hbar\omega/k_B T_V)}{1 - \exp(-\hbar\omega/k_B T)} \exp\left(-\frac{\theta_D - \beta T}{T_m}\right), \quad (\text{A.7})$$

where $\theta_D = 113\,260 \text{ K}$ is the dissociation temperature of N_2 , $\beta = 3$ and $1/T_m = 1/T_V - 1/T$.

	Reaction	Rate (m³⁽ⁿ⁻¹⁾s⁻¹)	Reference
Electron impact ionization			
1	$e + O_2 \longrightarrow O_2^+ + 2e$	$f(x_0)$	Bolsig+
2	$e + N_2 \longrightarrow N_2^+ + 2e$	$f(x_0)$	Bolsig+
3	$e + NO \longrightarrow NO^+ + 2e$	$F \times 5 \times 10^{-15} \times \exp\left(-\frac{460}{E/N}\right)$	34
4	$e + O \longrightarrow O^+ + 2e$	$F \times 4 \times 10^{-15} \times \exp\left(-\frac{713}{E/N}\right)$	34
5	$e + H_2O \longrightarrow H_2O^+ + 2e$	$f(x_0)$	Bolsig+
Associative ionization ionization			
6	$N + O \longrightarrow NO^+ + e$	$1.5 \times 10^{-21} \times T \times \exp\left(\frac{-32000}{T}\right)$	34
7	$N_2(A) + N_2(a') \longrightarrow N_4^+ + e$	5×10^{-17}	34
8	$N_2(a') + N_2(a') \longrightarrow N_4^+ + e$	2×10^{-16}	34
Dissociative attachment			
9	$e + O_2 \longrightarrow O + O^-$	$f(x_0)$	Bolsig+
10	$e + H_2O \longrightarrow OH^- + H$	$f(x_0)$	Bolsig+
11	$e + H_2O \longrightarrow O^- + H_2$	$f(x_0)$	Bolsig+
12	$e + H_2O \longrightarrow H^- + OH$	$f(x_0)$	Bolsig+
3-body attachment			
13	$e + O_2 + O_2 \longrightarrow O_2^- + O_2$	$f(x_0)$	Bolsig+
14	$e + O_2 + N_2 \longrightarrow O_2^- + N_2$	$1.07 \times 10^{-43} \times \frac{\exp(1500 \times (1/T - 1/T_e))}{(T_e/300)^2 \times \exp(70/T)}$	34
15	$e + O_2 + O \longrightarrow O_2^- + O$	1×10^{-43}	81
16	$e + O_2 + H_2O \longrightarrow O_2^- + H_2O$	$f(x_0)$	Bolsig+
Electron-ion recombination			
17	$e + O_2^+ \longrightarrow O + O(1D)$	$2 \times 10^{-13} \times \left(\frac{300}{T_e}\right)$	34
18	$e + NO^+ \longrightarrow O + N(2D)$	$4 \times 10^{-13} \times \left(\frac{300}{T_e}\right)^{1.5}$	34
19	$e + O_4^+ \longrightarrow O_2 + O_2$	$1.4 \times 10^{-12} \times \left(\frac{300}{T_e}\right)^{0.5}$	34
20	$e + N_2O_2^+ \longrightarrow N_2 + O_2$	$1.3 \times 10^{-12} \times \left(\frac{300}{T_e}\right)^{0.5}$	34
21	$e + O_2^+ + M \longrightarrow O_2 + M$	$6 \times 10^{-39} \times \left(\frac{300}{T_e}\right)^{1.5}$	34
22	$e + N_2^+ \longrightarrow N + N(2D)$	$2 \times 10^{-13} \times \left(\frac{300}{T_e}\right)^{0.5}$	81
23	$e + N_4^+ \longrightarrow N_2 + N_2(C)$	$2 \times 10^{-12} \times \left(\frac{300}{T_e}\right)^{0.5}$	81
25	$e + O_2^+ \cdot (H_2O) \longrightarrow O_2 + H_2O$	$2 \times 10^{-12} \times \left(\frac{300}{T_e}\right)^{0.5}$	81
25	$e + H_2O^+ \longrightarrow OH + H$	$3.15 \times 10^{-13} \times \left(\frac{300}{T_e}\right)^{0.8}$	81
26	$e + H_3O^+ \longrightarrow H_2O + H$	$3.15 \times 10^{-13} \times \left(\frac{300}{T_e}\right)^{0.5}$	81
27	$e + H_3O^+ \cdot (H_2O) \longrightarrow 2H_2O + H$	$2.5 \times 10^{-12} \times \left(\frac{300}{T_e}\right)^{0.5}$	81
28	$e + H_3O^+ \cdot (H_2O)_2 \longrightarrow 3H_2O + H$	$4.5 \times 10^{-12} \times \left(\frac{300}{T_e}\right)^{0.5}$	81
29	$e + H_3O^+ \cdot (H_2O)_3 \longrightarrow H + 4H_2O$	$6.5 \times 10^{-12} \times \left(\frac{300}{T_e}\right)^{0.5}$	1

Electron detachment

30	$O^- + N_2 \longrightarrow N_2O + e$	$1.16 \times 10^{-18} \times \exp\left(-\left(\frac{48.9}{11+E/N}\right)^2\right)$	116
31	$O^- + O \longrightarrow O_2 + e$	5×10^{-16}	34
32	$O^- + N_2(A) \longrightarrow O + N_2 + e$	2.2×10^{-15}	34
33	$O^- + O_2(a) \longrightarrow O_3 + e$	3×10^{-16}	34
34	$O^- + NO \longrightarrow NO_2 + e$	2.6×10^{-16}	34
35	$O_2^- + O \longrightarrow O_3 + e$	1.5×10^{-16}	34
36	$O_2^- + N_2(A) \longrightarrow O_2 + N_2 + e$	2.1×10^{-15}	34
37	$O_2^- + O_2(a) \longrightarrow 2O_2 + e$	2×10^{-16}	34
38	$M + O_2^- \longrightarrow e + O_2 + M$	$1.24 \times 10^{-17} \times \exp\left(-\left(\frac{179}{8.8+E/N}\right)^2\right)$	116
39	$O_3^- + O \longrightarrow 2O_2 + e$	3×10^{-16}	34
40	$O^- + N \longrightarrow NO + e$	2.6×10^{-16}	28
41	$O^- + O_2(b) \longrightarrow O + O_2 + e$	6.9×10^{-16}	28
42	$O^- + N_2(B) \longrightarrow O + N_2 + e$	1.9×10^{-15}	28
43	$O_2^- + O_2(b) \longrightarrow 2O_2 + e$	3.6×10^{-16}	28
44	$O_2^- + N_2(B) \longrightarrow N_2 + O_2 + e$	2.5×10^{-15}	28
45	$H^- + H \longrightarrow H_2 + e$	2×10^{-15}	81
46	$H^- + O_2 \longrightarrow HO_2 + e$	1.2×10^{-15}	81
47	$OH^- + H \longrightarrow e + H_2O$	1.4×10^{-15}	81
48	$OH^- + O \longrightarrow HO_2 + e$	2×10^{-16}	49

Electron impact excitation of metastables

49	$e + N_2 \longrightarrow e + N_2(A)$	$f(x_0)$	Bolsig+
50	$e + N_2 \longrightarrow e + N_2(B)$	$f(x_0)$	Bolsig+
51	$e + N_2 \longrightarrow e + N_2(a)$	$f(x_0)$	Bolsig+
52	$e + N_2 \longrightarrow e + N_2(C)$	$f(x_0)$	Bolsig+
53	$e + O_2 \longrightarrow e + O_2(a)$	$f(x_0)$	Bolsig+
54	$e + O_2 \longrightarrow e + O_2(b)$	$f(x_0)$	Bolsig+

Electron impact dissociation

55	$e + N_2 \longrightarrow N + N(2D) + e$	$f(x_0)$	Bolsig+
56	$e + O_2 \longrightarrow O + O + e$	$f(x_0)$	Bolsig+
57	$e + O_2 \longrightarrow O + O(1D) + e$	$f(x_0)$	Bolsig+
58	$e + O_2 \longrightarrow O + O(1S) + e$	$f(x_0)$	Bolsig+
231	$e + H_2O \longrightarrow H + OH + e$	$f(x_0)$	81
232	$e + H_2O \longrightarrow H_2 + O + e$	$f(x_0)$	81

Radiative deactivation of metastables, optical emission

59	$N_2(C) \longrightarrow N_2(B) + h\nu_{2PN2}$	2.47×10^7	28
----	---	--------------------	----

60	$N_2(B) \longrightarrow N_2(A) + h\nu_{1PN_2}$	1.34×10^5	28
Collisional quenching of metastables			
61	$N_2(A) + O_2 \longrightarrow N_2 + O + O$	2.54×10^{-18}	34
62	$N_2(A) + O_2 \longrightarrow N_2 + O_2(b)$	7.5×10^{-19}	34
63	$N_2(A) + O \longrightarrow N_2 + O(1S)$	3×10^{-17}	34
64	$N_2(A) + O \longrightarrow NO + N(2D)$	7×10^{-18}	34
65	$N_2(A) + N_2(A) \longrightarrow N_2(B) + N_2$	7.7×10^{-17}	34
66	$N_2(A) + N_2(A) \longrightarrow N_2(C) + N_2$	1.6×10^{-16}	34
67	$N_2(B) + N_2 \longrightarrow 2N_2$	2×10^{-18}	28
68	$N_2(B) + O_2 \longrightarrow N_2 + 2O$	3×10^{-16}	28
69	$N_2(B) + N_2 \longrightarrow N_2(A) + N_2$	1×10^{-17}	34
70	$N_2(a') + O_2 \longrightarrow N_2 + O + O(1D)$	2.8×10^{-17}	34
71	$N_2(a') + N_2 \longrightarrow N_2(B) + N_2$	2×10^{-19}	34
72	$N_2(C) + O_2 \longrightarrow N_2 + O + O(1D)$	2.5×10^{-16}	34
73	$N_2(C) + O_2 \longrightarrow N_2 + O + O(1S)$	3×10^{-16}	28
74	$N_2(C) + O_2 \longrightarrow N_2 + O + O$	2.5×10^{-16}	130
75	$N_2(C) + N_2 \longrightarrow N_2(B) + N_2$	1×10^{-17}	34
76	$N_2(C) + N_2 \longrightarrow N_2(a') + N_2$	1×10^{-17}	34
77	$O(1D) + N_2 \longrightarrow O + N_2$	$1.8 \times 10^{-17} \times \exp\left(\frac{107}{T}\right)$	34
78	$O(1D) + O_2 \longrightarrow O + O_2(b)$	$2.56 \times 10^{-17} \times \exp\left(\frac{67}{T}\right)$	34
79	$O(1D) + O_2 \longrightarrow O + O_2$	$6.4 \times 10^{-18} \times \exp\left(\frac{67}{T}\right)$	34
80	$O(1D) + O_2 \longrightarrow O + O_2(a)$	1×10^{-18}	28
81	$O(1D) + O \longrightarrow 2O$	8×10^{-18}	28
82	$O(1D) + N_2O \longrightarrow NO + NO$	7.2×10^{-17}	81
83	$O(1D) + N_2O \longrightarrow N_2 + O_2$	4.4×10^{-17}	81
84	$O(1S) + O \longrightarrow O(1D) + O(1D)$	$5 \times 10^{-17} \times \exp\left(\frac{-301}{T}\right)$	34
85	$O(1S) + O_2 \longrightarrow O(1D) + O_2$	$1.3 \times 10^{-18} \times \exp\left(\frac{-850}{T}\right)$	34
86	$N(2D) + O_2 \longrightarrow NO + O$	$1.5 \times 10^{-18} \times \left(\frac{300}{T}\right)^{-0.5}$	34
87	$N(2D) + O_2 \longrightarrow NO + O(1D)$	$6 \times 10^{-18} \times \left(\frac{300}{T}\right)^{-0.5}$	34
88	$N(2D) + N_2 \longrightarrow N + N_2$	6×10^{-21}	34
89	$N(2D) + O \longrightarrow N + O(1D)$	4×10^{-19}	28
90	$O_2(a) + O_2 \longrightarrow O_2 + O_2$	$2.2 \times 10^{-24} \times \left(\frac{300}{T}\right)^{-0.8}$	34
91	$O_2(a) + O \longrightarrow O_2 + O$	$7 \times 10^{-22} \times \left(\frac{300}{T}\right)^{-0.5}$	81
92	$O_2(b) + O_2 \longrightarrow O_2(a) + O_2$	4.1×10^{-23}	81
93	$O_2(b) + N_2 \longrightarrow O_2(a) + N_2$	2.1×10^{-21}	81
94	$O_2(b) + O \longrightarrow O_2(a) + O$	$8 \times 10^{-20} \times \left(\frac{300}{T}\right)^{-0.5}$	81

95	$O_2(b) + O \longrightarrow O_2 + O(1D)$	$3.4 \times 10^{-17} \times \left(\frac{300}{T}\right)^{0.1} \times \exp\left(-\frac{4200}{T}\right)$	28
100	$N_2(A) + H \longrightarrow N_2 + H$	2.1×10^{-16}	81
101	$N_2(A) + OH \longrightarrow N_2 + OH$	1×10^{-16}	81
102	$N_2(A) + H_2O \longrightarrow N_2 + H + OH$	5×10^{-20}	81
103	$N_2(a') + H_2O \longrightarrow N_2 + H + OH$	3×10^{-16}	81
104	$O(1D) + H_2 \longrightarrow H + OH$	1.1×10^{-16}	81
105	$O(1D) + H_2O \longrightarrow 2OH$	2.2×10^{-16}	81
106	$O(1D) + H_2O \longrightarrow H_2 + O_2$	3.57×10^{-16}	81
107	$O(1D) + H_2O_2 \longrightarrow H_2O + O_2$	5.2×10^{-16}	81
108	$O(1S) + H_2O \longrightarrow O + H_2O$	3×10^{-16}	81
109	$O(1S) + H_2O \longrightarrow OH + OH$	5×10^{-16}	81
110	$O(1S) + H_2O \longrightarrow H_2 + O_2$	5×10^{-16}	81
111	$O_2(b) + H_2O \longrightarrow O_2 + H_2O$	4.6×10^{-18}	81

Thermal dissociation and recombination

112	$N_2 + N_2 \longrightarrow 2N + N_2$	$Z \times 5 \times 10^{-14} \times \exp\left(-\frac{113200}{T}\right) \left(1 - \exp\left(-\frac{3354}{T}\right)\right)$	34
113	$N_2 + O_2 \longrightarrow 2N + O_2$	$Z \times 5 \times 10^{-14} \times \exp\left(-\frac{113200}{T}\right) \left(1 - \exp\left(-\frac{3354}{T}\right)\right)$	34
115	$N_2 + NO \longrightarrow 2N + NO$	$Z \times 5 \times 10^{-14} \times \exp\left(-\frac{113200}{T}\right) \left(1 - \exp\left(-\frac{3354}{T}\right)\right)$	34
115	$N_2 + O \longrightarrow 2N + O$	$Z \times 1.1 \times 10^{-13} \times \exp\left(-\frac{113200}{T}\right) \left(1 - \exp\left(-\frac{3354}{T}\right)\right)$	34
116	$N_2 + N \longrightarrow 2N + N$	$Z \times 1.1 \times 10^{-13} \times \exp\left(-\frac{113200}{T}\right) \left(1 - \exp\left(-\frac{3354}{T}\right)\right)$	34
117	$O_2 + O_2 \longrightarrow 2O + O_2$	$3.7 \times 10^{-14} \times \exp\left(-\frac{59380}{T}\right) \left(1 - \exp\left(-\frac{2240}{T}\right)\right)$	2
118	$O_2 + O \longrightarrow 3O$	$1.3 \times 10^{-13} \times \exp\left(-\frac{59380}{T}\right) \left(1 - \exp\left(-\frac{2240}{T}\right)\right)$	2
119	$O_2 + N \longrightarrow 2O + N$	$9.3 \times 10^{-15} \times \exp\left(-\frac{59380}{T}\right) \left(1 - \exp\left(-\frac{2240}{T}\right)\right)$	34
120	$O_2 + NO \longrightarrow 2O + NO$	$9.3 \times 10^{-15} \times \exp\left(-\frac{59380}{T}\right) \left(1 - \exp\left(-\frac{2240}{T}\right)\right)$	34
121	$O_2 + N_2 \longrightarrow 2O + N_2$	$9.3 \times 10^{-15} \times \exp\left(-\frac{59380}{T}\right) \left(1 - \exp\left(-\frac{2240}{T}\right)\right)$	34
122	$NO + N_2 \longrightarrow N + O + N_2$	$8.7 \times 10^{-15} \times \exp\left(\frac{-76000}{T}\right)$	34
123	$NO + O_2 \longrightarrow N + O + O_2$	$8.7 \times 10^{-15} \times \exp\left(\frac{-76000}{T}\right)$	34
124	$NO + O \longrightarrow N + O + O$	$1.7 \times 10^{-13} \times \exp\left(\frac{-76000}{T}\right)$	34
125	$NO + NO \longrightarrow N + O + NO$	$1.7 \times 10^{-13} \times \exp\left(\frac{-76000}{T}\right)$	34
126	$NO + N \longrightarrow N + O + N$	$1.7 \times 10^{-13} \times \exp\left(\frac{-76000}{T}\right)$	34
127	$N + N + M \longrightarrow N_2 + M$	$8.27 \times 10^{-46} \times \exp\left(\frac{500}{T}\right)$	34
128	$O + O + N_2 \longrightarrow O_2 + N_2$	$2.76 \times 10^{-46} \times \exp\left(\frac{720}{T}\right)$	34
129	$O + O + N \longrightarrow O_2 + N$	$2.76 \times 10^{-46} \times \exp\left(\frac{720}{T}\right)$	34
130	$O + O + NO \longrightarrow O_2 + NO$	$2.76 \times 10^{-46} \times \exp\left(\frac{720}{T}\right)$	34
131	$O + O + O_2 \longrightarrow O_2 + O_2$	$2.45 \times 10^{-43} \times T^{-0.63}$	34
132	$O + O + O \longrightarrow O_2 + O$	$8.8 \times 10^{-43} \times T^{-0.63}$	34

133	$N + O + M \longrightarrow NO + M$	$1.76 \times 10^{-43} \times T^{-0.5}$	34
134	$O_3 + O_3 \longrightarrow O_2 + O + O_3$	$7.16 \times 10^{-16} \times \exp\left(\frac{-11200}{T}\right)$	81
135	$O_2 + O + M \longrightarrow O_3 + M$	$6 \times 10^{-46} \times \left(\frac{300}{T}\right)^{2.6}$	
136	$OH + OH + N_2 \longrightarrow H_2O_2 + N_2$	$6.9 \times 10^{-43} \times \left(\frac{300}{T}\right)^{0.8}$	81
137	$OH + OH + O_2 \longrightarrow H_2O_2 + O_2$	$6.05 \times 10^{-43} \times \left(\frac{300}{T}\right)^3$	81
138	$OH + OH + H_2O \longrightarrow H_2O_2 + H_2O$	$1.54 \times 10^{-43} \times \left(\frac{300}{T}\right)^2 \times \exp\left(\frac{183.6}{T}\right)$	81
139	$O_2 + H + N_2 \longrightarrow HO_2 + N_2$	$5.94 \times 10^{-44} \times \left(\frac{300}{T}\right)$	81
140	$O_2 + H + O_2 \longrightarrow HO_2 + O_2$	$5.94 \times 10^{-44} \times \left(\frac{300}{T}\right)$	81
141	$OH + OH \longrightarrow H_2O_2$	2.6×10^{-17}	81
142	$OH + H + N_2 \longrightarrow H_2O + N_2$	$6.87 \times 10^{-43} \times \left(\frac{300}{T}\right)^2$	81
143	$OH + H + H_2O \longrightarrow H_2O + H_2O$	$4.38 \times 10^{-43} \times \left(\frac{300}{T}\right)^2$	81
Exchange of chemical bonds			
144	$O + N_2 \longrightarrow N + NO$	$1.3 \times 10^{-16} \times \exp\left(\frac{-38000}{T}\right)$	34
145	$N + O_2 \longrightarrow O + NO$	$1 \times 10^{-20} \times T \times \exp(-3150/T)$	34
146	$N + NO \longrightarrow O + N_2$	$1 \times 10^{-18} \times T^{0.5}$	34
147	$O + NO \longrightarrow N + O_2$	$2.5 \times 10^{-21} \times T \times \exp(-19\,500/T)$	34
148	$O + NO_2 \longrightarrow NO + O_2$	$5.5 \times 10^{-18} \times \exp\left(\frac{-187.9}{T}\right)$	81
149	$O_3 + NO \longrightarrow O_2 + NO_2$	$3.16 \times 10^{-18} \times \exp\left(\frac{1563}{T}\right)$	81
150	$OH + OH \longrightarrow H_2O + O$	$6.2 \times 10^{-20} \times \left(\frac{300}{T}\right)^{-2.6} \times \exp\left(\frac{945}{T}\right)$	81
151	$OH + HO_2 \longrightarrow H_2O + O_2$	$4.8 \times 10^{-17} \times \exp\left(\frac{250}{T}\right)$	81
152	$OH + O \longrightarrow H + O_2$	$2.4 \times 10^{-17} \times \exp\left(\frac{110}{T}\right)$	81
153	$HO_2 + HO_2 \longrightarrow H_2O_2 + O_2$	$2.2 \times 10^{-25} \times \exp\left(\frac{600.2}{T}\right)$	81
154	$HO_2 + NO \longrightarrow OH + NO_2$	$3.6 \times 10^{-18} \times \exp\left(\frac{269.4}{T}\right)$	81
155	$HO_2 + HO_2 + M \longrightarrow H_2O_2 + O_2 + M$	$1.9 \times 10^{-45} \times \exp\left(\frac{980}{T}\right)$	81
156	$H + HO_2 \longrightarrow H_2 + O_2$	$1.75 \times 10^{-16} \times \exp\left(\frac{-1030}{T}\right)$	81
157	$H + HO_2 \longrightarrow H_2O + O$	$5 \times 10^{-17} \times \exp\left(\frac{-866}{T}\right)$	81
158	$H + HO_2 \longrightarrow OH + OH$	$7.4 \times 10^{-16} \times \exp\left(\frac{-700}{T}\right)$	81
159	$O + HO_2 \longrightarrow OH + O_2$	$2.7 \times 10^{-17} \times \exp\left(\frac{224}{T}\right)$	81
160	$O_3 + H \longrightarrow OH + O_2$	$1.4 \times 10^{-16} \times \exp\left(\frac{-480}{T}\right)$	81
161	$O_3 + OH \longrightarrow O_2 + HO_2$	$1.7 \times 10^{-18} \times \exp\left(\frac{-940}{T}\right)$	81
Positive ion conversion			
162	$O_4^+ + O_2(a) \longrightarrow O_2^+ + 2O_2$	1×10^{-16}	34
163	$O_4^+ + O \longrightarrow O_2^+ + O_3$	3×10^{-16}	34
164	$O_2^+ + 2O_2 \longrightarrow O_4^+ + O_2$	$2.4 \times 10^{-42} \times \left(\frac{T_{eff}}{300}\right)^{-3.2}$	34
165	$N_2O_2^+ + O_2 \longrightarrow O_4^+ + N_2$	1×10^{-15}	34
166	$O_2^+ + 2N_2 \longrightarrow N_2O_2^+ + N_2$	$9 \times 10^{-43} \times \left(\frac{T_{eff}}{300}\right)^{-2}$	34

167	$O_4^+ + N_2 \longrightarrow N_2O_2^+ + O_2$	$4.61 \times 10^{-18} \times \left(\frac{T_{eff}}{300}\right)^{2.5} \times \exp\left(-\frac{2650}{T_{eff}}\right)$	34
168	$N_2O_2^+ + N_2 \longrightarrow O_2^+ + 2N_2$	$1.1 \times 10^{-12} \times \left(\frac{T_{eff}}{300}\right)^{-5.3} \times \exp\left(-\frac{2357}{T_{eff}}\right)$	34
169	$O_4^+ + O_2 \longrightarrow O_2^+ + 2O_2$	$3.3 \times 10^{-12} \times \left(\frac{T_{eff}}{300}\right)^{-4} \times \exp\left(-\frac{5030}{T_{eff}}\right)$	34
170	$O_2^+ + N_2 \longrightarrow NO^+ + NO$	$1 \times 10^{-26} \times \left(\frac{T_{eff}}{300}\right)^{-2}$	81
171	$O_2^+ + N \longrightarrow NO^+ + O$	1.2×10^{-16}	34
172	$O_2^+ + NO \longrightarrow NO^+ + O_2$	4.4×10^{-16}	34
173	$O_4^+ + NO \longrightarrow NO^+ + 2O_2$	1×10^{-16}	34
174	$N_2^+ + N_2 + M \longrightarrow N_4^+ + M$	$5 \times 10^{-41} \times \left(\frac{300}{T_i}\right)^2$	1
175	$N_2^+ + O_2 \longrightarrow O_2^+ + N_2$	$6 \times 10^{-17} \times \left(\frac{T_{eff}}{300}\right)^{-0.5}$	81
176	$N_4^+ + N_2 \longrightarrow 2N_2 + N_2^+$	$2.1 \times 10^{-22} \times \left(\frac{T_{eff}}{300}\right)^{0.5}$	81
177	$N_4^+ + O_2 \longrightarrow 2N_2 + O_2^+$	$2.5 \times 10^{-16} \times \left(\frac{T_{eff}}{300}\right)^{0.5}$	81
178	$O^+ + O_2 \longrightarrow O_2^+ + O$	$2 \times 10^{-17} \times \left(\frac{T_{eff}}{300}\right)^{-0.4}$	81
179	$O^+ + N_2 \longrightarrow NO^+ + N$	$1.2 \times 10^{-18} \times \left(\frac{T_{eff}}{300}\right)^{-1}$	81
180	$O^+ + N_2 + O_2 \longrightarrow NO^+ + N + O_2$	$6 \times 10^{-41} \times \left(\frac{T_{eff}}{300}\right)^{-2}$	81
181	$O^+ + N_2 + N_2 \longrightarrow NO^+ + N + N_2$	$6 \times 10^{-41} \times \left(\frac{T_{eff}}{300}\right)^{-2}$	81

Negative ion conversion

182	$O^- + O_2(a) \longrightarrow O_2^- + O$	1×10^{-16}	34
183	$O_2^- + O \longrightarrow O_2 + O^-$	3.3×10^{-16}	34
184	$O_3^- + O \longrightarrow O_2^- + O_2$	3.2×10^{-16}	34
185	$O_2 + O^- + M \longrightarrow O_3^- + M$	$1.1 \times 10^{-42} \times \exp\left(-\left(\frac{E/N}{65}\right)^2\right)$	116
186	$O_2 + O^- \longrightarrow O_2^- + O$	$6.96 \times 10^{-17} \times \exp\left(-\left(\frac{198}{5.6+E/N}\right)^2\right)$	116
187	$H^- + H_2O \longrightarrow OH^- + H_2$	3.8×10^{-15}	81
188	$O^- + H_2O \longrightarrow OH^- + OH$	6×10^{-19}	45

2-body ion-ion recombination

189	$O^- + O_2^+ \longrightarrow O + O_2$	$2 \times 10^{-13} \times \left(\frac{300}{T_i}\right)^{0.5}$	34
190	$O_2^- + O_2^+ \longrightarrow O_2 + O_2$	$2 \times 10^{-13} \times \left(\frac{300}{T_i}\right)^{0.5}$	34
191	$O_3^- + O_2^+ \longrightarrow O_3 + O_2$	$2 \times 10^{-13} \times \left(\frac{300}{T_i}\right)^{0.5}$	34
192	$O^- + NO^+ \longrightarrow O + NO$	$2 \times 10^{-13} \times \left(\frac{300}{T_i}\right)^{0.5}$	34
193	$O_2^- + NO^+ \longrightarrow O_2 + NO$	$2 \times 10^{-13} \times \left(\frac{300}{T_i}\right)^{0.5}$	34
194	$O_3^- + NO^+ \longrightarrow O_3 + NO$	$2 \times 10^{-13} \times \left(\frac{300}{T_i}\right)^{0.5}$	34
195	$O^- + N_2^+ \longrightarrow O + N_2$	$2 \times 10^{-13} \times \left(\frac{300}{T_i}\right)^{0.5}$	74
196	$O^- + O^+ \longrightarrow O + O$	$2 \times 10^{-13} \times \left(\frac{300}{T_i}\right)^{0.5}$	74
197	$O_2^- + N_2^+ \longrightarrow O_2 + N_2$	$2 \times 10^{-13} \times \left(\frac{300}{T_i}\right)^{0.5}$	74
198	$O_2^- + O^+ \longrightarrow O_2 + O$	$2 \times 10^{-13} \times \left(\frac{300}{T_i}\right)^{0.5}$	74

199	$O_3^- + N_2^+ \longrightarrow O_3 + N_2$	$2 \times 10^{-13} \times \left(\frac{300}{T_i}\right)^{0.5}$	74
200	$O_3^- + O^+ \longrightarrow O_3 + O$	$2 \times 10^{-13} \times \left(\frac{300}{T_i}\right)^{0.5}$	74
201	$O^- + O_2^+ \longrightarrow 3O$	1×10^{-13}	34
202	$O^- + NO^+ \longrightarrow 2O + N$	1×10^{-13}	34
203	$O^- + O_4^+ \longrightarrow O + 2O_2$	1×10^{-13}	34
204	$O^- + N_2O_2^+ \longrightarrow O + O_2 + N_2$	1×10^{-13}	34
205	$O_2^- + O_2^+ \longrightarrow O_2 + 2O$	1×10^{-13}	34
206	$O_2^- + NO^+ \longrightarrow O_2 + O + N$	1×10^{-13}	34
207	$O_2^- + O_4^+ \longrightarrow 3O_2$	1×10^{-13}	34
208	$O_2^- + N_2O_2^+ \longrightarrow 2O_2 + N_2$	1×10^{-13}	34
209	$O_3^- + O_2^+ \longrightarrow O_3 + 2O$	1×10^{-13}	34
210	$O_3^- + NO^+ \longrightarrow O_3 + N + O$	1×10^{-13}	34
211	$O_3^- + O_4^+ \longrightarrow O_3 + 2O_2$	1×10^{-13}	34
212	$O_3^- + N_2O_2^+ \longrightarrow O_3 + O_2 + N_2$	1×10^{-13}	34
213	$O^- + N_2^+ \longrightarrow O + 2N$	1×10^{-13}	74
214	$O_2^- + N_2^+ \longrightarrow O_2 + 2N$	1×10^{-13}	74
215	$O_3^- + N_2^+ \longrightarrow O_3 + 2N$	1×10^{-13}	74
216	$O^- + N_4^+ \longrightarrow O + 2N_2$	1×10^{-13}	74
217	$O_2^- + N_4^+ \longrightarrow O_2 + 2N_2$	1×10^{-13}	74
218	$O_3^- + N_4^+ \longrightarrow O_3 + 2N_2$	1×10^{-13}	74
229	$A^+ + B^- \longrightarrow$	1×10^{-13}	74
3-body ion-ion recombination			
219	$O^- + O_2^+ + O_2 \longrightarrow O + O_2 + O_2$	$2 \times 10^{-37} \times \left(\frac{300}{T_i}\right)^{2.5}$	34
220	$O_2^- + O_2^+ + O_2 \longrightarrow O_2 + O_2 + O_2$	$2 \times 10^{-37} \times \left(\frac{300}{T_i}\right)^{2.5}$	34
221	$O^- + NO^+ + O_2 \longrightarrow O + NO + O_2$	$2 \times 10^{-37} \times \left(\frac{300}{T_i}\right)^{2.5}$	34
222	$O_2^- + NO^+ + O_2 \longrightarrow O_2 + NO + O_2$	$2 \times 10^{-37} \times \left(\frac{300}{T_i}\right)^{2.5}$	34
223	$O_2^- + O_4^+ + O_2 \longrightarrow 3O_2 + O_2$	$2 \times 10^{-37} \times \left(\frac{300}{T_i}\right)^{2.5}$	34
224	$O^- + O_2^+ + N_2 \longrightarrow O + O_2 + N_2$	$2 \times 10^{-37} \times \left(\frac{300}{T_i}\right)^{2.5}$	34
225	$O_2^- + O_2^+ + N_2 \longrightarrow O_2 + O_2 + N_2$	$2 \times 10^{-37} \times \left(\frac{300}{T_i}\right)^{2.5}$	34
226	$O^- + NO^+ + N_2 \longrightarrow O + NO + N_2$	$2 \times 10^{-37} \times \left(\frac{300}{T_i}\right)^{2.5}$	34
227	$O_2^- + NO^+ + N_2 \longrightarrow O_2 + NO + N_2$	$2 \times 10^{-37} \times \left(\frac{300}{T_i}\right)^{2.5}$	34
228	$O_2^- + O_4^+ + N_2 \longrightarrow 3O_2 + N_2$	$2 \times 10^{-37} \times \left(\frac{300}{T_i}\right)^{2.5}$	34
Water cluster ions			
233	$O_2^- + H_2O + M \longrightarrow O_2^- \cdot (H_2O) + M$	2.2×10^{-40}	50
234	$O_2^- \cdot (H_2O) + M \longrightarrow O_2^- + H_2O + M$	$5.5 \times 10^{-15} \times \exp\left(\frac{-1.28116 \times 10^{-19}}{k_B T_i}\right)$	50

235	$O_2^- \cdot (H_2O) + H_2O + M \longrightarrow O_2^- \cdot (H_2O)_2 + M$	5×10^{-40}	50
236	$O_2^- \cdot (H_2O)_2 + M \longrightarrow O_2^- \cdot (H_2O) + H_2O + M$	$1.25 \times 10^{-14} \times \exp\left(\frac{-5.80133 \times 10^{-20}}{k_B T_i}\right)$	50
237	$O_2^- \cdot (H_2O)_2 + H_2O + M \longrightarrow O_2^- \cdot (H_2O)_3 + M$	5×10^{-41}	50
238	$O_2^- \cdot (H_2O)_3 + M \longrightarrow O_2^- \cdot (H_2O)_2 + H_2O + M$	$1.25 \times 10^{-15} \times \exp\left(\frac{-4.48821 \times 10^{-20}}{k_B T_i}\right)$	50
239	$O_2^+ + H_2O + M \longrightarrow O_2^+ \cdot (H_2O) + M$	2.6×10^{-40}	1
240	$O_2^+ \cdot (H_2O) + H_2O \longrightarrow H_3O^+ + OH + O_2$	3×10^{-16}	1
230	$O_4^+ + H_2O \longrightarrow O_2^+ \cdot (H_2O) + O_2$	$1.5 \times 10^{-15} \times \left(\frac{300}{T}\right)^{-0.5}$	105
241	$H_3O^+ + H_2O + M \longrightarrow H_3O^+ \cdot (H_2O) + M$	3×10^{-39}	1
242	$H_3O^+ \cdot (H_2O) + H_2O + M \longrightarrow H_3O^+ \cdot (H_2O)_2 + M$	3×10^{-39}	1
243	$H_3O^+ \cdot (H_2O)_2 + H_2O + M \longrightarrow H_3O^+ \cdot (H_2O)_3 + M$	3×10^{-39}	1
244	$O^- + H_2O + O_2 \longrightarrow O^- \cdot (H_2O) + O_2$	1.3×10^{-40}	145
245	$O^- \cdot (H_2O) + H_2O \longrightarrow OH^- \cdot (H_2O) + OH$	1×10^{-17}	145
246	$OH^- + H_2O + O_2 \longrightarrow OH^- \cdot (H_2O) + O_2$	2×10^{-40}	8
247	$OH^- \cdot (H_2O) + O_2 \longrightarrow OH^- + H_2O + O_2$	$5 \times 10^{-15} \times \exp\left(\frac{-1.17416 \times 10^{-19}}{k_B T_i}\right)$	8
248	$OH^- \cdot (H_2O) + H_2O + O_2 \longrightarrow OH^- \cdot (H_2O)_2 + O_2$	3×10^{-40}	8
249	$OH^- \cdot (H_2O)_2 + O_2 \longrightarrow OH^- \cdot (H_2O) + H_2O + O_2$	$7.5 \times 10^{-15} \times \exp\left(\frac{-7.43403 \times 10^{-20}}{k_B T_i}\right)$	8
250	$OH^- \cdot (H_2O)_2 + H_2O + O_2 \longrightarrow OH^- \cdot (H_2O)_3 + O_2$	1×10^{-40}	8
251	$OH^- \cdot (H_2O)_3 + O_2 \longrightarrow OH^- \cdot (H_2O)_2 + H_2O + O_2$	$2.5 \times 10^{-15} \times \exp\left(\frac{-5.69711 \times 10^{-20}}{k_B T_i}\right)$	8
252	$OH^- \cdot (H_2O)_3 + H_2O + O_2 \longrightarrow OH^- \cdot (H_2O)_4 + O_2$	1×10^{-40}	8
253	$OH^- \cdot (H_2O)_4 + O_2 \longrightarrow OH^- \cdot (H_2O)_3 + H_2O + O_2$	$2.5 \times 10^{-15} \times \exp\left(\frac{-3.89071 \times 10^{-20}}{k_B T_i}\right)$	8
254	$OH^- \cdot (H_2O)_4 + H_2O + O_2 \longrightarrow OH^- \cdot (H_2O)_5 + O_2$	1×10^{-40}	8
255	$OH^- \cdot (H_2O)_5 + O_2 \longrightarrow OH^- \cdot (H_2O)_4 + H_2O + O_2$	$2.5 \times 10^{-15} \times \exp\left(\frac{-2.93193 \times 10^{-20}}{k_B T_i}\right)$	8

References

- ALEKSANDROV, N.L. & BAZELYAN, E.M. (1999). Ionization processes in spark discharge plasmas. *Plasma Sour. Sci. Technol.*, **8**, 285. 1, 13, 130, 135, 137
- ALEKSANDROV, N.L., BAZELYAN, E.M., KOCHETOV, I.V. & DYATKO, N.A. (1997). The ionization kinetics and electric field in the leader channel in long air gaps. *J. Phys. D*, **30**, 1616. 133
- ALGHAMDI, A., AHMADIA, A., KETCHESON, D.I., KNEPLEY, M.G., MANDLI, K.T. & DALCIN, L. (2011). Petclaw: A scalable parallel nonlinear wave propagation solver for python. In *Proceedings of the 19th High Performance Computing Symposia*, HPC '11, 96–103, Society for Computer Simulation International, San Diego, CA, USA. 48
- ANDERSON, C.R. (1986). A Method of Local Corrections for Computing the Velocity Field Due to a Distribution of Vortex Blobs. *Journal of Computational Physics*, **62**, 111–123. 51
- ANDERSON, C.R. (1989). Domain decomposition techniques and the solution of poisson's equation in infinite domains. In T. Chan, R. Glowinski, J. Périaux & O. Widlund, eds., *Domain Decomposition Methods*, Proceedings in Applied Mathematics, SIAM. 51
- ANDERSON, C.R. (2016). High order expanding domain methods for the solution of Poisson's equation in infinite domains. *Journal of Computational Physics*, **314**, 194–205. 51
- ARRAYÁS, M., EBERT, U. & HUNSDORFER, W. (2002). Spontaneous Branching of Anode-Directed Streamers between Planar Electrodes. *Phys. Rev. Lett.*, **88**, 174502. 72
- ARSHADI, M. & KEBARLE, P. (1970). Hydration of oh-and o2- in the gas phase. comparative solvation of oh-by water and the hydrogen halides. effects of acidity. *The Journal of Physical Chemistry*, **74**, 1483–1485. 137
- BABAeva, N.Y. & NAIDIS, G.V. (1996). Two-dimensional modelling of positive streamer dynamics in non-uniform electric fields in air. *J. Phys. D*, **29**, 2423. 50
- BABAeva, N.Y. & NAIDIS, G.V. (2000). Modeling of streamer propagation. In E.M. van Veldhuizen, ed., *Electrical discharges for environmental purposes: fundamentals and applications*, Nova Science, New York, United States. 50
- BABICH, L. & BOCHKOV, E. (2017). Numerical simulation of electric field enhancement at the contact of positive and negative streamers in relation to the problem of runaway electron generation in lightning and in long laboratory sparks. *J. Phys. D*, **50**, 455202. 94
- BABICH, L.P., BOCHKOV, E.I., KUTSYK, I.M., NEUBERT, T. & CHANRION, O. (2015). A model for electric field enhancement in lightning leader tips to levels allowing X-ray and γ ray emissions. *J. Geophys. Res. (Space Phys)*, **120**, 5087. 92, 94
- BAGHERI, B. & TEUNISSEN, J. (2019). The effect of the stochasticity of photoionization on 3d streamer simulations. *Plasma Sources Science and Technology*, **28**, 045013. 99, 100
- BALAY, S., ABHYANKAR, S., ADAMS, M.F., BROWN, J., BRUNE, P., BUSCHELMAN, K., DALCIN, L., EIJKHOUT, V., GROPP, W.D., KAUSHIK, D., KNEPLEY, M.G., MCINNES, L.C., RUPP, K., SMITH, B.F., ZAMPINI, S., ZHANG, H. & ZHANG, H. (2016a). PETSc users manual. Tech. Rep. ANL-95/11 - Revision 3.7, Argonne National Laboratory. 48, 62
- BALAY, S., ABHYANKAR, S., ADAMS, M.F., BROWN, J., BRUNE, P., BUSCHELMAN, K., DALCIN, L., EIJKHOUT, V., GROPP, W.D., KAUSHIK, D., KNEPLEY, M.G., MCINNES, L.C., RUPP, K., SMITH, B.F., ZAMPINI, S., ZHANG, H. & ZHANG, H. (2016b). PETSc Web page. <http://www.mcs.anl.gov/petsc>. 48, 62
- BALLS, G.T. & COLELLA, P. (2002). A Finite Difference Domain Decomposition Method Using Local Corrections for the Solution of Poisson's Equation. *Journal of Computational Physics*, **180**, 25–53. 51
- BÁRDOS, L. & BARÁNKOVÁ, H. (2010). Cold atmospheric plasma: Sources, processes, and applications. *Thin Solid Films*, **518**, 6705–6713. 1
- BAYLISS, A., GUNZBURGER, M. & TURKEL, E. (1982). Boundary conditions for the numerical solution of elliptic equations in exterior regions. *SIAM J. App. Math.*, **42**, 430–451. 51
- BAZELYAN, E. & RAIZER, Y. (2010). *Lightning Physics and Lightning Protection*. Institute of Physics Publishing, Bristol, UK. 77
- BAZELYAN, E.M. & RAIZER, Y.P. (1997). *Spark discharge*. CRC press. 5, 7, 8, 10, 13
- BENILOV, M.S. & NAIDIS, G.V. (2003). Modelling of low-current discharges in atmospheric-pressure air taking account of non-equilibrium effects. *J. Phys. D*, **36**, 1834. 128

REFERENCES

- BIAGI, C.J., UMAN, M.A., HILL, J.D., JORDAN, D.M., RAKOV, V.A. & DWYER, J. (2010). Observations of stepping mechanisms in a rocket-and-wire triggered lightning flash. *J. Geophys. Res. (Atmos.)*, **115**, D23215. 1, 2, 15, 77, 94, 111
- BIAGI, C.J., UMAN, M.A., HILL, J.D. & JORDAN, D.M. (2014). Negative leader step mechanisms observed in altitude triggered lightning. *J. Geophys. Res. (Atmos.)*, **119**, 8160. 3, 14, 76, 82, 111
- BÓR, J. (2013). Optically perceptible characteristics of sprites observed in Central Europe in 2007-2009. *J. Atm. Sol.-Terr. Phys.*, **92**, 151. 106, 107, 109
- BOURDON, A., PASKO, V.P., LIU, N.Y., CÉLESTIN, S., SÉGUR, P. & MARODE, E. (2007). Efficient models for photoionization produced by non-thermal gas discharges in air based on radiative transfer and the Helmholtz equations. *Plasma Sour. Sci. Technol.*, **16**, 656. 50, 73
- BRIELS, T.M.P., KOS, J., WINANDS, G.J.J., VAN VELDHUIZEN, E.M. & EBERT, U. (2008). Positive and negative streamers in ambient air: measuring diameter, velocity and dissipated energy. *J. Phys. D*, **41**, 234004. 11
- BRIGGS, M.S., XIONG, S., CONNAUGHTON, V., TIERNEY, D., FITZPATRICK, G., FOLEY, S., GROVE, J.E., CHEKHTMAN, A., GIBBY, M., FISHMAN, G.J., MCBREEN, S., CHAPLIN, V.L., GUIRIEC, S., LAYDEN, E., BHAT, P.N., HUGHES, M., GREINER, J., KIENLIN, A., KIPPEN, R.M., MEEGAN, C.A., PACIESAS, W.S., PREECE, R.D., WILSON-HODGE, C., HOLZWORTH, R.H. & HUTCHINS, M.L. (2013). Terrestrial gamma-ray flashes in the Fermi era: Improved observations and analysis methods. *J. Geophys. Res. (Space Phys)*, **118**, 3805. 75
- CAPITELLI, M., M., F.C., F., G.B. & I., O.A. (2000). *Plasma Kinetics in Atmospheric Gases*. Springer Verlag, Berlin, Germany. 7, 113, 115, 116, 128, 131, 132, 133
- CELESTIN, S., XU, W. & PASKO, V.P. (2012). Terrestrial gamma ray flashes with energies up to 100 MeV produced by nonequilibrium acceleration of electrons in lightning. *J. Geophys. Res. (Space Phys)*, **117**, A05315. 1
- CHERNYI, G. (2002). *Progress In Astronautics and Aeronautics: Physical and Chemical Processes In Gas Dynamics*, vol. 1. AIAA. 115
- CHRISTIAN, H.J., BLAKESLEE, R.J., BOCCIPPPIO, D.J., BOECK, W.L., BUECHLER, D.E., DRISCOLL, K.T., GOODMAN, S.J., HALL, J.M., KOSHAK, W.J., MACH, D.M. & STEWART, M.F. (2003). Global frequency and distribution of lightning as observed from space by the Optical Transient Detector. *J. Geophys. Res. (Atmos.)*, **108**, 4005. 1
- COORAY, V. (2003). Mechanism of electrical discharges. In V. Cooray, ed., *The Lightning Flash*, IEE Power Series, Institution of Engineering and Technology. 2, 10, 13, 76
- CUMMER, S.A., JAUGEY, N., LI, J., LYONS, W.A., NELSON, T.E. & GERKEN, E.A. (2006). Submillisecond imaging of sprite development and structure. *Geophys. Res. Lett.*, **33**, L04104. 97
- DA SILVA, C.L. & PASKO, V.P. (2013). Dynamics of streamer-to-leader transition at reduced air densities and its implications for propagation of lightning leaders and gigantic jets. *J. Geophys. Res. (Atmos.)*, **118**, 13. 7, 22, 23, 76, 78, 92, 113, 116, 128, 130, 131, 132, 133, 134, 135, 136
- DERKS, G., EBERT, U. & MEULENBROEK, B. (2008). Laplacian Instability of Planar Streamer Ionization Fronts—An Example of Pulled Front Analysis. *Journal of NonLinear Science*, **18**, 551. 72
- DOMENS, P., GIBERT, A., DUPUY, J. & HUTZLER, B. (1991). Propagation of the positive streamer-leader system in a 16.7 m rod-plane gap. *J. Phys. D*, **24**, 1748. 111
- DOUGLAS-HAMILTON, D.H. & MANI, S.A. (1973). An electron attachment plasma instability. *Appl. Phys. Lett.*, **23**, 508. 98, 105
- DOUGLAS-HAMILTON, D.H. & MANI, S.A. (1974). Attachment instability in an externally ionized discharge. *J. Appl. Phys.*, **45**, 4406. 15, 77, 98, 105
- DWYER, J.R. (2004). Implications of x-ray emission from lightning. *Geophys. Res. Lett.*, **31**, L12102. 1
- DWYER, J.R. & UMAN, M.A. (2014). The physics of lightning. *J. Geophys. Res.*, **534**, 147. 75, 77
- DWYER, J.R., RASSOUL, H.K., AL-DAYEH, M., CARAWAY, L., CHREST, A., WRIGHT, B., KOZAK, E., JERAULD, J., UMAN, M.A., RAKOV, V.A., JORDAN, D.M. & RAMBO, K.J. (2005). X-ray bursts associated with leader steps in cloud-to-ground lightning. *Geophys. Res. Lett.*, **32**, L01803. 75, 94
- DWYER, J.R., UMAN, M.A. & RASSOUL, H.K. (2009). Remote measurements of thundercloud electrostatic fields. *J. Geophys. Res. (Atmos.)*, **114**, D09208. 1
- EBERT, U., MONTJIN, C., BRIELS, T.M.P., HUNSDORFER, W., MEULENBROEK, B., ROCCO, A. & VAN VELDHUIZEN, E.M. (2006). The multiscale nature of streamers. *Plasma Sour. Sci. Technol.*, **15**, S118. 49
- EBERT, U., NIJDAM, S., LI, C., LUQUE, A., BRIELS, T. & VAN VELDHUIZEN, E. (2010). Review of recent results on streamer discharges and discussion of their relevance for sprites and lightning. *J. Geophys. Res. (Space Phys)*, **115**, A00E43. 76
- FEHSENFELD, F.C. & FERGUSON, E.E. (1974). Laboratory studies of negative ion reactions with atmospheric trace constituents. *J. Chem. Phys.*, **61**, 3181–3193. 135

- FISHMAN, G.J., BHAT, P.N., MALLOZZI, R., HORACK, J.M., KOSHUT, T., KOUVELIOTOU, C., PENDLETON, G.N., MEEGAN, C.A., WILSON, R.B., PACIESAS, W.S., GOODMAN, S.J. & CHRISTIAN, H.J. (1994). Discovery of Intense Gamma-Ray Flashes of Atmospheric Origin. *Science*, **264**, 1313. 1, 75
- FLITTI, A. & PANCHESHNYI, S. (2009). Gas heating in fast pulsed discharges in N₂-O₂ mixtures. *European Physical Journal Applied Physics*, **45**, 21001. 78, 79
- FRANZ, R.C., NEMZEK, R.J. & WINCKLER, J.R. (1990). Television Image of a Large Upward Electrical Discharge Above a Thunderstorm System. *Science*, **249**, 48. 97
- FRIDMAN, A. (2008). *Plasma chemistry*. Cambridge university press. 131
- GALLIMBERTI, I. (1979). The mechanism of the long spark formation. *Journal de Physique*, **40**, 193. 76, 78, 112, 136, 137
- GALLIMBERTI, I., BACCIEGA, G., BONDIU-CLEGERIE, A. & LANLANDE, P. (2002). Mécanismes physiques des décharges électriques sur de grands intervalles d'air. *Comptes Rendus Physique*, **3**, 1335. 13, 111
- GAMEROTA, W.R., IDONE, V.P., UMAN, M.A., NGIN, T., PILKEY, J.T. & JORDAN, D.M. (2014). Dart-stepped-leader step formation in triggered lightning. *Geophys. Res. Lett.*, **41**, 2204. 3, 76, 82, 111
- GAO, Y., CHEN, M., QIN, Z., QIU, Z., YANG, Y., DU, Y.P., WANG, S. & ZHANG, G. (2020). The Spatial Evolution of Upward Positive Stepped Leaders Initiated From a 356-m-Tall Tower in Southern China. *Journal of Geophysical Research (Atmospheres)*, **125**, e31508. 111
- GORIN, B.N., LEVITOV, V.I. & SHKILEV, A.V. (1976). Some principles of leader discharge of air gaps with a strong non-uniform field. *IEE Conf. Publ.*, **143**, 274–278. 3, 76, 111
- HAGELAAR, G.J.M. & PITCHFORD, L.C. (2005). Solving the Boltzmann equation to obtain electron transport coefficients and rate coefficients for fluid models. *Plasma Sour. Sci. Technol.*, **14**, 722. 114, 127, 128
- HEJLESEN, M.M., RASMUSSEN, J.T., CHATELAIN, P. & WALTHER, J.H. (2013). A high order solver for the unbounded Poisson equation. *Journal of Computational Physics*, **252**, 458–467. 51
- HILL, J.D., UMAN, M.A. & JORDAN, D.M. (2011). High-speed video observations of a lightning stepped leader. *J. Geophys. Res. (Atmos.)*, **116**, D16117. 3, 76, 82, 94, 111
- HU, W., CUMMER, S.A. & LYONS, W.A. (2007). Testing sprite initiation theory using lightning measurements and modeled electromagnetic fields. *J. Geophys. Res. (Atmos.)*, **112**, D13115. 100
- HUANG, S., CHEN, W., PEI, Z., FU, Z., WANG, L., HE, T., LI, Z., GU, J., BIAN, K., XIANG, N. & WANG, Y. (2020). The Discharge Preceding the Intense Reillumination in Positive Leader Steps Under the Slow Varying Ambient Electric Field. *Geophys. Res. Lett.*, **47**, e86183. 112
- IHADDADENE, M.A. & CELESTIN, S. (2015). Increase of the electric field in head-on collisions between negative and positive streamers. *Geophys. Res. Lett.*, **42**, 5644. 94
- ITIKAWA, Y. (2005). Cross Sections for Electron Collisions with Water Molecules. *J. Phys. Chem. Ref. Data*, **34**, 1. 128
- JACKSON, J. (1975). *Classical electrodynamics*. John Wiley and sons, New York, USA. 55, 58, 65, 67
- JAMES, R.A. (1977). The Solution of Poisson's Equation for Isolated Source Distributions. *Journal of Computational Physics*, **25**, 71–93. 51
- JIANG, R., QIE, X., ZHANG, H., LIU, M., SUN, Z., LU, G., WANG, Z. & WANG, Y. (2017). Channel branching and zigzagging in negative cloud-to-ground lightning. *Scientific Reports*, **7**, 3457. 111
- JIANG, R., QIE, X., LI, Z., ZHANG, H., LI, X., YUAN, S., LIU, M., SUN, Z., SRIVASTAVA, A., LIU, M., MA, Z. & LV, G. (2020). Luminous Crown Residual Vs. Bright Space Segment: Characteristic Structures for the Intermittent Positive and Negative Leaders of Triggered Lightning. *Geophys. Res. Lett.*, **47**, e88107. 112
- KIEU, N., GORDILLO-VÁZQUEZ, F.J., PASSAS, M., SÁNCHEZ, J., PÉREZ-INVERNÓN, F.J., LUQUE, A., MONTANYÁ, J. & CHRISTIAN, H. (2020). Submicrosecond Spectroscopy of Lightning-Like Discharges: Exploring New Time Regimes. *Geophys. Res. Lett.*, **47**, e88755. 13, 76
- KOCHETOV, I.V., NAPARTOVICH, A.P., VAGIN, N.P. & YURYSHV, N.N. (2011). Role of N
- 2
- molecules in pulse discharge production of I atoms for a pulsed chemical oxygen-iodine laser. *J. Phys. D*, **44**, 15204. 124
- KOCHKIN, P., LEHTINEN, N., VAN DEURSEN, A.P.J. & ØSTGAARD, N. (2016). Pilot system development in metre-scale laboratory discharge. *J. Phys. D*, **49**, 425203. 92, 98
- KOCHKIN, P.O., NGUYEN, C.V., VAN DEURSEN, A.P.J. & EBERT, U. (2012). Experimental study of hard x-rays emitted from metre-scale positive discharges in air. *J. Phys. D*, **45**, 425202. 17, 94
- KOCHKIN, P.O., VAN DEURSEN, A.P.J. & EBERT, U. (2014). Experimental study of the spatio-temporal development of metre-scale negative discharge in air. *J. Phys. D*, **47**, 145203. 83, 94

REFERENCES

- KOCHKIN, P.O., VAN DEURSEN, A.P.J. & EBERT, U. (2015). Experimental study on hard x-rays emitted from metre-scale negative discharges in air. *J. Phys. D*, **48**, 025205. 94
- KÖHN, C., CHANRION, O. & NEUBERT, T. (2017). Electron acceleration during streamer collisions in air. *Geophys. Res. Lett.*, **44**, 2604. 94
- KÖHN, C., CHANRION, O. & NEUBERT, T. (2019). The Sensitivity of Sprite Streamer Inception on the Initial Electron Ion Patch. *Journal of Geophysical Research (Space Physics)*, **124**, 3083–3099. 97
- KOSSYI, I.A., KOSTINSKY, A.Y., MATVEYEV, A.A. & SILAKOV, V.P. (1992). Kinetic scheme of the non-equilibrium discharge in nitrogen-oxygen mixtures. *Plasma Sour. Sci. Technol.*, **1**, 207. 78, 135, 136
- KOSTINSKIY, A.Y., SYSSOEV, V.S., BOGATOV, N.A., MAREEV, E.A., ANDREEV, M.G., BULATOV, M.U., SUKHAREVSKY, D.I. & RAKOV, V.A. (2018). Abrupt Elongation (Stepping) of Negative and Positive Leaders Culminating in an Intense Corona Streamer Burst: Observations in Long Sparks and Implications for Lightning. *Journal of Geophysical Research (Atmospheres)*, **123**, 5360–5375. 77, 83, 94, 111, 112, 118
- LANDAU, L. & LIFSHITZ, E. (1987). *Fluid Mechanics*. Pergamon Press, 2nd edn. 22
- LES RENARDIÈRES GROUP (1978a). Negative discharges in long air gaps at les renardières. *Elektra*, **74**, 67–216. 3, 76, 111
- LES RENARDIÈRES GROUP (1978b). Positive discharges in long air gaps at les renardières, 1975 results and conclusions. *Elektra*, **53**, 31–153. 3, 111
- LEVEQUE, R. (2002). *Finite Volume Methods for Hyperbolic Problems*. Cambridge Texts in Applied Mathematics, Cambridge University Press. 28, 34, 35, 36, 38, 41, 43, 48
- LI, L., NIXON, C.A., ACHTERBERG, R.K., SMITH, M.A., GORIUS, N.J.P., JIANG, X., CONRATH, B.J., GIERASCH, P.J., SIMON-MILLER, A.A., MICHAEL FLASAR, F., BAINES, K.H., INGERSOLL, A.P., WEST, R.A., VASAVADA, A.R. & EWALD, S.P. (2011). The global energy balance of Titan. *Geophys. Res. Lett.*, **38**, L23201. 106
- LIU, L. & BECERRA, M. (2017). Gas heating dynamics during leader inception in long air gaps at atmospheric pressure. *Journal of Physics D Applied Physics*, **50**, 345202. 23, 114, 128, 130, 131, 132, 133, 134, 135
- LIU, N. (2010). Model of sprite luminous trail caused by increasing streamer current. *Geophys. Res. Lett.*, **37**, L04102. 77, 98
- LIU, N. & PASKO, V.P. (2004). Effects of photoionization on propagation and branching of positive and negative streamers in sprites. *J. Geophys. Res. (Space Phys)*, **109**, A04301. 50
- LIU, N. & PASKO, V.P. (2006). Effects of photoionization on similarity properties of streamers at various pressures in air. *J. Phys. D*, **39**, 327. 49, 50
- LIU, N., KOSAR, B., SADIGHI, S., DWYER, J.R. & RASSOUL, H.K. (2012). Formation of Streamer Discharges from an Isolated Ionization Column at Subbreakdown Conditions. *Phys. Rev. Lett.*, **109**, 025002. 86
- LIU, N., DWYER, J.R., STENBAEK-NIELSEN, H.C. & MCHARG, M.G. (2015). Sprite streamer initiation from natural mesospheric structures. *Nature communications*, **6**, 7540. 97
- LIU, N., SPIVA, N., DWYER, J.R., RASSOUL, H.K., FREE, D. & CUMMER, S.A. (2015). Upward electrical discharges observed above Tropical Depression Dorian. *Nature Communications*, **6**, 5995. 49
- LUQUE, A. (2017). Radio Frequency Electromagnetic Radiation From Streamer Collisions. *J. Geophys. Res. (Atmos.)*, **122**, 10. 80, 94
- LUQUE, A. & EBERT, U. (2009). Emergence of sprite streamers from screening-ionization waves in the lower ionosphere. *Nature Geoscience*, **2**, 757. 97
- LUQUE, A. & EBERT, U. (2010). Sprites in varying air density: Charge conservation, glowing negative trails and changing velocity. *Geophys. Res. Lett.*, **37**, L06806. 77, 98, 99, 105
- LUQUE, A. & EBERT, U. (2012). Density models for streamer discharges: Beyond cylindrical symmetry and homogeneous media. *J. Comput. Phys.*, **231**, 904. 49
- LUQUE, A. & EBERT, U. (2014). Growing discharge trees with self-consistent charge transport: the collective dynamics of streamers. *New Journal of Physics*, **16**, 013039. 22, 72, 99, 125
- LUQUE, A. & GORDILLO-VÁZQUEZ, F.J. (2011). Sprite beads originating from inhomogeneities in the mesospheric electron density. *Geophys. Res. Lett.*, **38**, L04808. 83, 98
- LUQUE, A., EBERT, U., MONTIJN, C. & HUNSDORFER, W. (2007). Photoionization in negative streamers: Fast computations and two propagation modes. *Appl. Phys. Lett.*, **90**, 081501. 73, 80
- LUQUE, A., RATUSHNAYA, V. & EBERT, U. (2008). Positive and negative streamers in ambient air: modelling evolution and velocities. *J. Phys. D*, **41**, 234005. 12, 86

- LUQUE, A., STENBAEK-NIELSEN, H.C., MCHARG, M.G. & HAALAND, R.K. (2016a). Sprite beads and glows arising from the attachment instability in streamer channels. *J. Geophys. Res. (Space Phys)*, **121**, 2431. 16, 97, 98, 99, 100, 105, 108
- LUQUE, A., STENBAEK-NIELSEN, H.C., MCHARG, M.G. & HAALAND, R.K. (2016b). Sprite beads and glows arising from the attachment instability in streamer channels. *J. Geophys. Res. (Space Phys)*, **121**, 77, 83, 92
- LUQUE, A., GONZÁLEZ, M. & GORDILLO-VÁZQUEZ, F.J. (2017). Streamer discharges as advancing imperfect conductors: inhomogeneities in long ionized channels. *Plasma Sour. Sci. Technol.*, **26**, 125006. 23, 78, 99, 106
- MALAGÓN-ROMERO, A. & LUQUE, A. (2018). A domain-decomposition method to implement electrostatic free boundary conditions in the radial direction for electric discharges. *Comput. Phys. Commun.*, **225**, 114. 18, 122
- MALAGÓN-ROMERO, A. & LUQUE, A. (2019). Spontaneous Emergence of Space Stems Ahead of Negative Leaders in Lightning and Long Sparks. *Geophys. Res. Lett.*, **46**, 4029. 18, 122
- MALAGÓN-ROMERO, A., PÉREZ-INVERNÓN, F.J., LUQUE, A. & GORDILLO-VÁZQUEZ, F.J. (2019). Analysis of the Spatial Nonuniformity of the Electric Field in Spectroscopic Diagnostic Methods of Atmospheric Electricity Phenomena. *Journal of Geophysical Research (Atmospheres)*, **124**, 12,356–12,370. 19
- MALAGÓN-ROMERO, A., TEUNISSEN, J., STENBAEK-NIELSEN, H.C., MCHARG, M.G., EBERT, U. & LUQUE, A. (2020). On the Emergence Mechanism of Cartot Sprites. *Geophys. Res. Lett.*, **47**, e85776. 18, 123
- MARISALDI, M., ARGAN, A., TROIS, A., GIULIANI, A., TAVANI, M., LABANTI, C., FUSCHINO, F., BULGARELLI, A., LONGO, F., BARBIELLINI, G., DEL MONTE, E., MORETTI, E., TRIFOGLIO, M., COSTA, E., CARAVEO, P., CATTANEO, P.W., CHEN, A., D'AMMANDO, F., DE PARIS, G., DI COCCO, G., DI PERSIO, G., DONNARUMMA, I., EVANGELISTA, Y., FEROCI, M., FERRARI, A., FIORINI, M., FROYSLAND, T., GALLI, M., GIANOTTI, F., LAPSHOV, I., LAZZAROTTO, F., LIPARI, P., MEREGHETTI, S., MORSELLI, A., PACCIANI, L., PELLIZZONI, A., PEROTTI, F., PICOZZA, P., PIANO, G., PILIA, M., PREST, M., PUCELLA, G., RAPISARDA, M., RAPPOLDI, A., RUBINI, A., SABATINI, S., SOFFITTA, P., STRIANI, E., VALLAZZA, E., VERCELLONE, S., VITTORINI, V., ZAMBRA, A., ZANELLO, D., ANTONELLI, L.A., COLAFRANCESCO, S., CUTINI, S., GIOMMI, P., LUCARELLI, F., PITTORI, C., SANTOLAMAZZA, P., VERRECCHIA, F. & SALLOTTI, L. (2010). Gamma-Ray Localization of Terrestrial Gamma-Ray Flashes. *Phys. Rev. Lett.*, **105**, 128501. 75
- MARRONE, P.V. & TREANOR, C.E. (1963). Chemical Relaxation with Preferential Dissociation from Excited Vibrational Levels. *Physics of Fluids*, **6**, 1215. 115
- MCEWAN, M.J. & PHILLIPS, L.F. (1975). Chemistry of the atmosphere. *nyhp*. 137
- MCHARG, M.G., STENBAEK-NIELSEN, H.C. & KAMMAE, T. (2007). Observations of streamer formation in sprites. *Geophys. Res. Lett.*, **34**, L06804. 97, 102
- MONTANYÀ, J., FABRÓ, F., VAN DER VELDE, O., MARCH, V., ROLFE WILLIAMS, E., PINEDA, N., ROMERO, D., SOLÀ, G. & FREJO, M. (2016). Global distribution of winter lightning: a threat to wind turbines and aircraft. *Natural Hazards and Earth System Sciences*, **16**, 1465. 1
- MOORE, C.B., EACK, K.B., AULICH, G.D. & RISON, W. (2001). Energetic radiation associated with lightning stepped-leaders. *Geophys. Res. Lett.*, **28**, 2141. 1
- NASIR, N.M., LEE, B., YAP, S.S., THONG, K. & YAP, S.L. (2016). Cold plasma inactivation of chronic wound bacteria. *Archives of biochemistry and biophysics*, **605**, 76–85. 1
- NIJDM, S., VAN DE WETERING, F.M.J.H., BLANC, R., VAN VELDHIJZEN, E.M. & EBERT, U. (2010). Probing photoionization: experiments on positive streamers in pure gases and mixtures. *J. Phys. D*, **43**, 145204. 5, 10
- NIJDM, S., TAKAHASHI, E., MARKOSYAN, A.H. & EBERT, U. (2014). Investigation of positive streamers by double-pulse experiments, effects of repetition rate and gas mixture. *Plasma Sour. Sci. Technol.*, **23**, 025008. 82, 92
- NIJDM, S., TEUNISSEN, J. & EBERT, U. (2020). The physics of streamer discharge phenomena. *Plasma Sources Science Technology*, **29**, 103001. 10
- ORVILLE, R.E. (1968). Spectrum of the lightning stepped leader. *J. Geophys. Res.*, **73**, 6999. 13, 76
- ØSTGAARD, N., CARLSON, B.E., NISI, R.S., GJESTELAND, T., GRONDAHL, O., SKELTIVED, A., LEHTINEN, N.G., MEZENTSEV, A., MARISALDI, M. & KOCHKIN, P. (2016). Relativistic electrons from sparks in the laboratory. *J. Geophys. Res. (Atmos.)*, **121**, 2939. 94
- PANCHESHNYI, S. (2005). Role of electronegative gas admixtures in streamer start, propagation and branching phenomena. *Plasma Sour. Sci. Technol.*, **14**, 645. 5, 10
- PANCHESHNYI, S. (2013). Effective ionization rate in nitrogen-oxygen mixtures. *J. Phys. D*, **46**, 155201. 131, 135
- PANCHESHNYI, S., BIAGI, S., BORDAGE, M.C., HAGELAAR, G.J.M., MORGAN, W.L., PHELPS, A.V. & PITCHFORD, L.C. (2012). The LXCat project: Electron scattering cross sections and swarm parameters for low temperature plasma modeling. *Chem. Phys.*, **398**, 148. 128
- PASKO, V.P. & STENBAEK-NIELSEN, H.C. (2002). Diffuse and streamer regions of sprites. *Geophys. Res. Lett.*, **29**, 1440. 106

REFERENCES

- PASKO, V.P., INAN, U.S., TARANENKO, Y.N. & BELL, T.F. (1995). Heating, ionization and upward discharges in the mesosphere, due to intense quasi-electrostatic thundercloud fields. *Geophys. Res. Lett.*, **22**, 365. 97
- PASKO, V.P., INAN, U.S. & BELL, T.F. (1996). Sprites as luminous columns of ionization produced by quasi-electrostatic thundercloud fields. *Geophys. Res. Lett.*, **23**, 649. 97
- PASKO, V.P., INAN, U.S., BELL, T.F. & TARANENKO, Y.N. (1997). Sprites produced by quasi-electrostatic heating and ionization in the lower ionosphere. , **102**, 4529. 97
- PASKO, V.P., INAN, U.S., BELL, T.F. & REISING, S.C. (1998). Mechanism of ELF radiation from sprites. *Geophys. Res. Lett.*, **25**, 3493. 97
- PASKO, V.P., YAIR, Y. & KUO, C.L. (2012). Lightning Related Transient Luminous Events at High Altitude in the Earth's Atmosphere: Phenomenology, Mechanisms and Effects. *Space Sci. Rev.*, **168**, 475. 107, 109
- PÉREZ-IVERNÓN, F.J., MALAGÓN-ROMERO, A., GORDILLO-VÁZQUEZ, F.J. & LUQUE, A. (2020). The Contribution of Sprite Streamers to the Chemical Composition of the Mesosphere-Lower Thermosphere. *Geophys. Res. Lett.*, **47**, e88578. 19
- PHELPS, A.V. & PITCHFORD, L.C. (1985). Anisotropic scattering of electrons by N₂ and its effect on electron transport. *Phys. Rev. A*, **31**, 2932. 127, 128
- PHELPS, C.T. (1974). Positive streamer system intensification and its possible role in lightning initiation. *Journal of Atmospheric and Terrestrial Physics*, **36**, 103. 92
- PHELPS, C.T. & GRIFFITHS, R.F. (1976). Dependence of positive corona streamer propagation on air pressure and water vapor content. *J. Appl. Phys.*, **47**, 2929. 112
- POPOV, N.A. (2001). Investigation of the Mechanism for Rapid Heating of Nitrogen and Air in Gas Discharges. *Plasma Physics Reports*, **27**, 886. 79
- POPOV, N.A. (2003). Formation and development of a leader channel in air. *Plasma Physics Reports*, **29**, 695. 22, 76, 92, 116
- POPOV, N.A. (2011). Fast gas heating in a nitrogen-oxygen discharge plasma: I. Kinetic mechanism. *J. Phys. D*, **44**, 285201. 114, 132
- POPOV, N.A. (2016). Kinetics of plasma-assisted combustion: effect of non-equilibrium excitation on the ignition and oxidation of combustible mixtures. *Plasma Sources Science Technology*, **25**, 043002. 116
- QIN, J. & PASKO, V.P. (2015). Dynamics of sprite streamers in varying air density. *Geophys. Res. Lett.*, **42**, 2031. 49
- QIN, J., CELESTIN, S. & PASKO, V.P. (2012). Minimum charge moment change in positive and negative cloud to ground lightning discharges producing sprites. *Geophys. Res. Lett.*, **39**, L22801. 98
- QIN, J., CELESTIN, S. & PASKO, V.P. (2013a). Dependence of positive and negative sprite morphology on lightning characteristics and upper atmospheric ambient conditions. *J. Geophys. Res. (Space Phys)*, **118**, 2623. 108
- QIN, J., CELESTIN, S., PASKO, V.P., CUMMER, S.A., MCHARG, M.G. & STENBAEK-NIELSEN, H.C. (2013b). Mechanism of column and carrot sprites derived from optical and radio observations. *Geophys. Res. Lett.*, **40**, 4777. 98, 108
- RAIZER, Y.P. (1991). *Gas Discharge Physics*. Springer-Verlag, Berlin, Germany. 2, 14
- RAIZER, Y.P., MILIKH, G.M., SHNEIDER, M.N. & NOVAKOVSKI, S.V. (1998). Long streamers in the upper atmosphere above thundercloud. *J. Phys. D*, **31**, 3255. 97
- RAKOV, V.A. & UMAN, M.A. (2003a). *Lightning*. Cambridge University Press. 1
- RAKOV, V.A. & UMAN, M.A. (2003b). *Lightning*. 2, 111
- RISON, W., KREHBIEL, P.R., STOCK, M.G., EDENS, H.E., SHAO, X.M., THOMAS, R.J., STANLEY, M.A. & ZHANG, Y. (2016). Observations of narrow bipolar events reveal how lightning is initiated in thunderstorms. *Nature Communications*, **7**, 10721. 92
- SABA, M.M., SCHUMANN, C., WARNER, T.A., HELSDON, J.H. & ORVILLE, R.E. (2015). High-speed video and electric field observation of a negative upward leader connecting a downward positive leader in a positive cloud-to-ground flash. *Electric Power Systems Research*, **118**, 89 – 92, the Lightning Flash and Lightning Protection (SIPDA 2013). 111
- SCHONLAND, B.F.J. & COLLENS, H. (1934). Progressive Lightning. *Proceedings of the Royal Society of London Series A*, **143**, 654–674. 2
- SCHONLAND, B.F.J., MALAN, D.J. & COLLENS, H. (1935). Progressive Lightning. II. *Proc. R. Soc. London, Ser. A*, **152**, 595. 3, 76
- SÉGUR, P., BOURDON, A., MARODE, E., BESSIERES, D. & PAILLOL, J.H. (2006). The use of an improved Eddington approximation to facilitate the calculation of photoionization in streamer discharges. *Plasma Sour. Sci. Technol.*, **15**, 648. 73
- SEKIMOTO, K. & TAKAYAMA, M. (2007). Influence of needle voltage on the formation of negative core ions using atmospheric pressure corona discharge in air. *International Journal of Mass Spectrometry*, **261**, 38–44. 137

- SHI, F., LIU, N. & DWYER, J.R. (2017). Three-Dimensional Modeling of Two Interacting Streamers. *J. Geophys. Res. (Atmos.)*, **122**, 10, 22
- SHNEIDER, M.N., MOKROV, M.S. & MILIKH, G.M. (2012). Dynamic contraction of the positive column of a self-sustained glow discharge in molecular gas. *Physics of Plasmas*, **19**, 033512. 113
- SIGMOND, R.S. (1984). The residual streamer channel: Return strokes and secondary streamers. *J. Appl. Phys.*, **56**, 1355. 15, 77
- SMITH, D.M., LOPEZ, L.I., LIN, R.P. & BARRINGTON-LEIGH, C.P. (2005). Terrestrial Gamma-Ray Flashes Observed up to 20 MeV. *Science*, **307**, 1085. 75
- SRIVASTAVA, A., JIANG, R., YUAN, S., QIE, X., WANG, D., ZHANG, H., SUN, Z. & LIU, M. (2019). Intermittent Propagation of Upward Positive Leader Connecting a Downward Negative Leader in a Negative Cloud-to-Ground Lightning. *Journal of Geophysical Research (Atmospheres)*, **124**, 13,763–13,776. 111
- STANLEY, M., KREHBIEL, P., BROOK, M., MOORE, C., RISON, W. & ABRAHAMS, B. (1999). High speed video of initial sprite development. *Geophys. Res. Lett.*, **26**, 3201. 97
- STENBAEK-NIELSEN, H.C. & MCHARG, M.G. (2008). High time-resolution sprite imaging: observations and implications. *J. Phys. D*, **41**, 234009. 97, 98
- STENBAEK-NIELSEN, H.C., KANMAE, T., MCHARG, M.G. & HAALAND, R. (2013). High-Speed Observations of Sprite Streamers. *Surveys in Geophysics*, **34**, 769. 97, 105
- STENBAEK-NIELSEN, H.C., MCHARG, M.G., HAALAND, R.K. & LUQUE. (2020). Optical spectra of small-scale sprite features observed at 10,000 fps. *Journal of Geophysical Research: Atmospheres*, e2020JD033170. 97
- TEUNISSEN, J. & EBERT, U. (2017). Simulating streamer discharges in 3D with the parallel adaptive Afivo framework. *J. Phys. D*, **50**, 474001. 22, 99, 100
- TEUNISSEN, J. & EBERT, U. (2018). Afivo: A framework for quadtree/octree AMR with shared-memory parallelization and geometric multigrid methods. *Comput. Phys. Commun.*, **233**, 156. 49, 99, 100
- THOMAS, R.J., KREHBIEL, P.R., RISON, W., HAMLIN, T., HARLIN, J. & SHOWN, D. (2001). Observations of VHF source powers radiated by lightning. *Geophys. Res. Lett.*, **28**, 143. 75
- VELDHUIZEN, VAN, E.M. (2000). *Electrical discharges for environmental purposes: fundamentals and applications*. Nova Science. 1
- VIDAL, F., GALLIMBERTI, I., RIZK, F.A.M., JOHNSTON, T.W., BONDIU-CLEGERIE, A., COMTOIS, D., KIEFFER, J.C., LA FONTAINE, B., MERCURE, H.P. & PEPIN, H. (2002). Modeling of the air plasma near the tip of the positive leader. *IEEE Trans. Plasma Sci.*, **30**, 1339. 128
- WAIT, J.R. & SPIES, K.P. (1964). *Characteristics of the Earth-ionosphere waveguide for VLF radio waves*. 300, US Dept. of Commerce, National Bureau of Standards: for sale by the Supt. of 100
- WANG, X., YUAN, P., CEN, J. & XUE, S. (2016). Correlation between the spectral features and electric field changes for natural lightning return stroke followed by continuing current with M-components. *J. Geophys. Res. (Atmos.)*, **121**, 8615. 111
- WESCOTT, E.M., SENTMAN, D.D., HEAVNER, M.J., HAMPTON, D.L., LYONS, W.A. & NELSON, T. (1998). Observations of ‘Columniform’ sprites. *J. Atm. Sol.-Terr. Phys.*, **60**, 733. 98
- WORMEESTER, G., PANCHESHNYI, S., LUQUE, A., NIJDAM, S. & EBERT, U. (2010). Probing photo-ionization: simulations of positive streamers in varying N₂ : O₂-mixtures. *J. Phys. D*, **43**, 505201. 80
- WU, J., GAO, X., MA, Y. & LIU, N. (2019). Streamer initiation from column hydrometeor at weak ambient electric field. *Plasma Research Express*, **1**, 035009. 97
- ZHELEZNIAK, M.B., MNATSAKIAN, A.K. & SIZYKH, S.V. (1982). Photoionization of nitrogen and oxygen mixtures by radiation from a gas discharge. *High Temperature Science*, **20**, 423. 5, 80

Acknowledgements

Me gustaría dedicar este trabajo a mi familia, en especial a mis padres y hermanos, por su apoyo incondicional, esfuerzo y comprensión. Y a tí Mercedes, por estar ahí en los buenos y no tan buenos momentos, siempre con una sonrisa.

A mis amigos más cercanos, que aunque muchas veces desde la distancia, también me han acompañado. Juanjo, Alba, David y Rafa, gracias.

Thanks to my colleagues and friends Javi, Antonio, Paco, Laly, Dongshuai, Ny, Miguel, and Anthony, for the good times that we spent together.

I would like to thank my supervisor Dr. Alejandro Luque and Dr. Francisco J. Gordillo Vázquez for their support, guidance and commitment. Thanks to the Multiscale Dynamics group at CWI, especially to Jannis and Ute for their help during my short stay in Amsterdam.

I would like to acknowledge the University of Granada for allowing me to get a Ph.D. in the Physics and Space Science program.

This work was supported by the European Research Council (ERC) under the European Union H2020 programme/ERC grant agreement 681257. We acknowledge support from the State Agency for Research of the Spanish MCIU through the “Center of Excellence Severo Ochoa” award for the Instituto de Astrofísica de Andalucía (SEV-2017-0709). We thankfully acknowledge the computer resources, technical expertise and assistance provided by the Barcelona Supercomputing Center - Centro Nacional de Supercomputación.

Alejandro Malagón Romero

Curriculum Vitae

Date of birth: April 12th, 1991

Place of birth: Granada, Spain

Education

- 2017–2021 **PhD, Physics & Space Sciences**, *University of Granada*.
Dissertation: *Numerical investigation on the advance of leader channels in lightning and long sparks*.
Supervisor: Dr. Alejandro Luque Estepa
- 2015–2016 **MSc, Theoretical Physics**, *Autonomous University of Madrid*.
Dissertation: *Renormalon divergences: Hard function in QCD and jet functions in SCET and bHQET*.
Supervisor: Dr. Vicent Mateu Barreda
- 2011–2015 **BSc, Physics**, *University of Granada*.
Dissertation: *Role of the Group Theory in Particle Physics*.
Supervisor: Dr. Fernando Cornet Sánchez del Águila

Research Experience

- Centrum Wiskunde & Informatica, Multiscale Dynamics group.
Feb, 2019 **Secondment**.
Investigating the carrot sprite mechanism with streamer simulations using AFIVO streamer code.
Advisor : **Dr. J. Teunissen**, *Tenured Scientist, Multiscale Dynamics group*.
Centrum Wiskunde & Informatica, Multiscale Dynamics group.
Oct – Nov, 2018 **Secondment**.
Investigating the carrot sprite mechanism with streamer simulations using AFIVO streamer code.
Advisor : **Dr. J. Teunissen**, *Tenure track, Multiscale Dynamics Group*.
Institute of Astrophysics of Andalusia, Solar System department.
2017 – 2021 **Lightning propagation and high-energy emissions within coupled multimodel simulations (eLightning)**.
Developing distributed parallel numerical model in Python, FORTRAN and MPI to study the stepped leader propagation.
Supervisor : **Dr. A. Luque**, *Tenured Scientist, Solar System department*.

Institute of Theoretical Physics UAM/CSIC.

2015-2016 **Master Dissertation Research: Renormalon divergences: Hard function in QCD and jet functions in SCET and bHQET.**

Investigating renormalons (divergences encoded in poles) in Quantum Chromodynamics through different diagrams like the associated to the jet function.

Supervisor : **Dr. Vicent Mateu Barreda**, *Ramón y Cajal Fellow, Department of Theoretical Physics.*

University of Granada.

2014 **Undergraduate Research Initiation grant: Study of the $tc\gamma$ coupling at the LHC.**

Studying Flavour Changing Neutral Currents (FCNC) by means of the $tc\gamma$ coupling with Feynrules and Madgraph.

Advisor : **Dr. Fernando Cornet Sánchez del Águila**, *Full Professor, department of Theoretical Physics.*

Refereed Journal Articles

A. Luque, F. José Gordillo-Vázquez, D. Li, **A. Malagón-Romero**, F. J. Pérez-Invernón, A. Schmalzried, S. Soler, O. Chanrion, M. Heumesser, T. Neubert, V. Reglero, N. Østgaard, Modeling lightning observations from space-based platforms (CloudScat.jl 1.0), Geoscientific Model Development 13 (11) (2020) 5549–5566. doi:10.5194/gmd-13-5549-2020.

S. Soler, F. J. Pérez-Invernón, F. J. Gordillo-Vázquez, A. Luque, D. Li, **A. Malagón-Romero**, T. Neubert, O. Chanrion, V. Reglero, J. Navarro-Gonzalez, G. Lu, H. Zhang, A. Huang, N. Østgaard, Blue Optical Observations of Narrow Bipolar Events by ASIM Suggest Corona Streamer Activity in Thunderstorms, Journal of Geophysical Research (Atmospheres) 125 (16) (2020) e32708. doi:10.1029/2020JD032708.

F. J. Pérez-Invernón, **A. Malagón-Romero**, F. J. Gordillo-Vázquez, A. Luque, The Contribution of Sprite Streamers to the Chemical Composition of the Mesosphere-Lower Thermosphere, Geophys. Res. Lett. 47 (14) (2020) e88578. doi:10.1029/2020GL088578.

A. Malagón-Romero, J. Teunissen, H. C. Stenbaek-Nielsen, M. G. McHarg, U. Ebert, A. Luque, On the Emergence Mechanism of

Carrot Sprites, *Geophys. Res. Lett.* 47 (1) (2020) e85776. arXiv:2001.06248, doi:10.1029/2019GL085776.

A. Malagón-Romero, F. J. Pérez-Invernón, A. Luque, F. J. Gordillo-Vázquez, Analysis of the Spatial Nonuniformity of the Electric Field in Spectroscopic Diagnostic Methods of Atmospheric Electricity Phenomena, *Journal of Geophysical Research (Atmospheres)* 124 (22) (2019) 12,356–12,370. arXiv:1910.06012, doi:10.1029/2019JD030945.

A. Malagón-Romero, A. Luque, Spontaneous Emergence of Space Stems Ahead of Negative Leaders in Lightning and Long Sparks, *Geophys. Res. Lett.* 46 (7) (2019) 4029–4038. arXiv:1909.04424, doi:10.1029/2019GL082063.

A. Malagón-Romero, A. Luque, A domain-decomposition method to implement electrostatic free boundary conditions in the radial direction for electric discharges, *Computer Physics Communications* 225 (2018) 114–121. arXiv:1708.09444, doi:10.1016/j.cpc.2018.01.003.

Conference Proceedings/Presentations

If the presenter is not provided: Presenter is Alejandro Malagón-Romero.

A. Malagón-Romero and A. Luque. “Leader discharge stepping in dry and humid air”, European Geosciences Union General Assembly 2020 (EGU), Vienna, Austria, 2020, Poster (online meeting).

F. J. Pérez-Invernón, **A. Malagón-Romero**, A. Luque, F.J. Gordillo-Vázquez. “Spectroscopic diagnostic methods of non-uniform atmospheric discharges”, American Geophysical Union fall meeting 2019 (AGU), San Francisco, United States of America, 2019. Poster. Presenter: F. J. Pérez-Invernón.

F. J. Pérez-Invernón, S. Soler, F. J. Gordillo-Vázquez, A. Luque, D. Li, **A. Malagón-Romero**, T. Neubert, O. Chanrion, K. Dimitriadou, M. Heumesser, V. Reglero, J. Navarro-Gonzales, N. Østgaard, G. Lu, H. Zhang, A. Huang. "Analysis of blue discharges detected by ASIM-MMIA with indication of their source altitudes and electromagnetic signatures", American Geophysical Union fall meeting 2019 (AGU), San Francisco, United States of America, 2019. Oral. Presenter: F. J. Pérez-Invernón.

A. Luque, M.B. Teixeira Gomes, **A. Malagón-Romero**, D. Li. "Dynamics of the leading edge of an extensive streamer corona", American Geophysical Union fall meeting 2019 (AGU), San Francisco, United States of America, 2019. Poster. Presenter: A. Luque.

A. Malagón-Romero, J. Teunissen, U. Ebert, A. Luque. "Lateral streamers emergence from sprite glows", American Geophysical Union fall meeting 2019 (AGU), San Francisco, United States of America, 2019. Poster.

A. Malagón-Romero, J. Teunissen, A. Luque and U. Ebert. "Lateral streamer emergence from sprite glows", 2nd Science And Innovation with Thunderstorms (SAINT) Summer School", Toulouse, France, 2019. Poster.

S. Soler, F. J. Pérez-Invernón, F. J. Gordillo-Vazquez, **A. Malagón-Romero**, A. Luque, J. Navarro-González, V. Reglero, T. Neubert, N. Ostgaard, O. Chanrion, K. Dimitriadou, C. Zuccotti, and M. Heumesser. "Analysis of spectral emissions associated with thunderstorm activity detected by ASIM", European Geosciences Union General Assembly 2019 (EGU), Vienna, Austria, 2019, Poster. Presenter: F. J. Pérez-Invernón

A. Malagón-Romero, J. Teunissen, A. Luque and U. Ebert. "Lateral streamer emergence from space stem precursor", European Geosciences Union General Assembly 2019 (EGU), Vienna, Austria, 2019, Oral.

A. Malagón-Romero and A. Luque. "Space stem precursors", 2nd Science And Innovation with Thunderstorms (SAINT) Summer School", Leiden, The Netherlands, 2019. Oral.

A. Luque, M.B. Teixeira Gomes, D. Li, **A. Malagón-Romero**. “Homogenised Models for Large-scale Streamer Corona Discharges. American Geophysical Union fall meeting 2018 (AGU), Washington D. C., United States of America, 2018. Oral. Presenter: D. Li.

A. Malagón-Romero and A. Luque. “Humidity effects on streamer propagation and the formation of space stems”, American Geophysical Union fall meeting 2018 (AGU), Washington D. C., United States of America, 2018. Poster.

A. Malagón-Romero and A. Luque. “Space stem precursors”, 1st Science And Innovation with Thunderstorms (SAINT) Summer School”, Barcelona, Spain, 2018. Poster.

A. Malagón-Romero and A. Luque. “Space stem precursors”, 16th International Conference on Atmospheric Electricity (ICAE), Nara, Japan, 2018. Oral.

A. Malagón-Romero and A. Luque. “Formation of space-stem precursors ahead of a lightning leader”, American Geophysical Union fall meeting 2017 (AGU), New Orleans, United States of America, 2017, Poster.

A. Malagón-Romero and A. Luque. “Fluid model for the streamer-to-leader transition in lightning channels”, XXXVI Biennial Meeting of the Real Sociedad Española de Física, Santiago de Compostela, Spain, 2017, Oral.

A. Malagón-Romero and A. Luque. “Towards a fluid model for the streamer-to-leader transition in lightning channels”, XXXIII Int. Conf. On Phenomena in ionized gases (ICPIG), Lisbon, Estoril, Portugal, 2017, Poster.

A. Malagón-Romero and A. Luque. “Towards a fluid model for the streamer-to-leader transition in lightning channels”, European Geosciences Union General Assembly 2017 (EGU), Vienna, Austria, 2017, Poster.

Selection of simulation software

Author **Space Stem**: Electro-hydrodynamical code built on top of CLAWPACK and PETSc to simulate the formation of space stem precursors.

https://gitlab.com/amaro/space_stem

Author **Streamer2D**: Code built on top of CLAWPACK and PETSc to simulate streamer discharges.

<https://gitlab.com/amaro/streamer2d>

Grants

2014 **Research Initiation Grant**, University of Granada.
Study of the $tc\gamma$ coupling at the LHC.

Reviewer for scientific journals

Journal of Geophysical Research: Atmospheres

Journal of Physics D: Applied Physics

Plasma Sources Science and Technology

News Reports on My Research

El País <https://elpais.com/ciencia/2020-11-02/como-la-ciencia-esta-desentranando-el-misterio-de-los-rayos-y-las-tormentas-electricas.html>

La Cope https://www.cope.es/programas/la-tarde/audios/tarde-05-11-2020-1800-1900-horas-20201105_264997

Horizon <https://horizon-magazine.eu/article/we-are-starting-crack-mystery-how-lightning-and-thunderstorms-work.html7>

Relevant courses

Jun 2019 SAINT Summer School 2, Toulouse, France.

Jan 2019 SAINT Summer School 2, Leiden, The Netherlands.

Jul 2018 SAINT Summer School 1, Barcelona, Spain.

Jan 2018 SAINT Winter School 1, Copenhagen, Denmark.

Jul 2017 High-performance computing: Atmospheric and Oceanic Modelling (CSIC), Santiago de Compostela, Spain.